Numerical fire modeling of crude oil spills: validation report

Gomaa, Islam; Elsagan, Nour; Duong, Dana; Ko, Yoon

https://doi.org/10.4224/40002738

NRC·CNRC CONSTRUCTION

Numerical Fire Modeling of Crude Oil Spills: Validation Report

Author(s): Islam Gomaa, Nour Elsagan, Dana Duong and Yoon Ko

Report No.: A1-017078

Report Date: 15-09-2021

Contract No.: A1-017078

Agreement Date: January 2020 (Original agreement)
December 2020 (Amendment No. 1)
August 2021(Amendment No. 2)

National Research Council Canada | Conseil national de recherches Canada

Canada

Cat. No. T44-3/21-2021E-PDF
ISBN 978-0-660-38586-0 TP No. TP 15471

Numerical Fire Modeling of Crude Oil Spills: Validation Report

Author

Islam Gomaa, Research Officer, PhD

Approved

Kashef, AH
2022.02.07
14:16:32 -05'00'

Ahmed Kashef, FSU Director, PhD

Program Leader

Fire Laboratory Transition Program

NRC Construction Research Centre

Report No: A1-017078

Report Date: 15 09 2021

Contract No: A1-017078

Agreement date: January 2020 (Original agreement)
December 2020 (Amendment No. 1)
August 2021 (Amendment No. 2)

Program: FS R&D

123 pages

Copy no. 1 of 1

(This page is intentionally left blank)

Table of Content

List of Figures

List of Tables

Executive Summary

For the last six years the National Research Council (NRC) has been collaborating with Transport Canada to investigate fire incidents involving crude oil rail tank cars. The investigation involved conducting intermediate-scale experiments of a tank car engulfed in pool fires fuelled by crude oil to characterize the thermal conditions external to the tank car. The experiments were conducted by the NRC and Sandia National Laboratories using a 1/10th scale cylindrical calorimeter to simulate a tank car. The calorimeter was placed above a 2-m diameter crude oil pool fire. To complement these experiments and to gain further insight the NRC has been constructing a numerical fire model for the conducted crude oil fire tests. These efforts have been envisioned to include four stages. The first stage objective was to explore the feasibility of using numerical models to simulate crude oil fires. Two open source tools were used: Fire Dynamics Simulator (FDS) and Open Source Field Operation and Manipulation (OpenFOAM). Both tools showed promising capabilities to simulate crude oil fires using parallel computation.

Presented in this report are the findings from Stage 2 of the “Numerical Fire Modeling of Crude Oil Spills” project. The objective of this stage is to evaluate the ability of numerical models to predict gas phase parameters from crude oil pool fires. The numerical modelling results were validated using the NRC-Sandia crude oil pool fire experiments that were conducted to obtain thermal environment around a 1/10th scale rail tank car (calorimeter) engulfed in a 2-m diameter pool fire fueled by heptane and Bakken and dilbit crude oils.

A review of gas phase models used for combustion, soot generation and radiation heat transfer was conducted. Based on the review respective models were implemented in a numerical model for the NRC-Sandia experiments. Six simulations were conducted: 3 types of fuel (heptane, Bakken and dilbit) and 2 scenarios (with and without a calorimeter).

Numerical and experimental results were compared using parameters affecting the calorimeter and/or tank car boundaries: centerline plume temperature, calorimeter temperature, temperature of the air surrounding the calorimeter, calorimeter heat flux (i.e. total heat flux measured by the calorimeter), radiative heat fraction and heat release rate (HRR).

There is good agreement between the numerical and experimental results. Discrepancies are explained by considering experimental uncertainties and simplifications made to the numerical model. High resolution details are further obtained from the numerical model for the calorimeter temperature distribution and calorimeter heat flux.

A wide range of data points and parameters was used to validate the numerical models. The general agreement with experimental results provides good confidence in the ability of the numerical model to predict important thermal boundary conditions affecting a tank car subjected to a crude oil pool fire.

If further work were to be conducted, the stage 3 objective would be developing and validating pyrolysis models for Bakken and dilbit to predict their burning rates. The stage 4 objective would be using these models along with the validated gas phase models to simulate large scale fire scenarios.

1 Background

Fire incidents involving crude oil tank cars have been the subject of investigation by Transport Canada and the NRC for the last five years. Intermediate-scale experiments of a tank car engulfed in pool fires fueled by crude oil were conducted by the National Research Council Canada (NRC) at Sandia National Laboratories [1] (NRC-Sandia experiments) [2] to characterize the thermal conditions external to the tank car. In these experiments, the tank car was represented by a 1/10th scale cylindrical calorimeter, subjected to a 2-m diameter pool fire.

The NRC proposed constructing a numerical fire model for the NRC-Sandia crude oil fire tests with the following end goals in mind:

- Extrapolate the findings from the scaled-down experiments to real-scale fire incidents.
- Use the numerical model to simulate other fire incident scenarios involving tank cars accidents.
- Use the numerical model to provide high resolution thermal boundary conditions to other research groups working on the tank car structure or the crude oil inside the tank car.

The NRC suggested conducting this work over the following four stages:

- Stage 1: Feasibility study of currently-available modeling tools for crude oil pool fires
- Stage 2: Construction of a numerical model for the NRC-Sandia experiments, and validation of the numerical model using the experimental results.
- Stage 3: Construction of a numerical model that predicts crude oil burning rate and validation of the model using bench scale experiments and the NRC-Sandia experiments.
- Stage 4: Combination of all validated models to simulate real-scale experiments or fire incidents involving crude oil spills and use of the model to explore different fire scenarios.

Stage 1 was conducted using two (2) open source modeling tools: Fire Dynamics Simulator (FDS) [3], [4] and Open Source Field Operation and Manipulation (OpenFOAM) [5]–[7]. Both tools showed promising results in terms of numerical fire simulations using parallel computation. Other commercially-available tools were excluded due to cost and limitations in parallel computation. Findings from stage 1 can be found in the full report [8].

Both tools recommended from stage 1 were used in stage 2. Presented in this report are the validation results for OpenFOAM and FDS. This report includes the following sections:

- Section 2: Sub-models used in the simulations: This section includes the gas phase sub-models: the turbulence model, soot formation and oxidation model and the radiation model.
- Section 3: The experimental setup: This section includes a brief description of the NRC-Sandia experiment.

- Section 4: Simulations cases setup: This section includes the numerical domain description, the mesh description and the boundary conditions (BCs) in both OpenFoam and FDS.
- Section 5: Results and discussion: This section includes a comparison between numerical results from both tools (OpenFOAM and FDS) and the experimental ones for validation.
- Section 6: Comparison between OpenFOAM and FDS
- Section 7: Conclusions
- Section 8: Summary

Three types of fuel were used in the simulations; heptane and Bakken and dilbit crude oil. Two domains were used in each simulation tool: one domain included a calorimeter above the pool and another without the calorimeter. Validation results from six simulations are presented in this report. In order to form a complete picture about the validity of the numerical model, 11 parameters were chosen for comparison for the OpenFOAM simulation, while 8 were chosen for comparison for the FDS simulation. The parameters are presented in Section 5 and arranged in the order of most to least relevant based on the goals mentioned above. Special attention was paid to the parameters representing the thermal boundary conditions affecting tank cars in fire:

- Centerline temperature above the pool
- Exterior to calorimeter temperature (temperature of air surrounding the calorimeter)
- Radiative heat fraction
- Heat flux to the calorimeter
- Calorimeter surface temperature.

1.1 About OpenFOAM

OpenFOAM code is a general CFD software package for simulating thermo- and fluid-dynamics, chemical reactions, solid dynamics and electromagnetics, and it solves various partial differential equations using finite volume method on structured and unstructured mesh [5]. An object-oriented C++ library is utilized to numerically solve governing equations of continuum mechanics. For example, the velocity field can be represented in programming code by the symbol U that belongs to a “vectorField” class. The velocity field U would then be an instance, or an object, of the “vectorField” class; hence the term object-oriented [9].

OpenFOAM includes executables, known as applications. The applications fall into two categories: solvers that are each designed to solve a specific problem in continuum mechanics; and utilities, which are designed to perform simple pre- and post-processing tasks, mainly involving data manipulation and algebraic calculations [9]. OpenFOAM also includes libraries containing various sub-models such as turbulent models, thermo-physical models, radiation models, etc. The overall structure of OpenFOAM is shown in Figure 1 [5].

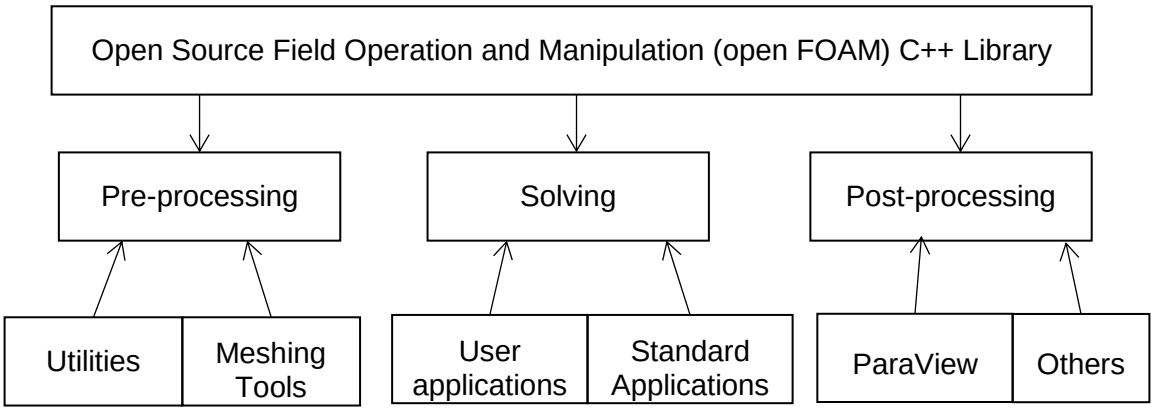

Figure 1. Overview of OpenFOAM structure [5]

OpenFOAM solver applications are written in a syntax that is very similar to the partial differential equations being solved [5]. For example the equation

$$\frac{\partial \rho U}{\partial t} + \nabla . \emptyset U - \nabla . \mu \nabla U = -\nabla p$$

is represented by the code:

```
solve (fvm::ddt(rho, U) + fvm::div(phi, U) fvm::laplacian(mu, U) == - fvc::grad(p));
```

1.1.1 Case Structure in OpenFOAM

Input files for OpenFOAM are arranged in three directories: A “constant” directory, a “system” directory and a “time” directory. The “constant” directory contains the mesh, thermodynamic properties, the turbulence model, the soot model, the radiation model and the combustion model. Most coefficients and constants, used in the models, can be changed in the respective input file for each model. The “system” directory contains the settings for solution procedures, control parameters (the controlDict file), discretization scheme (fvSchemes file) and the settings for the linear equations solver (fvSolution file). The “time” directory includes the solution at each time step. The “0” time directory contains the initial boundary conditions (BCs).

1.1.2 Modeling Steps in OpenFOAM

Constructing a simulation case, in OpenFOAM, starts with obtaining a geometrical model for the domain that includes its outer boundaries, input flow, output flow and solid objects. The next step is space discretization in which the domain is subdivided into control volumes (cells). Governing equations for the flow properties, such as velocity and temperature are solved for each control volume and stored in each cell or at their respective surfaces. The next step is imposing boundary conditions, initial conditions and selecting the models needed. This is done in the “constant” directory. The following step is running the simulation and storing the results at each time step in subsequent “time” directories. The final step is post processing the results. The standard post processing software is an open-source, multi-platform data analysis and visualization application called ParaView [10]. Post processing can also be done by running a

post processing utility that stores pre-specified parameters at predetermined locations in the domain in a separate directory.

1.2 About FDS

Fire Dynamic Simulator (FDS) is a 3D computational fluid dynamic (CFD) software used for simulating fire evolution and propagation as a thermally driven flow. It is an open-source code developed by National Institute of Standards and Technology (NIST) [3], [4]. FDS aims at solving practical fire problems in fire protection engineering, while at the same time providing a tool to study fundamental fire dynamics and combustion. The code is very specialized in fire simulations, hence it has many sub-models focusing on smoke movement and control, fire suppression, and heating, ventilation and air conditioning (HVAC) systems. FDS uses a structured and uniform grid, and a simple immersed boundary method for treatment of flow obstructions.

1.2.1 Case Structure in FDS

The input file to FDS is a single ASCII text file which provides all the necessary information to describe the scenario. The file includes:

- Global parameters such as simulation time, domain, mesh, hydrodynamic solver
- The geometry of the model and boundary conditions
- Different sub-models involved in the simulation and their associated parameters

The domain and geometry in FDS are based on rectilinear mesh, where all obstructions are assumed to conform to orthogonal shapes, and all bounding surfaces are assumed to be flat planes.

1.2.2 Modeling Steps in FDS

Modeling steps in FDS are similar to that of OpenFOAM. Domain boundaries are defined using text starting with “&VENT”. Objects in the domain are defined using text starting with “&OBST”. Burning surfaces are defined using “&SURF ID” lines. The domain is discretized by defining the mesh vertices and the number of cells in each direction; X, Y and Z. Mesh boundaries has to conform to the domain boundaries (i.e. location and size of vents). To decrease the computational “clock” time, the domain is divided into multiple connected meshes. The meshes can be distributed over an equal (or less) number of processors using parallel computing. Thermodynamic properties, reaction mechanisms, and sub model details are also included in the same input file. Running FDS simulations are done through a command prompt by typing a one-line command that specify the name of the input file and number of processors to be used. For post processing, FDS provides different types of outputs: line plots, iso-surfaces, contours and 3D videos. Output files from FDS can be visualized using a software designed specifically for FDS called Smokeview [11]. Alternatively, users can specify measuring “devices” at predetermined locations in the domain, in the input file, prior to stating the simulation for FDS to output these measurements in CSV files.

2 Sub-Models

Presented in the following sub-sections are the details of the most relevant gas phase sub-models. Shown in these sub-sections are the modeled terms in the governing equations and how they are calculated by the model. The discussion is focused on the calculation steps rather than the derivations or the assumptions made. By the end of each sub-section, all values for each sub-model's constants and coefficients are presented in a table with their location in the OpenFOAM input files.

2.1 Turbulence Model

In Computational Fluid Dynamics (CFD), there are three approaches to simulate fluid dynamics: Direct Numerical Simulation (DNS), Large Eddy Simulation (LES) and Reynold Average Navier-Stokes (RANS). In DNS the domain is resolved all the way down to the smallest scale of the flow eddies. In LES, large eddies are resolved while eddies smaller than the smallest grid size are modeled. In RANS all scales of eddies are modeled. The LES approach is used in all simulations in this work. LES is best used for transient phenomena or at transitional turbulence. In numerical fire modeling the governing equations are:

1. The continuity equation: Expression of the conservation of mass principle "mass cannot be created nor destroyed" in differential form
2. The momentum transport equation (Navier-Stokes equation)
3. The energy equation: Expression of the first law of thermodynamics which is "Energy is conserved", in a differential form.
4. The species transport equation

The Navier-Stokes (NS) equation governs the velocity and pressure fields. For turbulent flows, NS equation almost always has to be solved numerically. The velocity vector is divided into 2 components; a mean velocity component and a fluctuating component that represents the turbulence phenomenon in a flow. That fluctuating component results in a new term, $\frac{\partial \tau_{ij}}{\partial x_j}$, in the NS equation (Eq. 1) that cannot be solved numerically. τ_{ij} is the deviatoric stress tensor that is a function of the velocity fluctuations.

$$\text{Eq. 1} \quad \frac{\partial \bar{u}_i}{\partial t} + \bar{u}_j \frac{\partial \bar{u}_i}{\partial x_j} = -\frac{1}{\rho}\frac{\partial \bar{p}}{\partial x_j} + \frac{\partial}{\partial x_j}\left(\upsilon \frac{\partial \bar{u}_i}{\partial x_j}\right) + \frac{1}{\rho}\frac{\partial \tau_{ij}}{\partial x_j}$$

Because these velocity fluctuations are happening at a scale smaller than the numerical grid size, a sub-grid scale turbulence model is needed to account for the effect of these fluctuations on the main flow. In almost all turbulence models the Boussinesq hypothesis (Eq. 2) is applied:

$$\text{Eq. 2} \quad \tau_{ij} = \frac{2}{3} k_{SGS} \delta_{ij} - 2\upsilon_{SGS} \bar{S}_{ij} \qquad \text{Eq. 3} \quad where,\ \bar{S}_{ij} = \frac{1}{2}\left(\frac{\partial \bar{u}_i}{\partial x_j} + \frac{\partial \bar{u}_j}{\partial x_i}\right)$$

In Eq. 2, another sub-grid term appears that cannot be resolved, υ_{SGS}, the turbulent viscosity or the sub-grid scale eddy viscosity. This is computed using the sub-grid kinetic energy, k_{SGS} (Eq. 4).

$$\text{Eq. 4} \quad \upsilon_{SGS} = C_k \sqrt{k_{SGS}} \Delta$$

Where, C_k is a model constant and Δ is the LES filter width (calculated from local mesh size).

The next step is to compute k_{SGS}. This is the point where turbulent models start to differ. The most common model in LES is the Smagorinsky model that assumes local balance between the sub grid energy production and the sub grid energy dissipation. In this work, the one equation eddy viscosity model (Eq. 5) is used to avoid this assumption of local balance. The one equation model (Eq. 5) is a transport equation for the sub-grid kinetic energy, k_{SGS} .

$$\text{Eq. 5} \quad \frac{\partial k_{SGS}}{\partial t} + \frac{\partial \tilde{u} k_{SGS}}{\partial x_j} = \frac{\partial}{\partial x_j}\left(\frac{\upsilon_t}{Pr_t}\frac{\partial k_{SGS}}{\partial x_j}\right) - \tau_{ij}\frac{\partial \tilde{u}_i}{\partial x_j} - \varepsilon_{SGS}$$

Where

- $k_{SGS}$is the sub-grid scale kinetic energy
- $\tilde{u}$ is the density weighted velocity vector
- υ_t is the turbulent kinematic viscosity
- Pr_t is the turbulent Prandtl number
- τ_{ij} is the deviatoric stress tensor
- ε_{SGS} is the sub-grid scale energy dissipation rate

The energy dissipation rate, ε_{SGS}, is calculated using the expression in Eq. 6, Where, C_e is a model constant.

$$\text{Eq. 6} \quad \varepsilon_{SGS} = C_e \frac{{k_{SGS}}^{3/2}}{\Delta}$$

2.2 Combustion Model

2.2.1 OpenFOAM

Combustion is a chemical process in which its reaction rate is an exponential function of the reactants' temperature called the Arrhenius equation. Gas phase combustion occurs at a scale smaller than the smallest grid size in a CFD domain. Although the temperature in each cell is numerically calculated, it's an averaged value for a temperature distribution within the cell. When using the average cell temperature to determine the rate of reaction within the cell, it results in a significant error in the reaction rate because the temperature in the Arrhenius reaction rate expression is in the exponent. Because of that, the field of combustion models is created to approximate the fuel combustion rate within each cell. Generally, there are two (2) types of combustion models; models based on a conserved scalar [7]–[11] and models based on turbulent mixing [17]–[25]. The Eddy Dissipation Concept (EDC) [20], [22], [23], [25] is a model of the latter type and was used in all simulations in this work. In recent years, the EDC model has been proven useful in modeling combustion in fire simulations [26]–[28].

In turbulent flow, mechanical/kinetic energy from the main flow is transferred through eddies, from large eddies to smaller eddies where, at each level of eddies size, part of the mechanical energy is dissipated into heat. Most of the kinetic energy dissipation into heat occurs in the smallest eddies (see Figure 2). The EDC model postulates that chemical reactions occur in the

fine scale structures corresponding to the smallest scale of eddies in the flow known as the "Kolmogorov microscales" (see in Figure 2) [22].

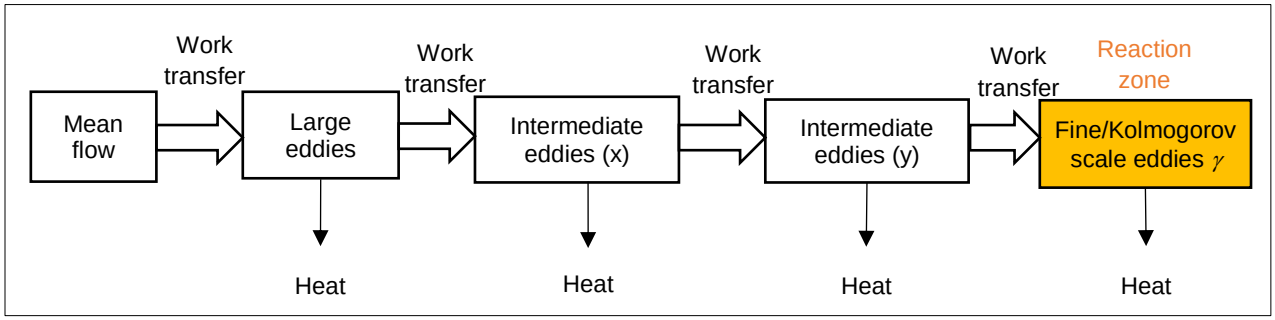

Figure 2. Turbulent energy transfer [22]

Within the framework of LES, the rate of reaction based on the EDC model is calculated using Eq. 7 [26]–[28]:

$$\text{Eq. 7} \quad \bar{\omega}_f = \bar{\rho}\dot{m}^* \frac{\gamma\chi}{1-\gamma\chi} \min(\tilde{Y}_f, \tilde{Y}_{O_2}/_s)$$

Where

- $\bar{\omega}_f$ is the filtered reaction rate of fuel
- $\bar{\rho}$ is the filtered flow density
- $\dot{m}^*$ is the mass transfer rate, per fine structure mass, between the fine structure and the surrounding
- γ is the mass fraction of the fine structure
- χ is the reacting portion of the fine structure
- $\tilde{Y}_f$ is the density weighted mass fraction of fuel (local)
- $\tilde{Y}_{O_2}$ is the density weighted mass fraction of oxygen (local)
- s is the stoichiometric coefficient (calculated from fuel chemical formula)

Mass transfer rate between the fine structure and surrounding is calculated using the expression in Eq. 8

$$\text{Eq. 8} \quad \dot{m}^* = \left(\frac{3}{C_{D2}}\right)^{1/2} \left(\frac{\varepsilon}{\upsilon}\right)^{1/2}$$

Where,

- C_{D2} is a model coefficient
- ε is the total energy dissipation rate
- υ is the molecular kinematic viscosity

While the mass fraction of the fine structure within the flow is calculated using the expression in Eq. 9

$$\text{Eq. 9} \quad \gamma = \left(\frac{L^*}{L'}\right)^{\alpha}$$

Where,

- L^* is the fine structure length scale or Kolmogorov length scale

- L' is the large structure length scale or integral length scale
- α is a model constant

The fine structure length scale is calculated using the expression in Eq. 10, where C_{D1} is a model coefficient

$$\text{Eq. 10} \quad L^* = \frac{2}{3}\left(\frac{3C_{D2}^3}{C_{D1}^2}\right)^{1/4}\left(\frac{\upsilon^3}{\varepsilon}\right)^{1/4}$$

While the large structure length scale is calculated using the expression inEq. 11

$$\text{Eq. 11} \quad L' = \left(\frac{\dot{Q}}{\rho_\infty c_p T_\infty \sqrt{g}}\right)^{2/5}$$

Where,

- $\dot{Q}$ is the heat release rate
- ρ_∞ is the ambient / far field density
- c_p is the specific heat
- T_∞ is the ambient / far field temperature
- g is the acceleration of gravity

In Eq. 10, the total energy dissipation rate is approximated using the expression in Eq. 12 and the reacting portion of the fine structure is estimated using the expression in Eq. 13.

$$\text{Eq. 12} \quad \varepsilon \approx \sqrt{\frac{2}{3}} C_{D1} \frac{k_{SGS}^{3/2}}{\Delta} + \frac{2}{9} C_{D2} \upsilon \frac{k_{SGS}}{\Delta^2}$$

$$\text{Eq. 13} \quad \chi = \begin{cases} \frac{s\tilde{Y}_{ref} + Y_{O_2}^0}{Y_{O_2}^0}, & if\ \tilde{Y}_{ref} < 0 \\ \frac{Y_{fuel}^0 - \tilde{Y}_{ref}}{Y_{fuel}^0}, & if\ \tilde{Y}_{ref} > 0 \end{cases}$$

$$\text{Eq. 14} \quad where,\ \tilde{Y}_{ref} = \tilde{Y}_{fuel} - \frac{\tilde{Y}_{O_2}}{s}$$

Where,

- $Y_{O_2}^0$ is the initial oxygen mass fraction in oxidizer (air) stream
- Y_{fuel}^0 is the Initial fuel mass fraction in the fuel stream

Shown in Table 1 are the constants and coefficients used in the turbulence model and the combustion model as well as their locations in the input files.

Table 1. Turbulence and combustion models constants

Coefficient / Constant	Value	Input file	Location
C_e	1.048	oneEqEddy.C	turbulence model source code
Pr_t	1	oneEqEddy.C	turbulence model source code
C_k	0.094	oneEqEddy.C	turbulence model source code
C_{D2}	0.75	edcInfiniteFast.C	combustion model source code
C_{D1}	0.5	edcInfiniteFast.C	combustion model source code
α	0.2	edcInfiniteFast.C	combustion model source code

2.2.2 FDS

Gas phase combustion is solved using a single-step, mixing-controlled chemical reaction which uses three (3) lumped species (fuel, oxidizer and products).

Implemented in FDS is a modified version of the Eddy Dissipation Concept (EDC) model for gas phase combustion [4, 5]. Fuel and oxidizer in the FDS version of the EDC model have a degree of mixing within each computational cell which is accounted for by a variable called the unmixed fraction (*ζ*). Each computational cell is treated as a batch reactor and the unmixed fraction (ζ) at each time step is calculated by solving the following ordinary differential equation (Eq. 15);

$$\text{Eq. 15} \quad \frac{d\zeta}{dt} = -\frac{\zeta}{\tau_{mix}}$$

Where τ_{mix} is the mixing time scale and calculated from the chemical, diffusion, advection and gravitational acceleration time scales, in addition to flame height.

Once ζ is calculated, it is used to calculate the average mass fraction $\widetilde{Y_\alpha}(t)$ of species *α* within the cell;

$$\text{Eq. 16} \quad \widetilde{Y_\alpha}(t) = \zeta(t)\check{Y}_\alpha^0 + (1-\zeta(t))\hat{Y}_\alpha(t)$$

Where $\check{Y}_\alpha^0$ is the initial average mass fraction of species *α* within the cell in the unmixed part, and $\hat{Y}_\alpha(t)$ is the mass fraction of species *α* within the mixed part that changes according to mass transfer (from the unmixed part) and chemical reaction (generation of products and consumption of reactants). Figure 3 shows a schematic representation of the combustion model within FDS.

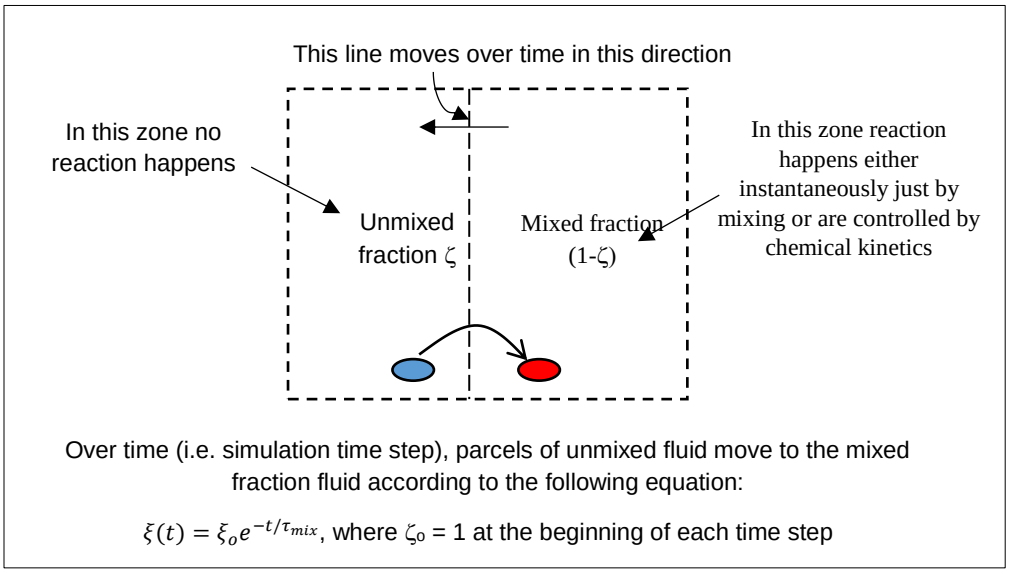

Figure 3. FDS version of EDC

2.3 Soot Model

2.3.1 OpenFOAM

Soot formation is a complicated process of chemical reactions and physical agglomeration of fine particles. It is computationally expensive to use a model that accounts for all the steps of soot formation. Usually an empirical formula is used to calculate the rate of soot formation in each cell. In this work, the Smoke Point Height (SPH) soot formation model is used in all simulations [28]. The SPH correlates experimentally obtained smoke point heights from different fuels to the rate of soot formation via an empirical formula that is also a function of local cell temperature and local fuel mass fraction. In the numerical domain, the soot distribution is governed by the transport equation (Eq. 17). The net soot production rate (Eq. 18) is calculated as the difference between the soot formation rate and soot oxidation rate. Laminar soot formation rate is calculated by the expression in Eq. 27 then modified through coefficients given in Eq. 19, Eq. 21, Eq. 23 and Eq. 25. Laminar soot oxidation rate is also expressed as an empirical function of local cell temperature and local oxygen mass fraction by the expression in Eq. 28. The laminar soot oxidation rate is then modified through coefficients given in Eq. 20, Eq. 22, Eq. 24 and Eq. 26. Shown in Table 2 are the empirical constants for the soot formation and oxidation models.

Table 2. Soot formation and oxidation models constants

Coefficient / Constant	Value	Input file	Location
$\boldsymbol{A_s}$	160000	creatSootFields.H	soot model source code
$\boldsymbol{L_{sp}}$	variable	sootModelProperties	case input files
$\boldsymbol{r}$	2.25	sootModelProperties	case input files
$\boldsymbol{T_a}$	2000	creatSootFields.H	soot model source code
$\boldsymbol{A_0}$	120	creatSootFields.H	soot model source code
$\boldsymbol{E_{a,o}}$	163.54	creatSootFields.H	soot model source code
$\boldsymbol{R}$	0.008314	creatSootFields.H	soot model source code
$\boldsymbol{Z_{s,O}}$	1 Z_{st}	creatSootFields.H	soot model source code or sootModelProperties
$\boldsymbol{Z_{s,f}}$	1.5 Z_{st}	creatSootFields.H	soot model source code or sootModelProperties

$$\text{Eq. 17}\quad \frac{\partial \bar{\rho}\tilde{Y}_S}{\partial t} + \frac{\partial \bar{\rho}\tilde{u}\tilde{Y}_S}{\partial x_j} = \frac{\partial}{\partial x_j}\left[\bar{\rho}\left(D_S + \frac{\upsilon_t}{Sc_t}\right)\frac{\partial \tilde{Y}_S}{\partial x_j}\right] + \bar{\omega}_S$$

Where

- $\tilde{Y}_S$ Is the density weighted mass fraction of soot
- D_S Is the soot diffusivity calculated as the 1% of the gas phase diffusivity
- Sc_t is the turbulent Schmidt number
- $\bar{\omega}_S$ is the net soot production rate

$$\text{Eq. 18}\quad \bar{\omega}_S = \bar{\omega}_{S,f} - \bar{\omega}_{S,ox} \quad kg/s/m^3$$

$$\text{Eq. 19}\quad \bar{\omega}_{S,f} = \kappa_f \omega_{S,f}\ ,$$

$$\text{Eq. 20}\quad \bar{\omega}_{S,ox} = \kappa_{ox}\omega_{S,ox}$$

Where,

- $\bar{\omega}_{S,f}$ is the soot formation rate
- $\bar{\omega}_{S,ox}$ is the soot oxidation rate
- $\omega_{S,f}$ is the laminar soot formation rate
- $\omega_{S,ox}$ is the laminar soot oxidation rate
- κ_f and κ_{ox} are the fractions of reacting zone in each cell for soot formation and oxidation

$$\text{Eq. 21} \quad \kappa_f = \frac{\tau_{c,s,f}}{\tau_{c,s,f}+\tau_{mix}},$$

$$\text{Eq. 22} \quad \kappa_{ox} = \frac{\tau_{c,s,ox}}{\tau_{c,s,ox}+\tau_{mix}}$$

$$\text{Eq. 23} \quad \tau_{c,s,f} = \frac{\rho Y_f}{\omega_{s,f}},$$

$$\text{Eq. 24} \quad \tau_{c,s,ox} = min\left(\frac{\rho Y_{soot}}{\omega_{s,ox}}, \frac{\rho Y_{O2}}{s\omega_{s,ox}}\right)$$

$$\text{Eq. 25} \quad \tau_{mix} = \sqrt{\tau_\eta \tau_{integ}} = \sqrt{\left(\frac{\upsilon}{\varepsilon}\right)^{0.5}\left(\frac{k}{\varepsilon}\right)} \quad sec,$$

$$\text{Eq. 26} \quad k = \left(\frac{3}{2{C_{D1}}^2}\right)^{1/3}(\varepsilon L')^{2/3}$$

Where,

- $\tau_{c,s,f}$ and $\tau_{c,s,ox}$ are chemical time scales for soot formation and oxidation respectively
- τ_{mix} is a mixing time scale
- τ_η is the fine structure / Kolmogorov time scale
- τ_{integ} Is the integral time scale (large scale eddies)
- k is the total kinetic energy

$$\text{Eq. 27} \quad \omega_{S,f} = \begin{cases} \frac{A_s}{L_{sp}}\rho^2\left(Y_{fuel}\frac{Z-Z_{st}}{1-Z_{st}}\right)T^r exp\left(-\frac{T_a}{T}\right) & Z_{s,O} \le Z \le Z_{s,f} \\ 0 & else \end{cases}$$

$$\text{Eq. 28} \quad \omega_{S,Ox} = \begin{cases} A_0[O_2]T^{1/2}exp\left(-\frac{E_{a,o}}{RT}\right) & Z \le Z_{s,O}\ and\ T \ge 1300\ K \\ 0 & else \end{cases}$$

Where,

- A_s is a model constant (formation)
- L_{sp} is the laminar smoke point height
- Z is the local mixture fraction calculated from local fuel and oxygen mass fractions
- Z_{st} is the mixture fraction at stoichiometric air to fuel ratio
- $Z_{s,O}$ and $Z_{s,f}$ are the lower and upper limits of Z for soot formation
- r is a constant exponent
- T_a is a reference activation temperature
- A_0 is a model constant (oxidation)
- $[O_2]$ is the local (each cell) molar oxygen concentration
- $E_{a,o}$ is an activation energy for oxidation

- R is the universal gas constant

2.3.2 FDS

The default approach in FDS for soot generation is predefining the soot mass fraction as a yield (i.e. the fraction of the fuel that is converted into soot). However, in our approach a stoichiometric reaction is defined to determine the mass of soot produced from the combustion of the fuel (i.e. heptane or crude oil). In addition, a step for soot oxidation is added. The two reactions are presented in Figure 4, where “reaction one” is for the fuel combustion (where soot is one of the combustion products) and “reaction two” is a soot oxidation reaction. There is a temperature threshold (1350 K) where the soot oxidation reaction wouldn’t proceed unless the local temperature is higher than this threshold. This way, soot remains in the numerical domain unless the temperature is high enough for soot to be consumed by oxygen.

```
&REAC ID='one', FUEL = 'N-HEPTANE', HEAT_OF_COMBUSTION=44500.,
SPEC_ID_NU = 'N-HEPTANE','AIR','PRODUCTS','SOOT',
NU=-1.,-10.2785,1,0.78/, RADIATIVE_FRACTION=0/
&REAC ID='two', FUEL = 'SOOT', AUTO_IGNITION_TEMPERATURE=1350,PRIORITY=2,
SPEC_ID_NU='SOOT', 'AIR','EXTRA',
NU=-1,-0.925,1/
```

Figure 4. A screenshot from FDS input file

The addition of the soot oxidation step was evaluated by comparing the radiative HRR and the soot mass fraction within the flame before and after the addition of this step. Figure 5 shows that radiation wasn’t affected by the soot oxidation step. Figure 6 shows the soot mass fraction at the centerline of the flame and 0.5 m height for two cases, with and without the oxidation step. The figure shows that, the oxidation step resulted in lower soot mass fraction due to the soot consumption. It can be concluded that, although the addition of the soot oxidation step affected the soot concentration within the flame sheet, it had minimal effect on the radiative heat loss.

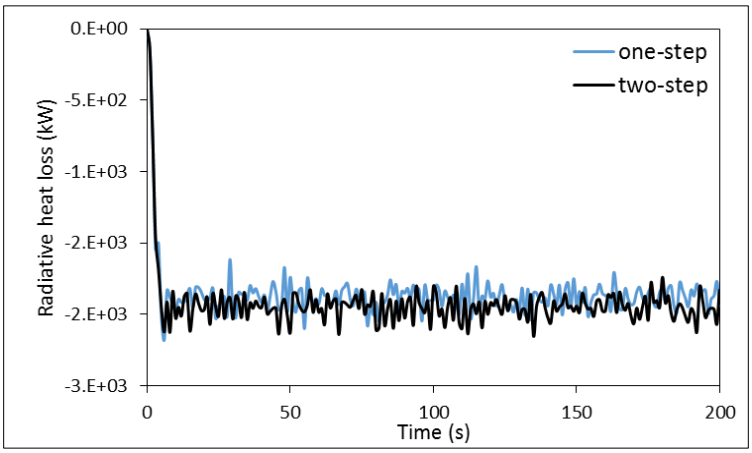

Figure 5. Radiative heat loss comparing the effect of adding the soot oxidation step

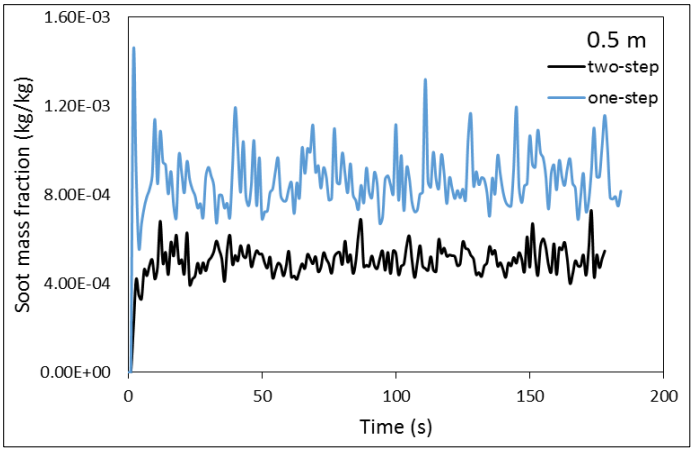

Figure 6. Soot mass fraction at the centerline of the flame and 0.5 height comparing the effect of adding the soot oxidation step

2.4 Radiation Model

2.4.1 OpenFOAM

The non-Grey Weighted Sum of Grey Gases (WSGG) radiation model was used in all simulations to solve the radiative transfer equation. In particular, the WSGG model developed by Cassol *et al*. [29] was used. The WSGG model is a simple model that approximates the total emissivity and absorptivity of a real gas by the sum of several grey gases (where the gas is assumed to have absorption coefficient independent of wavelength) weighted by a temperature-dependent factor.

•The radiative transfer equation (RTE) for each gas in the WSGG model is a function of:

- The gas partial pressure
- The local gas temperature
- The blackbody intensity
- The gas intensity

$$\text{Eq. 29} \quad s \cdot \nabla I_j = \kappa_j p_a \left[a_j(T) I_b(T) - I_j \right]$$

Where

- $s \cdot \nabla I_\lambda(s, x)$ is the solution to the reduced RTE
- κ_j is the absorption coefficient of the j^{th} gas
- p_a is the gas partial pressure
- $a_j(T)$ is the WSGG weighting coefficient of the j^{th} gas and is a function of temperature
- $I_b(T)$ is the blackbody intensity and is a function of temperature
- I_j is the gas intensity of the j^{th} gas

The non-Grey Cassol WSGG model uses four grey gases and a clear gas with the following table of hyper parameters:

Table 3: Cassol WSGG model table of hyper-parameters [29].

	J	k_j	$b_{j,1} \cdot 10^{-1}$	$b_{j,2} \cdot 10^{6}$	$b_{j,3} \cdot 10^{9}$	$b_{j,4} \cdot 10^{12}$	$b_{j,5} \cdot 10^{16}$
CO_2	1	0.138	0.999	6.441	-8.694	4.127	-6.774
	2	1.895	0.0942	1.036	-0.2277	-0.2134	0.6497
	3	13.301	1.4511	-3.073	3.765	-1.841	3.016
	4	340.811	-0.2915	2.523	-2.61	0.9965	-1.326
H_2O	1	0.171	0.6617	5.548	-4.841	2.227	-4.017
	2	1.551	1.1045	0.0576	2.4	-1.701	3.096
	3	5.562	-0.4915	7.063	-7.012	2.607	-3.494

Where hyper parameters $b_{j,i}$ are used as fitting coefficients in the weighting coefficients a_j as

$$\text{Eq. 30} \quad a_j(T) = \Sigma_{i=1}^{5} b_{j,i} T^{i-1}$$

And for the clear gas ($j = 5$),

$$\text{Eq. 31} \quad a_5 = 1 - \Sigma_{j=1}^{4} a_j$$

The input file location for these coefficients in OpenFOAM can be found in the wsggmAbsorptionEmissionCassolBand.H/radiation model source code or in the thermophysicalModels/radiation folder.

The total emissivity is described as:

$$\text{Eq. 32} \quad \epsilon(T,s) = \alpha(T,s) = 1 - e^{\kappa s} \approx \Sigma_{j=0}^{J} a_j(T)\left(1 - e^{-k_j p_a s}\right)$$

Where

- s is a length scale
- k_j is the pressure-absorption coefficient of the j^{th} gas
- p_a is the gas partial pressure

Values of k_j are presented in Table 3.

The radiation model uses the fvDOM discretization method. The number of solid angles (SA) controls the discretization of the RTE equation (Eq. 29). The number of solid angles is described as:

$$\text{Eq. 33} \quad SA = 4\phi\theta$$

Where

- ϕ is number of azimuthal angle divisions in the X-Y plane
- θ is number of polar angle divisions in the Z to X-Y plane

Additionally, radiation is assumed to be much faster than the flow properties, so the RTE only needs to be updated every few time steps. This update frequency of the RTE is a controllable parameter in addition to the number of solid angles, and both are located in the constant/radiationProperties file in the OpenFOAM source files.

2.4.2 FDS

The radiation term in the energy equation is expressed as

$$\text{Eq. 34 } \dot{q}_r''' = \kappa(x)[U(x) - 4\pi I_b(x)]; U(x) = \int_{4\pi}^{0} I(x,s')ds'$$

Where $\kappa(x)$ is the absorption coefficient at location x, I_b is the source term and $I(x, s')$ is the solution of the radiation transfer equation (RTE).

For an incident radiation on an object, the object can either scatter or absorb some of the incident radiation or emit more radiation. All these terms are present in the RTE. However, FDS solves the RTE using a non-scattering assumption (no scattering terms in the RTE) which is a valid assumption when dealing with combustion gases. The absorption coefficient (κ) and source term ($\mathbf{I_b}$) are functions of the absorption wavelength and radiation direction vector (s).

FDS uses a grey gas assumption which implies that an average value for k is used across the whole wavelength spectrum (i.e there is no need to solve the RTE at each wavelength). Hence, k and I_b are no longer a function of the wavelength.

The RTE for non-scattering grey gas is expressed as

$$\text{Eq. 35 } S.\nabla I(x,s) = \kappa(x)[I_b(x) - I(x,s)]$$

Soot is the dominant source and sink of radiation in fires and has a continuous absorption band. In FDS, κ is solved as a mean value using a narrow band model called RadCal [3].

Solving for I_b requires a very fine grid (i.e. small cell size) which is not applicable in large fire simulations. In FDS, I_b is approximated in the grids where the fuel and oxidizer exist; where

$$\text{Eq. 36 } I_b = \begin{cases} \frac{\sigma T^4}{\pi} & outside\ flame\ zone \\ \frac{C\sigma T^4}{\pi} & inside\ flame\ zone \end{cases}$$

And C is a constant calculated at each time step.

Finally to solve the RTE and calculate $I(x,s)$, FDS uses the finite volume method (FVM) where the RTE is integrated over each controlled volume and solid angle (Ω).

Figure 7 shows the RTE control volume with the azimuthal (Φ) and polar (θ) solid angles. Solving for the radiation direction vector (s) requires integration over the whole sphere (4π). The number of θ and Φ angles are correlated in FDS. Different values for the radiative angles (50, 300, 600) where tested in FDS and the effect on the radiative heat loss is shown in Figure 8. It can be seen that, the radiative heat loss wasn't affected by the radiative angles. Runefors et al. [30] discussed that, there is no optimal discretization, and recommended equal number of angles in the azimuthal and angular directions which is handled by FDS as both directions are correlated using a default equation. Thus, the default number of 100 angles was used in all simulations.

3 Experimental setup

This modelling study simulates the tests in the NRC-Sandia fire testing program that was conducted from 2017 to 2020 in the Fire Laboratory for Accreditation of Models and Experiments (FLAME) test cell at SNL (Sandia National Laboratories) [2].

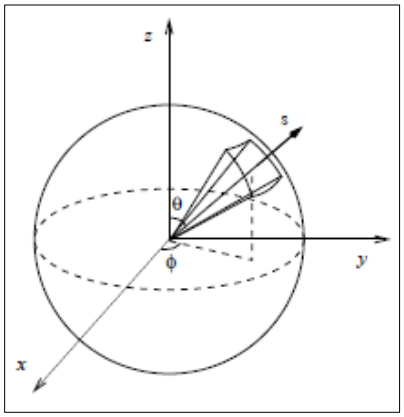

Figure 7. RTE control volume

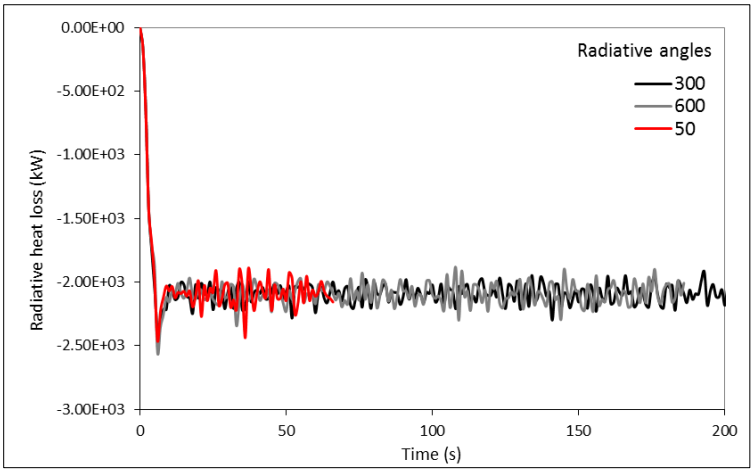

Figure 8. Effect of different radiative angles on radiative heat loss in FDS

To experimentally characterize the thermal environment surrounding a tank car engulfed in crude oil pool fires fueled by different crude oil types, a cylindrical object (calorimeter) representing the tank car at 1/10th scale was built for the fire testing program. The calorimeter did not contain any lading. It was constructed out of two concentric cylinders (inner cylinder and outer cylinder) with a ceramic blanket in between. The calorimeter was instrumented to measure the total heat flux (HF) at various locations along its surface and around its circumference. Detailed description of the calorimeter instrumentation is provided in the test report [2]. A cylindrical calorimeter (with a diameter of 0.3 m and a length of 1.8 m) was placed above a 2-m diameter pool fire (see Figure 9).

The pool fire was fueled by heptane, Bakken crude oil or diluted bitumen (dilbit) crude oil. Bakken and dilbit crude oils were selected to investigate the impact of fuel characteristics on the fire behaviour. Bakken crude oil contains higher concentrations of dissolved gases and light-end, volatile hydrocarbons, and dilbit crude oil is among the heaviest varieties of crude oil

transported in Canada. Heptane was also tested to provide baseline data against which the Bakken and dilbit test results could be compared.

The burning behaviour of the fuels was investigated by measuring the fuel mass burning rate, flame height, heat release rate (HRR), plume temperatures, fuel layer temperatures, flame surface emissive power (SEP) and incident heat flux at a distance away from the fire.

The study also investigated effects of the presence and placement of the calorimeter at different heights above the fuel surface, different fuel supply temperatures, and different methods of feeding the fuel to the pan (allowing the fuel to burn down versus maintaining a constant fuel depth) on the fire characteristics.

Figure 9. Experimental test set-up

3.1 Experimental uncertainty

It is important while validating the numerical model results to take into account experimental uncertainty. Unfortunately, there is no simple way or a single value to gauge experimental uncertainty. It is also important to differentiate between experimental uncertainty and fluctuations in the reported experimental results. For example in the NRC-Sandia experiments, the error bars on all values reported in Section 8 (Comparison of test series) are not uncertainties [2]. They represent the variability or fluctuations around an average value.

In a technical note published by the National Institute of Standards and Technology (NIST), McGrattan *et al.* [31], discussed the topic of experimental uncertainty and fire model validation. McGrattan *et al.* [31] indicated that experimental uncertainty could be a combination of the measuring instrument accuracy and a propagated uncertainty of input parameters (boundary conditions) to the numerical model that are taken from the experiments. For example, in this study, the fuel burning rate is an input parameter that is taken from the experiments. The uncertainty in this burning rate is propagated throughout the model affecting all validation parameters. For example if the actual burning rate is less than reported, even if the numerical model is 100% accurate, the numerical plume centerline temperature profile will overpredict the experimental results. This “propagated uncertainty” is an addition to the uncertainty of the measuring instrument itself, the Centerline thermocouples, in this example.

Some other validation parameters come from 2 or more measurements: for example the HRR is calculated from measurements of a flow rate and concentrations of gaseous combustion products. Each measurement has its level of uncertainty. From a statistical point of view not all these uncertainties will always give the worst case or the most error in the reported value. A distribution of errors and uncertainties is expected because not all instruments will underpredict or overpredict by their maximum deviation all the time. Some will be accurate, some will deviate by a little and some will deviate by a lot. That's why, one of the lessons learned from McGrattan *et al.* [31] is "Quantity makes up for quality", meaning that validating the same model against a large number of data points from a large number of experiments makes up for the unreported uncertainties in experimental measurements. Following the same school of thought, in this study, a large number of parameters were chosen to assess the model. The idea is to look at the model from different aspects and get a more complete picture of its capabilities.

Another lesson learned by McGrattan *et al.* [31] is that "some parameters are more difficult to predict than others". For example, heat flux is more difficult than temperature. That was proven true in this study; in almost all cases wide angle heat flux and narrow angle heat flux consistently were overpredicted.

Another source of discrepancy between numerical and experimental results has to do with the level of details that could be included in the numerical model. For example the support holding the calorimeter in place, the bundles of thermocouples coming out of the calorimeter and the supports holding the measuring instruments were not included in the numerical domain. Those obstacles, although seemingly irrelevant, might slightly alter the flow profile around the calorimeter. However, considering the marginal gain from including a very complicated geometry and the possible computational problems (such as numerical instability), these details were not included in the domain.

With the above discussion in mind, some quantitative values for experimental uncertainties are reported in Table 4.

Table 4. Examples of uncertainty values from experimental measurements [31]

Measurement	Relative uncertainty
Plume temp	14%
Pressure	40-80%
Heat flux	20%
HRR	15%

4 Cases Setup

Discussed in this section are the details for the numerical simulations setup:

1. The domain
2. The mesh
3. Boundary conditions

Six simulations were conducted. Each simulation is a numerical model of a test conducted by the NRC at Sandia National Laboratories (see Table 5).

Table 5. Numerical cases and equivalent experimental tests

Numerical case	Experimental test	Experimental conditions
Heptane with calorimeter	Test # 1.1	Constant supply of fuel @ ~20°C, calorimeter @ 1m height
Heptane without calorimeter	Test # 1.2	Constant supply of fuel @ ~20°C, no calorimeter
Bakken with calorimeter	Test # 2.5	Constant supply of fuel @ ~20°C, calorimeter @ 1m height
Bakken without calorimeter	Test # 2.1	Constant supply of fuel @ ~20°C, no calorimeter
Dilbit with calorimeter	Test # 3.5	Constant supply of fuel @ ~20°C, calorimeter @ 1m height
Dilbit without calorimeter	Test # 3.3	Constant supply of fuel @ ~20°C, no calorimeter

4.1 OpenFOAM Domain

Shown in Table 6 are the components included in the numerical domain and their dimensions. Shown in Figure 10 are the components and the numerical domain. It is important to note that this is a simplified geometry of the Sandia facility and doesn't include all the details of the actual experimental facility. For example, the domain doesn't include the facility walls. The domain extends only to the edge of the steel plate in the experimental setup. Hence the sides, in the numerical domain, are assumed to be open to atmospheric conditions. Also, calorimeter support, measuring devices and conduits housing thermocouples are not included in the domain.

Table 6. Domain components and dimensions

Component	Dimensions
Domain boundaries	12 m Dia. × 8 m Height
Steel floor	12 m Dia.
Fuel pan	2 m Dia. × 0.3 m Depth
Fuel	2 m Dia.
Top	12 m Dia.
Calorimeter	0.33 m Dia. × 1.8 m Length

4.2 OpenFOAM Mesh

Shown in Table 7 are the details of the mesh parameters: refinement levels, cell sizes and number of cells at each refinement level. There are 4 refinement levels to the base mesh (level 0). Each refinement level reduces the initial size by a factor of 2. The finest level for the gas phase (level 3) has cell sizes of 2 cm. Most cells (~75%) are in this level, where the flame is expected to be. Level 4 (cell size 1 cm) was created just to resolve the baffles/brackets supporting the calorimeter cylinders. These cells are only located only on the calorimeter surface. Shown in Figure 11 are different levels of refinement for the mesh.

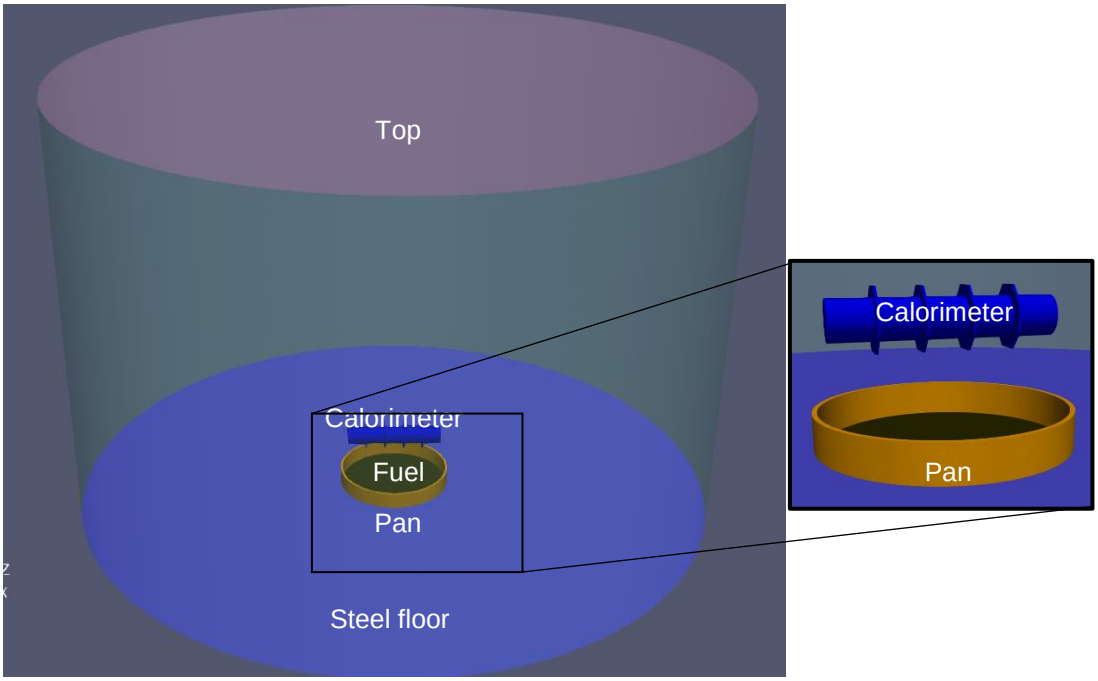

Figure 10. Simulations domain

Table 7. Mesh information

Geometry	Refinement Level	Cell size	Number of cells (with Cal. / without Cal.)
Outer cylinder (12 m Dia. × 8 m Height)	0	0.16 m	121,381 / 121,390
Middle cylinder 1 (8 m Dia. × 8 m Height)	1	0.08 m	478,456 / 478,412
Middle cylinder 2 (5 m Dia. × 8 m Height)	2	0.04 m	1,569,636 / 1,569,656
Inner cylinder (3 m Dia. × 8 m Height)	3	0.02 m	7,002,381 / 7,036,920
Calorimeter surface	4	0.01 m	113,816
Total			9,285,670 / 9,206,378

4.2.1 Grid Size Selection

Grid size was determined based on two (2) criteria: the Plume Resolution Index (PRI) and a preliminary grid sensitivity analysis. PRI is defined by Eq. 37. Higher PRI values correspond to a more resolved simulation. Values in the range of 5-15 have been proven to be sufficient [4], [32] while values up to 40 are recommended for 1-m diameter pool fires [33]. Wen *et al.* [34] used PRI values ranging from 9 to 17 for a 30.5 cm diameter pool fire in FDS. For the same pool size, Chen *et al.* [26] resolved the domain to PRI values of 33-66 using OpenFOAM. Maragkos *et al.* [35], resolved a 1-m diameter methane pool fire to PRI values of 84-102. In this study, the mesh was resolved to a PRI range of 75 to 91. Other parameters used to gauge the resolution of the mesh are presented in Table 8.

$$\text{Eq. 37} \quad PRI = \frac{D^*}{\Delta x}, \quad D^* = \left(\frac{\dot{Q}}{\rho_\infty c_p T_\infty \sqrt{g}}\right)^{2/5}$$

Where

- PRI is the Plume Resolution index
- D^* is the characteristic fire diameter
- Δx is the cell size in the fire zone

A preliminary mesh sensitivity analysis was conducted. The parameter chosen to check for grid size independence was the plume centerline temperature. The study was conducted for cell sizes of 8-cm, 5-cm, 3.5-cm and 2-cm in the inner cylinder mesh zone (core domain zone). The simulation case was a heptane 2-m diameter pool fire without the calorimeter. Shown in Figure 12 are the results from each mesh size. It was clear that the gain by reducing the grid size to less than 2-cm will be marginal; the centerline temperature obtained from the 3.5-cm simulation is very close to that obtained to the 2-cm simulation. To be on the safe side, the 2-cm grid size was chosen moving forward for all simulations.

Table 8. Examples for PRI values from the literature and other mesh related parameters

Study	PRI	Number of cells across the fire source	Cell size in flame zone (m)	Fire size
Current study	75, 76, 80, 83, 87, 91	100	0.02	3.1 – 5.1 MW
Maragkos *et al.* [35]	84-102	66	0.015	1.59 – 2.61 MW
Chen *et al.* [26]	33-66	48-96	0.00317 - 0.0063	22.5 kW
Wen *et al.* [34]	9-17	12-25	0.022-0.033	24.6 kw

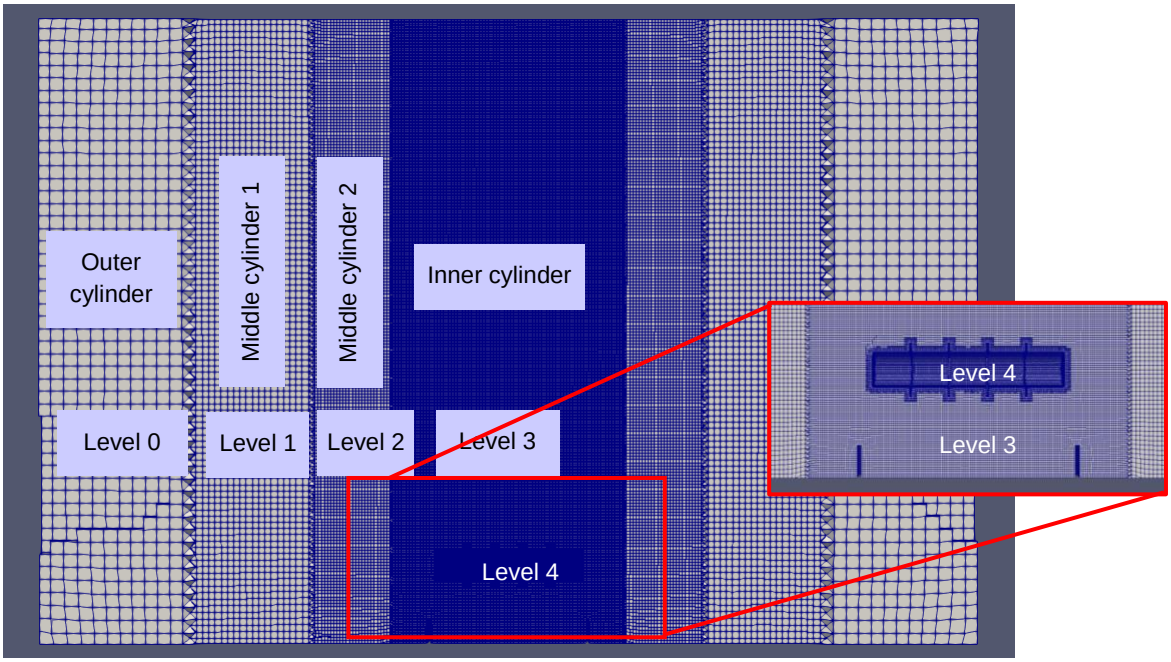

Figure 11. Mesh refinement levels

4.3 OpenFOAM Boundary Conditions (BC)

Shown in Table 9 are the flow BCs and temperature BC at each surface of the domain. The fuel BCs are reported separately in

Table 10. Flow and temperature BCs of the fuel surface are imposed in the numerical model. The flow rate for each case is obtained from the experimental burning rate from corresponding tests. The fuel enters the domain as a gas/vapour phase with properties corresponding to those of an ideal gas. The temperature at which the fuel enters the domain is obtained from the approximate fuel surface temperatures measured in the experiments. Despite the fluctuations in the measured experimental burning rates and fuel surface temperatures, the numerical flow rates and temperatures were kept constant, in order to minimize the complexity of the numerical model.

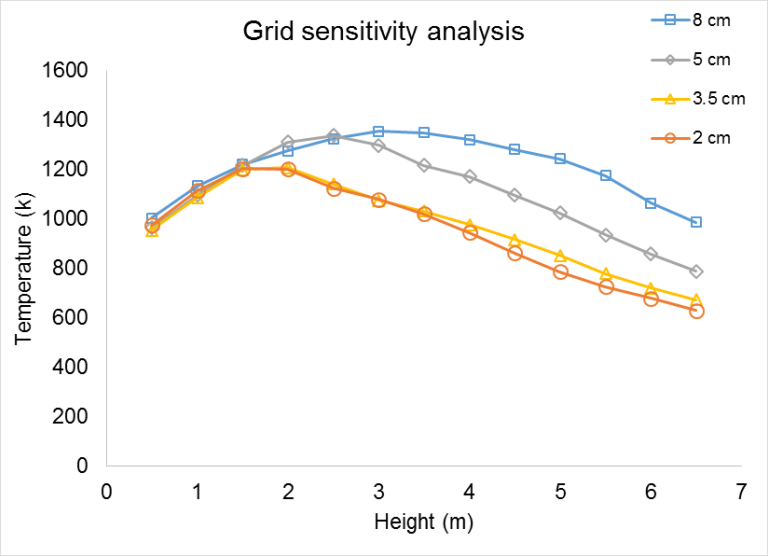

Figure 12. Grid size sensitivity analysis.

Given the complexity of the crude oil chemical composition, a surrogate made up of known gas phase fuels were used to model the volatiles generated from Bakken and dilbit, as shown in Table 10. The Bakken surrogate was made up mostly of heptane with some acetylene. The dilbit surrogate was made up of a heavier gas phase fuel with some acetylene. The fuel used for dilbit has twice the molecular weight (and consequently twice the gas phase density) of heptane but with the same heating value.

Table 9. Boundary conditions

Surface	Flow/velocity BCs	Temperature BC
Side boundaries	Open inlet/outlet	Ambient (298 K)
Steel floor	Zero flow/no-slip	Zero gradient (adiabatic)
Fuel pan	Zero flow/no-slip	Zero gradient (adiabatic)
Top	Open inlet/outlet	Ambient (298 K)
Calorimeter	Zero flow/no-slip	Zero gradient (adiabatic)

Table 10. Fuel boundary conditions

Surface	Flow/velocity BC [2]	Temperature BC [2]	SPH [36]	Notes
Fuel	Constant flow (with cal. / no cal.) (kg/sec)	Approx. fuel level temp. (K)	SPH (m) Heptane/acetylene	Composition used in the model
Heptane	0.114 / 0.1264	373	0.123/0	100% heptane
Bakken	0.08168 / 0.11	473	0.123/0.019	97.5% heptane / 2.5% C_2H_2
Dilbit	0.055 / 0.05	573	0.123/0.019	96% $C_{14}H_{32}$ / 4% C_2H_2

The logic behind selecting the surrogate composition is to add to the fuel flow a “sooty fuel”, namely acetylene, which has a short smoke point height (SPH) to generate more soot and a higher radiative heat fraction in order to match the experimental radiative heat fraction. Having said that, the maximum radiative heat fraction that was obtained from the surrogate composition was ~ 44%, which was in line with the maximum radiative fraction found in a study by De Ris [37]. The study investigated the relationship between SPH and radiative fraction and found that the maximum fraction is around 43%.

After several numerical iterations, it was found that the maximum radiative fraction corresponded to an acetylene percentage of ~ 4%. Hence, the percentage was selected for the dilbit surrogate. However, the acetylene percentage in the Bakken surrogate was assumed based on a preliminary experiment conducted for Bakken and dilbit in a cone calorimeter test. The test indicated that dilbit yielded slightly higher soot yield than Bakken. In another numerical simulation, where the fuel flow rate was kept constant, 2.5% acetylene yielded a slightly lower soot yield than the 4% acetylene surrogate, while maintaining the same radiative fraction.

The reason for using heptane as the main fuel for the Bakken surrogate is that Bakken has a high content of light end hydrocarbons. While a fuel with double the gas phase density was used for dilbit to account for the possibility that the volatiles from dilbit pyrolysis would be heavier than those from heptane or Bakken, this might have an effect on the flame shape. Selecting a gas / vapour phase with “double the density” is an assumption, and further gas phase analysis of the volatiles evolving from the crude oil pool is necessary to obtain a more accurate chemical surrogate for the numerical simulations.

4.4 FDS Domain

Figure 13 shows the domain used in the FDS simulations. The domain dimensions are 20 m length, 20 m width and 12 m height. The pool fire is represented by a circle 2 m in diameter and surrounded by a steel plate 14 m in diameter to replicate the experimental setup. In the simulations with the calorimeter, a solid cuboid of cross section 0.3 m by 0.3 m and 1.8 m length is placed at the centre of the domain and at a 1 m height above the pool. It should be noted that FDS uses a rectilinear mesh and can’t have curved structures in the domain. That’s the reason a cuboid calorimeter was built in the domain instead of a cylindrical one. This is likely the main

drawback of FDS that resulted in the poor agreement between the experimental and numerical temperatures on the surface of the calorimeter and its surrounding (see Section5).

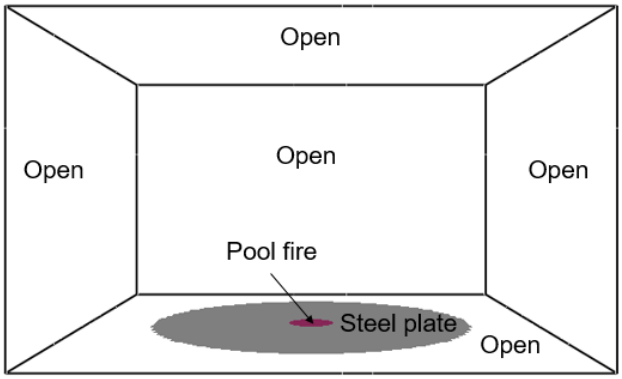

Figure 13 FDS domain

4.5 FDS Mesh

Simulations with different mesh sizes were first conducted to reach mesh convergence. Five mesh sizes were tested. Three of them are of equal cell size across the whole domain: 5 cm, 10 cm and 20 cm. Mesh 1 has cell sizes 2 cm, 10 cm and 20 cm while Mesh 2 has cell sizes 5 cm, 10 cm and 20 cm. In Mesh 1 and 2, the smallest cell size is used in the flame zone (i.e. center of the domain) in order to capture the flame characteristics. Table 11 shows the total number of cells and number of processors used in each mesh.

Table 11. Different meshes tested

Cell size	5 cm	10 cm	20 cm	Mesh 1	Mesh 2
No. of cells	32e6	5e6	6e5	8.98e6	1.72e6
Processors	500	500	75	227	50

The criteria used to determine the mesh convergence is the radiative heat loss, since radiation is the most important mode of heat transfer in fire. Figure 14 shows the radiative heat loss from the simulations of the five (5) meshes. The 5 cm mesh, Mesh 1 and Mesh 2 resulted in the same radiative heat loss. Since Mesh 2 requires the least computational resources, it was used for all the simulations.

4.6 FDS Boundary Conditions

As seen in Figure 13, the sides and top of the domain are simulated as open boundaries to represent an open crude oil fire. Both the steel plate and the calorimeter are simulated as adiabatic surfaces. The fuel mass flux is imposed in the simulations from the experiments. Similar to OpenFOAM simulations, a surrogate of 2.5% acetylene (C_2H_2) and 97.5% heptane (C_7H_{16}) is used to simulate Bakken and another of 4% C_2H_2 and 96% C_7H_{16} is used to simulate dilbit. Table 12 shows the total mass flux and composition used in the simulations.

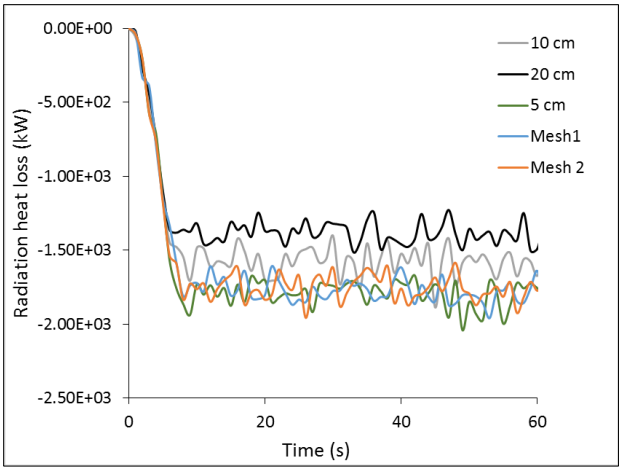

Figure 14. Radiative heat loss using the 5 meshes tested

Table 12. Mass fluxes and compositions used in the simulations

Simulation	Experimental test	Total mass flux ($kg/m^2.s$)	Composition
Heptane without calorimeter	Test 1.2	0.04	C_7H_{16}
Heptane with calorimeter	Test 1.1	0.037	C_7H_{16}
Bakken without calorimeter	Test 2.1	0.03	2.5% C_2H_2 + 97.5% C_7H_{16}
Bakken with calorimeter	Test 2.5	0.027	2.5% C_2H_2 + 97.5% C_7H_{16}
Dilbit without calorimeter	Test 3.3	0.016	4% C_2H_2 + 96% C_7H_{16}
Dilbit with calorimeter	Test 3.5	0.018	4% C_2H_2 + 96% C_7H_{16}

5 Results and Discussion

The parameters chosen to validate the results of the OpenFOAM results are:

1. Plume centerline temperature
2. Exterior to calorimeter temperature
3. Radiative fraction
4. Heat flux to calorimeter
5. Calorimeter temperature
6. HRR
7. Soot yield
8. Temperature contours
9. Wide angle HF
10. Narrow angle HF
11. Flame height

Locations of the measurements in the numerical domain are shown in Figure 15. At this point it is important to point out some differences between the methods used to calculate some parameters, in the numerical model and the way they are measured in the experiments:

- The calorimeter was modeled as an empty object in the domain without any thermal mass; it was set as an adiabatic boundary surface. No conduction heat transfer through/into the calorimeter or along its walls is considered. Experimentally, the calorimeter will conduct heat along its walls, which will result in closer temperature values on its surface compared to the numerical results.
- Numerically, the heat flux to the calorimeter is estimated by calculating the total incident heat flux to the calorimeter which is obtained by solving the RTE equation (Eq. 29). Experimentally, the total heat flux to the calorimeter was calculated by measuring the emitted heat from the calorimeter surface (i.e. with the calorimeter surface temperatures estimated based on the measured temperatures on the unexposed side of the outer calorimeter shell) and calculating the absorbed heat into the calorimeter (i.e. calculated based on the temperature difference between the calorimeter outer cylinder and the outer surface of the inner cylinder).
- Numerically, the wide angle heat flux is estimated by calculating the incident heat flux at the boundaries of the domain (i.e. far from the flame), which is 6 m away from the center of the pool. Experimentally, the wide angle heat flux is measured using a total heat flux gauge with a 180° view angle at 9 m away from the center of the pool. This will lead to an overprediction of the wide angle heat flux in the numerical model.
- Numerically, the narrow angle heat flux is estimated by sampling the radiation field close to the flame (i.e. at a distance 1.1 m from the pool center). In the numerical model, all wavelengths are considered using the WSGG radiation model. Experimentally, a 5.5^{o} view angle radiometer with a zinc selenide window was used. The zinc selenide window has 70% transmissivity in the wavelength range 2 ~ 20 μm and zero transmissivity outside this range.
- Numerically the flame height is defined by the highest point, in the domain, at which there is a nonzero value of the fuel concentration. Experimentally, the flame height is obtained using time-averaged images from an IR camera.

For the FDS, six simulations were conducted and the results are presented and discussed in this section. The parameters used for validation are:

1. Centerline (plume) temperature
2. Exterior to calorimeter temperature
3. Radiative fraction
4. Heat flux to calorimeter
5. Heat release rate (HRR)
6. Temperature contours
7. Wide angle HF
8. Flame height

The centerline temperatures are measured by simulated thermocouples located at the same experimental locations. Similar to the experiments, 3 sets of thermocouples are used to measure the temperatures surrounding the calorimeter at 51 mm away from the calorimeter surface; at the central plane, left and right planes of the calorimeter. Each set consists of 8 thermocouples which are arranged as shown in Figure 16. Although the surrounding thermocouples could have been be arranged in circular pattern in FDS, they are arranged in

rectangular pattern, to keep an equal distance between each thermocouple and the surface of the cuboid calorimeter in FDS domain.

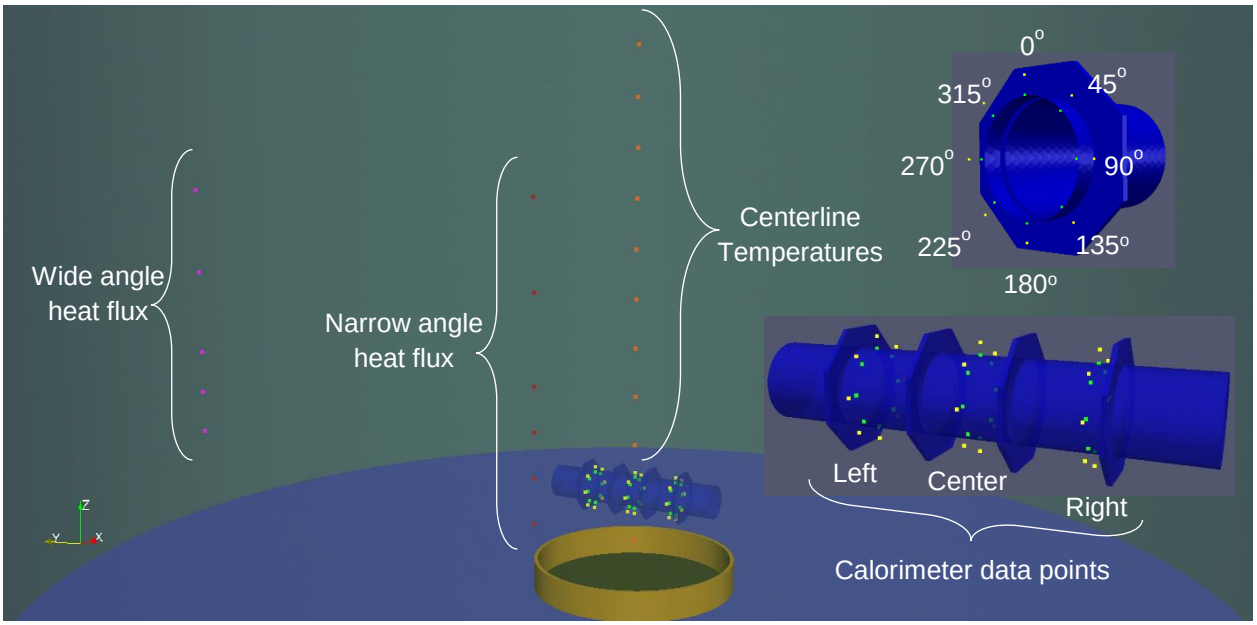

Figure 15. Locations of post processing points in the domain

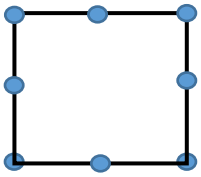

Figure 16. Locations of thermocouples surrounding the calorimeter (blue circles)

Similar to OpenFOAM, the wide angle radiometer is simulated as a heat flux gauge located at 6 m from the center of the flame. Experimentally, total heat flux gauges with a 180° view angle, located 9 m away from the centerline of the pool were used. The flame height, from FDS simulations, was estimated visually by monitoring the flame in FDS rendering tool, Smokeview.

Eight parameters are used for validation from FDS simulations compared to 11 from OpenFOAM. The three missing parameters are; narrow angle HF, soot yield and the temperature contours. FDS doesn't have the capability of measuring the narrow angle heat flux. Because soot yield wasn't measured experimentally, no device was added in the FDS simulations to calculate it.

Calorimeter temperature and heat flux to the calorimeter results are presented as contours rather than point values as in the experimental or OpenFOAM results. Given the significant difference in the calorimeter representation in FDS from the experiment, a qualitative comparison through contours was used instead of point value comparison.

Discussed in the next subsections (5.1 to 5.6) are the numerical results of the abovementioned parameters in comparison with the experimental results.

5.1 Heptane with Calorimeter

5.1.1 OpenFOAM Results Summary

Discussed in this section are the validation results for the “heptane with calorimeter” case. Numerical results are compared to experimental results from the NRC experiment at Sandia National Lab (Test 1.1) [2] [38]. Summaries of the numerical and experimental ranges are shown in Table 13.

Table 13. Results summary for the heptane with calorimeter simulation from OpenFOAM

Section	Validation parameter	Numerical range	Experimental range	Comments
5.1.3	Centerline temperature	238 – 1039°C	396 – 876°C	Good agreement given absence of a boiling model
5.1.4	Exterior to calorimeter temperature	608 – 1181°C	805 – 946°C	Good agreement given absence of a boiling model
5.1.5	Radiative fraction	38%	36%	Good agreement
5.1.6	Heat flux to calorimeter	82.3 – 151.5 kW/m^2	10.2 – 82.4 kw/m^2	Good agreement given absence of a boiling model
5.1.7	Calorimeter temperature	517 – 1258°C	751 – 875°C	
5.1.8	HRR	4.1 MW	4.4 MW	Good agreement
5.1.5	Soot yield	8 %	Not reported	
5.1.9	Temperature contours	750 – 1150 K	750 – 1150 K	
5.1.11	Wide angle HF	2.8 – 6.2 kW/m^2	2.2 – 2.9 kW/m^2	Overestimated
5.1.12	Narrow angle HF	37 – 109 kW/m^2	33 – 93 kW/m^2	Overestimated
5.1.13	Flame height	2.2 m (with pan) 3.5 m (no pan)	5.6 m	Different criteria

5.1.2 FDS Results Summary

The FDS results from simulating the heptane with calorimeter case are summarized in Table 14. Further discussion about each parameter is provided in the following subsections.

Table 14. Results summary for the heptane with calorimeter simulation from FDS

Section	Validation parameter	Numerical range	Experimental range	Comments
5.1.3	Centerline temperature	500 - 790°C	396 – 876°C	Good agreement given absence of a boiling model
5.1.4	Exterior to calorimeter temperature	122 – 847°C	805 – 946°C	Under-predicted
5.1.5	Radiative fraction	39%	36%	Good agreement
5.1.6	Heat flux to calorimeter	7.46 – 111 kW/m^2	10.2 – 82.4 kW/m^2	Reasonable agreement considering the different calorimeter geometries
5.1.7	Calorimeter temperature	633 – 1073°C	751 – 875°C	Reasonable agreement considering the different calorimeter geometries
5.1.8	HRR	5.5 MW	4.4 MW	Overpredicted
5.1.11	Wide angle HF	2– 3 kW/m^2	2.2 – 2.9 kW/m^2	Well predicted
NA	Flame height	5.8	5.6 m	Both are visually measured

5.1.3 Plume Centerline Temperature

5.1.3.1 OpenFOAM

Shown in Figure 17 are the transient centerline temperatures from (a) the numerical simulations and (b) the experiments [2]. It is important to point out that the x-axis units for the numerical results are “seconds” while the experimental x-axis units are “minutes”. The reason experimental results take minutes to reach a steady values is the thermal mass of objects in the experiment and the burn hall: the calorimeter, the steel floor, the burn hall walls and the fuel pan. In the numerical model, there is no thermal mass model for any solid object in the domain. All these objects are omitted volumes from the domain or just surfaces with specific boundary conditions. Shown in Figure 18 are the steady state centerline temperatures: a) Temperature versus height and b) Height versus temperature [38]. There are two numerical results; the blue line is for the original case with the fuel pan in the domain. The green line is for a modified domain where the pan is not included in the domain. Unlike Bakken and dilbit cases, in the case of heptane we observed some discrepancies between the numerical and experimental results. Some results from a modified domain with the pan excluded are introduced in some figures to explain the possible reason for that discrepancy. The centerline plume temperature profile of the numerical simulation is similar to that of the experiments. However, the numerical simulation range is wider than the experimental range; the upper temperature limit from the numerical simulation is ~ 14 % higher than the upper temperature limit from the experiments. The numerical lower limit is ~ 23% lower than that of the experimental lower limit (see Figure 18). In the modified domain with the pan excluded from the domain, the numerical centerline temperature matches the experimental trend better, showing the same profile but consistently shifted by ~ 200°C (see Figure 18). A possible explanation is discussed in Section 5.1.7 after exploring the most important parameters for validation.

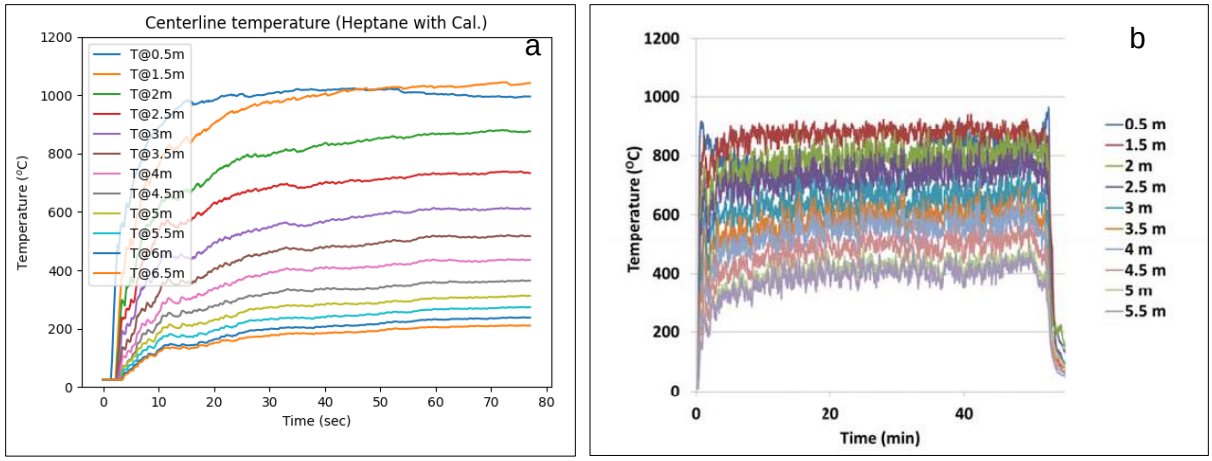

Figure 17. Centerline temperatures at different heights (heptane with calorimeter with pan): a) Numerical, b) Experimental.

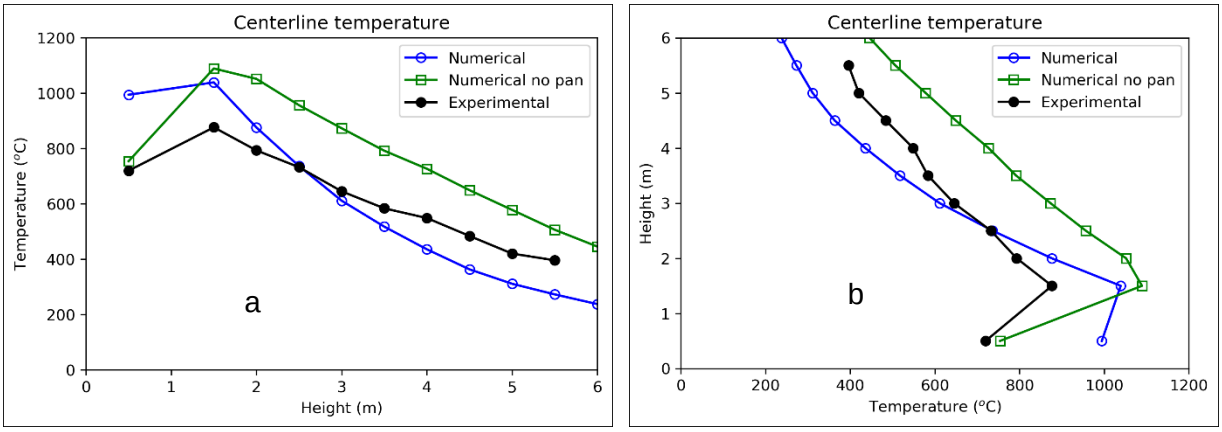

Figure 18. Average centerline temperatures at different heights: a) Temp. vs. Height b) Height vs. Temp.

5.1.3.2 FDS

The results from simulating heptane with the calorimeter are compared against the experimental results from Test 1.2. Figure 19 shows the experimental and numerical temperatures at the centerline of the flame. The range of temperatures in the simulations is 500-790 °C, while the experimental range is 396-876 °C. Good agreement can be seen between the two sets.

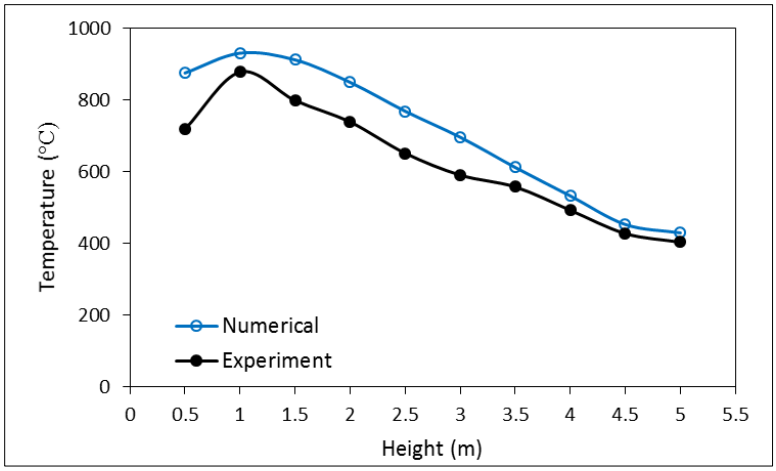

Figure 19. Average flame temperature at the centerline of the pool for heptane pool fire with the calorimeter from the experiments and simulation

5.1.4 Exterior to Calorimeter Temperature

5.1.4.1 OpenFOAM

Shown in Figure 20 are the transient exterior to calorimeter temperatures from a) the numerical simulation and b) the experiment [2]. Shown in Figure 21 are the steady state values at different angles for both numerical and experimental results [38]. The difference between Figure 21a and Figure 21b is that the numerical results in “a” are the results where the pan is included in the domain while “b” are the numerical results from the model without a pan in the domain.

From the model where the pan is included in the domain (Figure 21a) the numerical results in the center plane overestimated the surrounding temperature everywhere. The numerical results matched the experimental results on the left and right side of the calorimeter except the data point on top of the calorimeter. From the numerical model without the pan (Figure 21b), there is a better agreement on the center plane and a slight underestimation on the right and left planes from the numerical model.

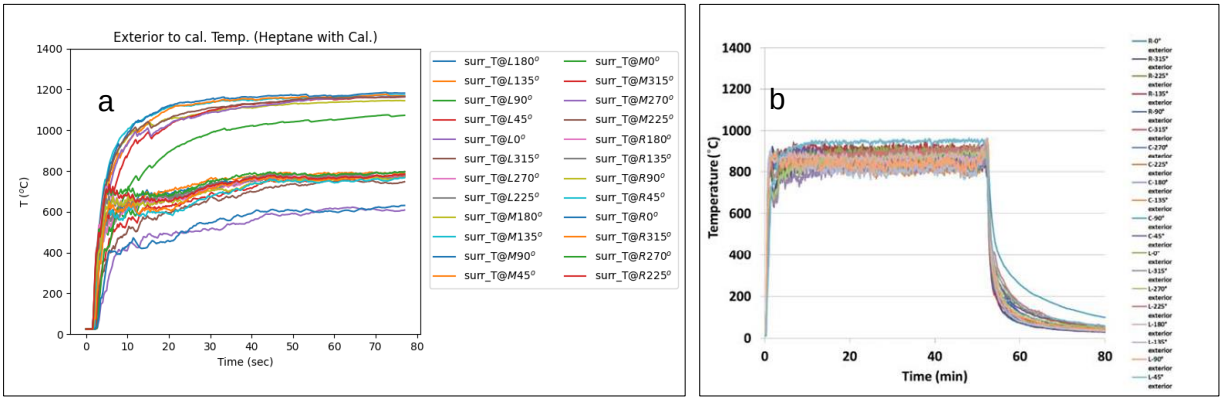

Figure 20. Exterior to calorimeter temperatures (°C) at different angular-positions: a) Numerical, b) Experimental.

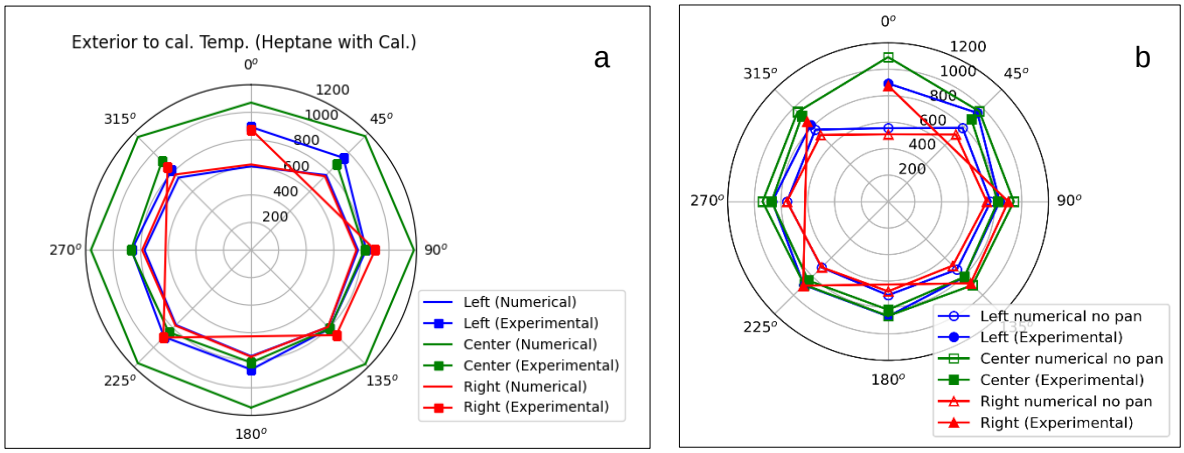

Figure 21. Spider plot of exterior to calorimeter temperatures (°C) at different angular-positions a) pan included in the numerical model b) pan not included in the numerical model

5.1.4.2 FDS

Figure 22a presents the temperature values surrounding the calorimeter from the simulations as raw data. Figure 22b presents the experimental data. Figure 22c presents the time-averaged values from the numerical model. Note that the drop in the experimental data is due to the ending of the experiment. The experimental range is 396-876 °C while the numerical range is 122-847 °C. Basically the lower temperatures in the simulations are seen at the thermocouples located at the side planes.

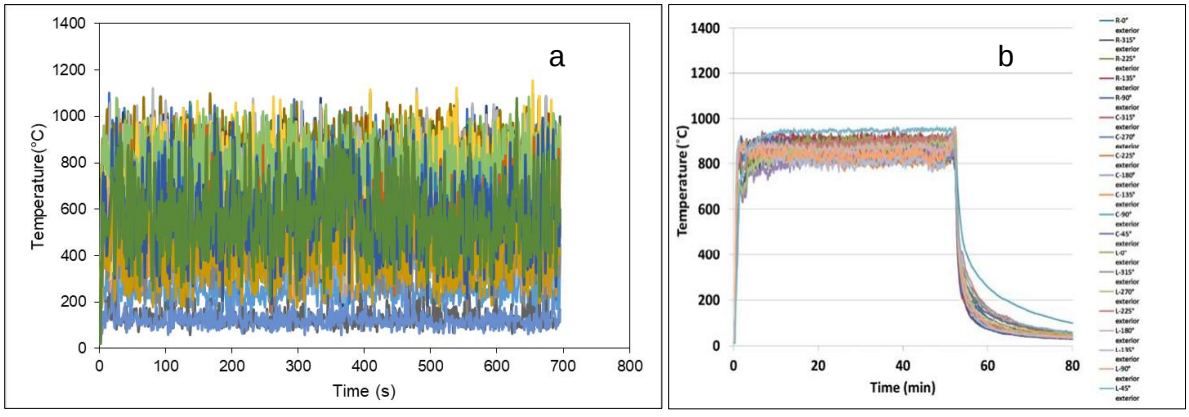

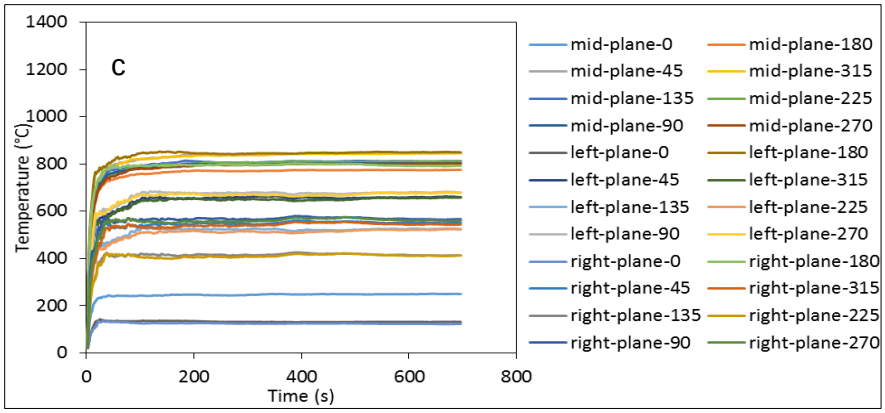

Figure 22. Temperatures surrounding the calorimeter from heptane pool fire from a) simulation (raw data), (b) experimental and c) time-averaged data (numerical)

The spider plot comparing the average temperatures surrounding the calorimeter at different angles and planes from the simulation and experiment is shown in Figure 23. The numerical temperatures at the left and right planes are greatly lower than the experimental one. The simulated temperatures at the central plane are in good agreement with the experimental temperatures, except for the temperature above the calorimeter. The lower temperatures measured numerically might be attributed to; (1) the calorimeter has a squared cross section in the model due to the rectilinear mesh requirement in FDS, where the sharp corners of the square lead to the separation of the flame from the calorimeter surface and decrease the heat transfer to the calorimeter, (2) the absence of baffles in the simulations, where baffles guide the flow of the hot gases over the calorimeter allowing their spread on the calorimeter and reaching the side planes, (3) in the experiments, the calorimeter external thermocouples are attached to the calorimeter through a steel rod.

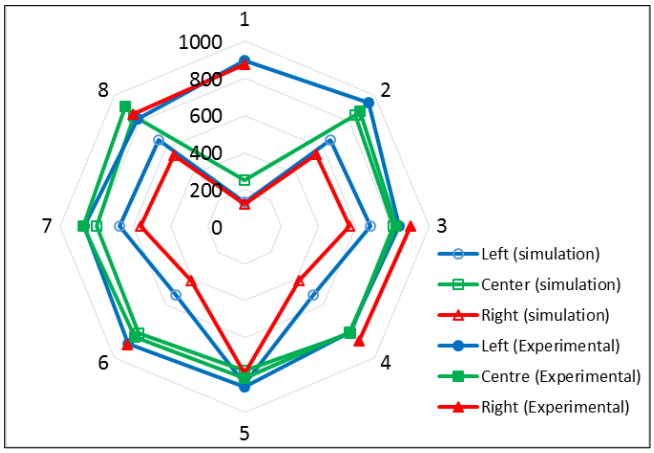

Figure 23. Spider plot of exterior to calorimeter temperatures (˚C) at different angular-positions

5.1.5 Radiative Fraction & Soot Yield

5.1.5.1 OpenFOAM

Shown in Figure 24 is the radiative heat fraction and the soot yield from the numerical simulation. There is good agreement between numerical and experimental results in terms of radiative fraction: Average radiative fraction from the numerical simulation was ~38%. Average radiative fraction from the experiments was 34~39%. Average soot yield from numerical simulation was 8%. No soot yield was measured during the experiment.

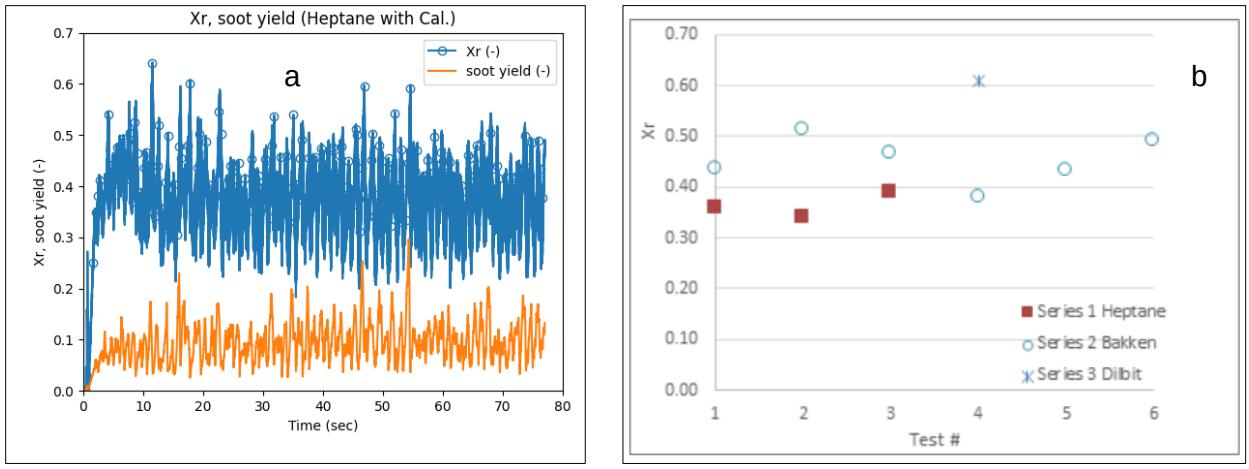

Figure 24. a) Numerical radiative fraction and soot yield results. b) Experimental radiative fraction.

5.1.5.2 FDS

The numerical radiative fraction (X_r) from FDS simulations for the heptane with calorimeter case is shown in Figure 25. The average X_r is 39%, which is in reasonable agreement with the experimental value (36%).

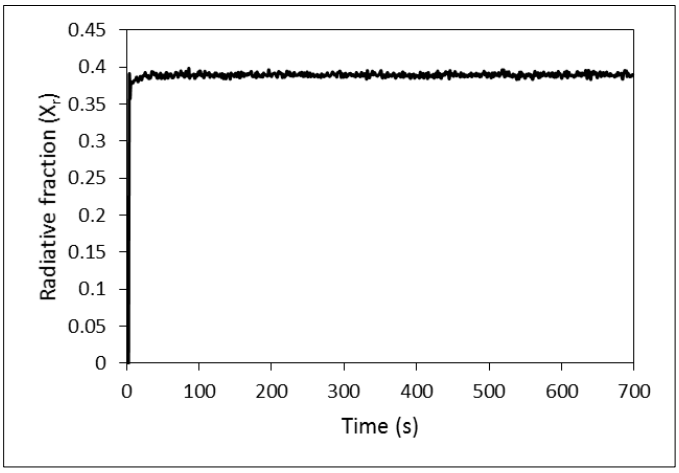

Figure 25. Numerical radiative fraction for heptane with calorimeter simulation in DS

5.1.6 Heat Flux to Calorimeter

5.1.6.1 OpenFOAM

Shown in Figure 26 are the transient heat fluxes to the calorimeter from a) the numerical simulation (pan included in the domain) and b) the experiment [2]. The numerical model (with the pan included in the domain) overestimated the heat flux to the calorimeter. Shown in Figure 27 are the steady state values at different angular positions from the numerical (pan included in the domain) and experimental results [38]. The steady state values confirm that the numerical model overestimated the heat flux to the calorimeter. Shown in Figure 27b are the numerical results from the model where the pan is excluded from the domain. In this case, the numerical model matched the experimental results everywhere except one data point at the top point on the center plane. Although that data point is not reported experimentally due to malfunctioned thermocouple, it is expected to follow the same trend as the top points on the left and right planes. Shown in Figure 28 is the heat flux distribution over the calorimeter from the numerical simulation: a) top, b) side and c) bottom. The heat flux to the calorimeter seems to be evenly distributed throughout the middle section of the calorimeter but slightly lower on the top side at the right and left planes.

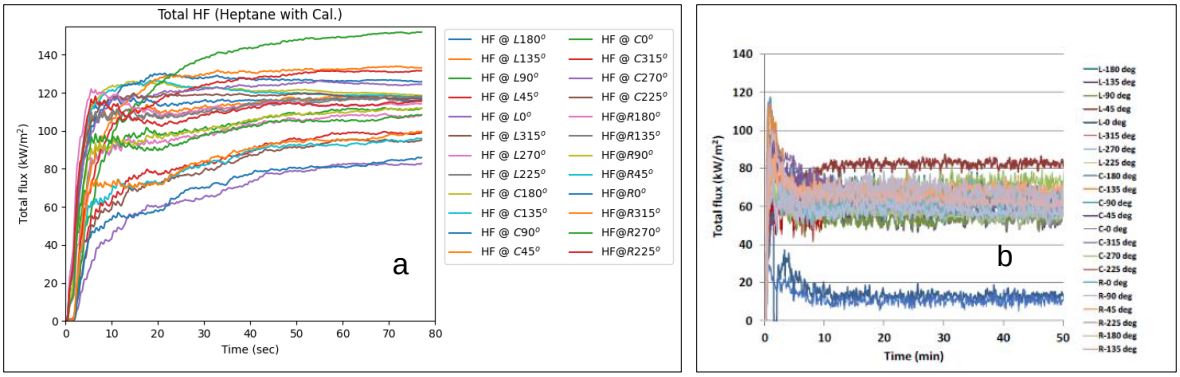

Figure 26. Total heat flux to calorimeter at different angular-positions: a) Numerical (with pan), b) Experimental.

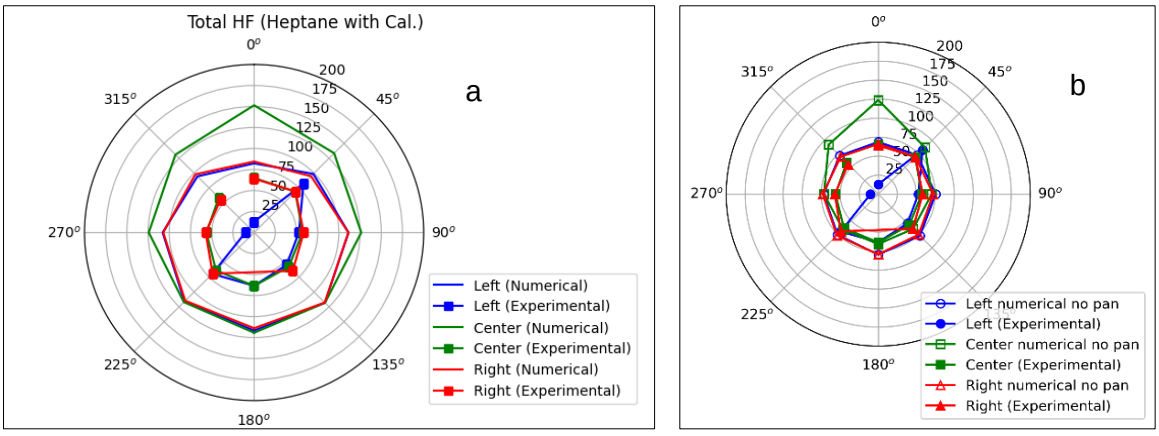

Figure 27. Spider plot of total heat flux (kW/m^2) to calorimeter at different angular-positions a) pan included in the numerical model, b) pan not included in the numerical model

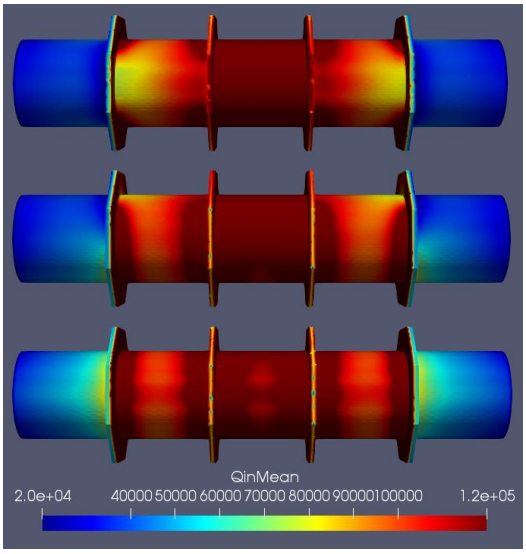

a) Top view

b) Side view

c) Bottom view

Figure 28. Heat flux (W/m^2) distribution (numerical): a) top view, b) side view, c) bottom view

5.1.6.2 FDS

The contours of incident heat flux to the calorimeter are shown in Figure 29. The maximum flux is 111 kW/m^2 at the bottom surface of the calorimeter. Lower fluxes can be seen on the sides.

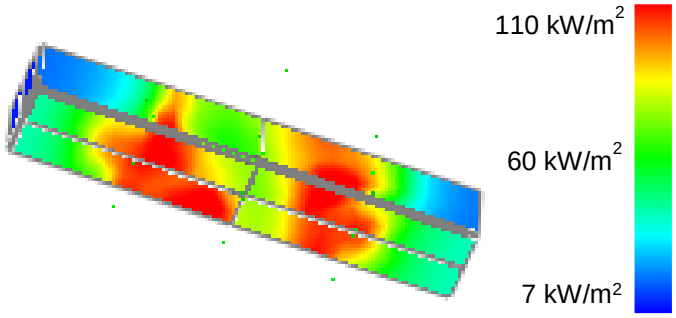

Figure 29. Incident heat flux on the calorimeter surface from heptane pool fire simulation

5.1.7 Calorimeter Temperature

5.1.7.1 OpenFOAM

Shown in Figure 30 are the transient calorimeter temperatures from a) the numerical simulation (pan included in the domain) and b) the experiment [2]. Shown in Figure 31 are the steady state values at different angular positions from the numerical (pan included) and experimental results [38]. Both figures (Figure 29a and Figure 30a) indicate that the numerical model, where the pan is included in the domain, overestimates the temperature distribution on the calorimeter. Figure 31b shows the results from the simulations where the pan is not included in the domain. Calorimeter temperature from this model is closer to the experimental results.

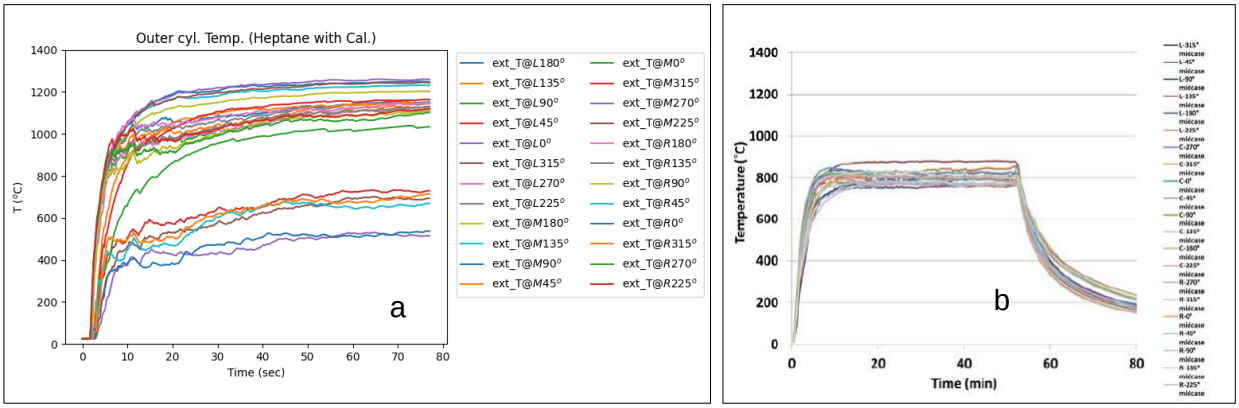

Figure 30. Outer cylinder temperatures at different angular-positions: a) Numerical (with pan), b) Experimental.

Shown in Figure 32 is the temperature distribution over the calorimeter from the numerical simulation: a) top, b) side and c) bottom. It is clear from this figure (Figure 32) and Figure 31 (both a and b) that the numerical model underestimated the temperature values on top of the calorimeter at the right and left planes of the calorimeter. The reason is attributed to the missing model for conduction heat transfer along the calorimeter surface. In the experiment, heat transfer by conduction through the outer steel cylinder is expected to heat up the thermocouples at these locations even if the gas phase temperature at these locations is not as high. This is why the experimental outercylinder temperatures are very close to each other. However, numerically, the calorimeter is an empty object with adiabatic boundary condition, therefore there is no thermal mass for the calorimeter and no heat transfer along the surface of the calorimeter.

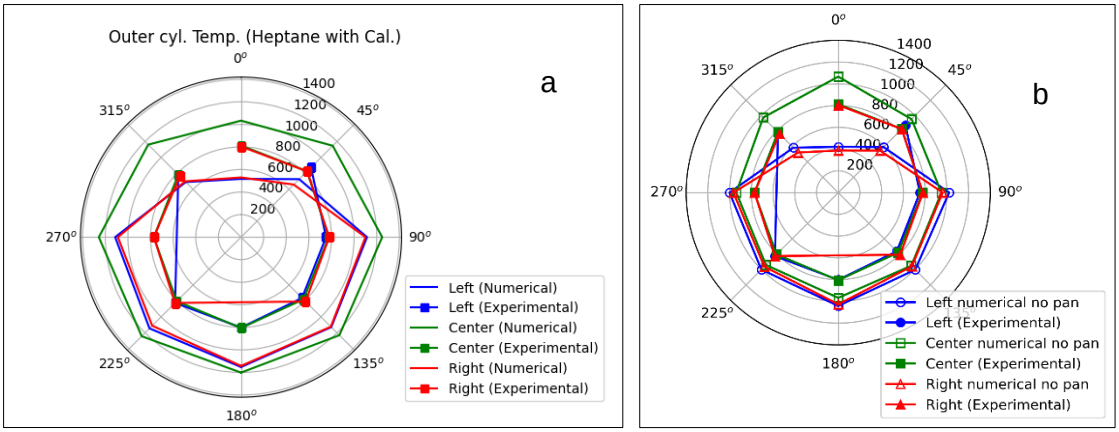

Figure 31. Spider plot of outer cylinder temperatures (°C) at different angular-positions a) pan included in the numerical model b) pan not included in the numerical model

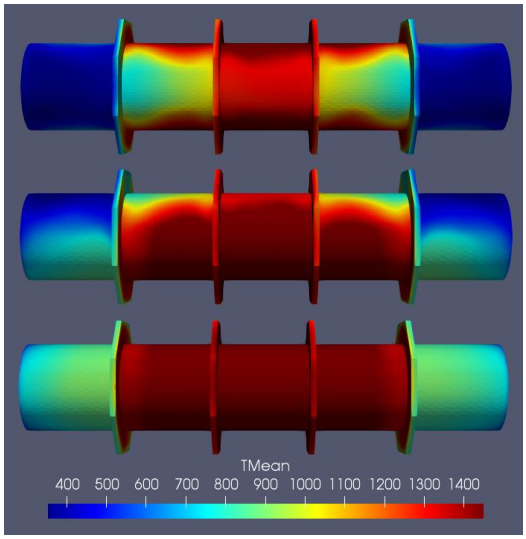

a) Top view

b) Side view

c) Bottom view

Figure 32. Calorimeter temperature distribution (K) (numerical): a) top view, b) side view, c) bottom view

After looking at all previous results in Sections 5.1.3, 5.1.4, 5.1.6 and 5.1.7 it is apparent that there are some discrepancies between the numerical and experimental results. A possible explanation has to do with a phenomena that was not considered in the numerical simulations, which is boiling and bubbling of heptane in the pan. Unlike the crude oils, heptane is transparent, which means that the radiation feedback to the heptane pool heats up not only the fuel surface but also the bottom of the heptane pool (i.e. the pan itself). While in the crude oil cases, the fuel is likely being heated from the top surface, given its black color and being mostly opaque. In case of heptane, that boiling and/or bubbling might have artificially lifted the surface of the heptane closer to the rim of the pan. That would explain why the numerical model results from the case where the pan is excluded from the domain showed better agreement with the experimental results. If the fuel top surface is closer to the rim it is approaching the scenario where there is no rim in the domain.

5.1.8 Heat Release Rate (HRR)

5.1.8.1 OpenFOAM

Shown in Figure 33a are the HRR, radiative heat release and heat release due to soot oxidation from the numerical simulation. Shown in Figure 33b is the experimental HRR [2]. HRR from the numerical model was 4.1 MW. Experimental HRR was approximately 4.4 MW.

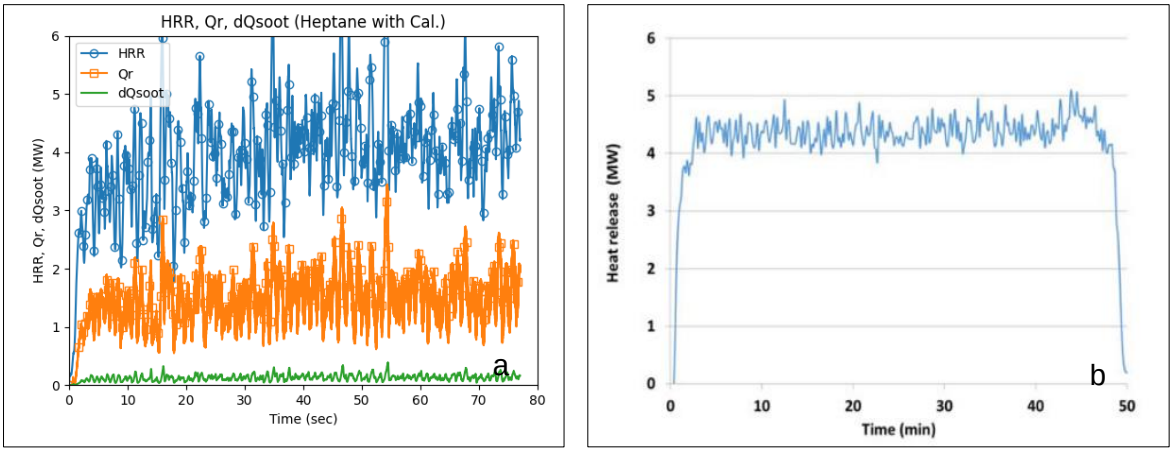

Figure 33. Time series results of heat release rate, radiative heat flux, soot radiative flux: a) Numerical, b) Experimental heat release rate.

5.1.8.2 FDS

The numerical HRR for the heptane pool fire with calorimeter is presented in Figure 34. The average HRR from the figure is 5.5 MW while the experimental value is 5.2 +/- 0.2 MW.

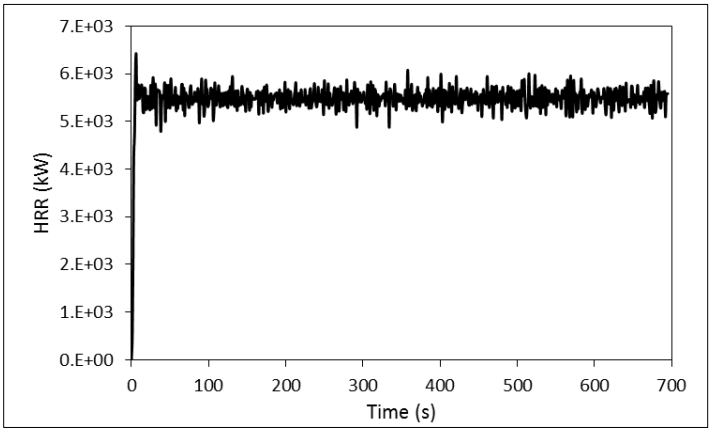

Figure 34. Numerical HRR for heptane with calorimeter simulation in FDS

5.1.9 Temperature Contours

5.1.9.1 OpenFOAM

Shown in Figure 35 are the temperature contours from a) the numerical simulation and b) the experiment [2]. Only the results from the model that includes the pan are reported. The effect of the calorimeter on temperature distribution is visible for both numerical and experimental results. Also there is good agreement between numerical and experimental temperature contour surrounding the calorimeter, ~1150 K. However, except for the 1150 K contour, the experimental contours are larger than that of the numerical contours as well as the expected temperatures measured by the thermocouples from the centerline thermocouple tree. For example, the height of the 950 K contour is ~ 3.8 m, while the height of same temperature from

the thermocouples tree is around 3 m. A possible reason for these differences between numerical results, experimental thermocouple tree measurements and the experimental contours is the way temperature contours are obtained experimentally; an infrared camera was used which might have been affected by the difference in emissivity (for example soot versus combustion products emissivity) from different flame areas.

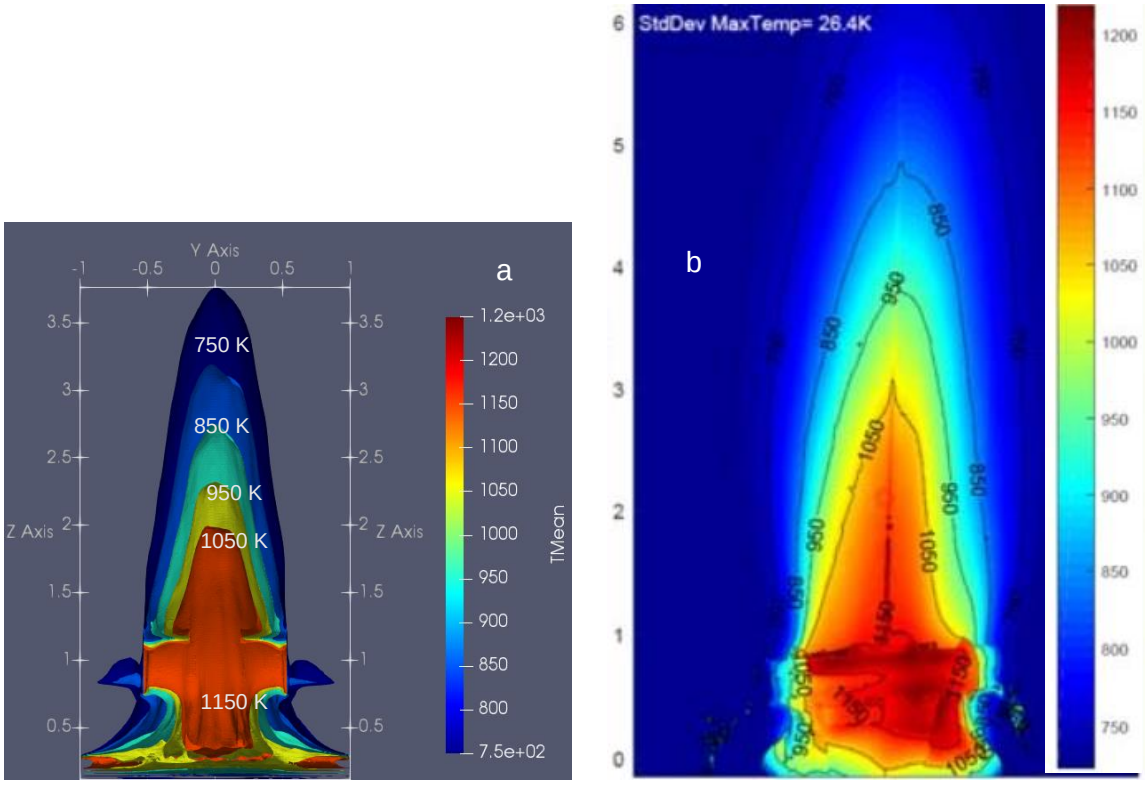

Figure 35. Temperature contours (Heptane with calorimeter). a) Numerical, b) Experimental

5.1.9.2 FDS

Figure 36 presents the temperature contours on the bottom of the calorimeter, which indicates higher temperature values compared to the top surface and the sides. The temperature range is 633-1073 °C.

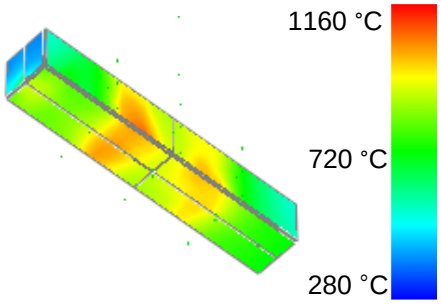

Figure 36. Temperature distribution on the bottom surface of the calorimeter from heptane pool fire simulation

5.1.10 Radiation Contours and Surface Emissive Power (SEP)

5.1.10.1 OpenFOAM

Shown in Figure 37a are the radiative heat flux contours from the numerical simulation (with pan in the domain). Shown in Figure 37b are the SEP contours from the experiment [2]. It is important to note that the radiative contours are not equivalent to the SEP contours; the radiative contours represent the radiation field iso-surfaces around the flame. The SEP is the projected radiation on a single point in the field of view of the IR camera, which is sensitive only to medium wave lengths of 3-5 micrometers, located at a distance from the flame. Nonetheless, both have the same values for qualitative comparison. The presence of the calorimeter seems to have distorted the numerical and experimental contours in the same manner.

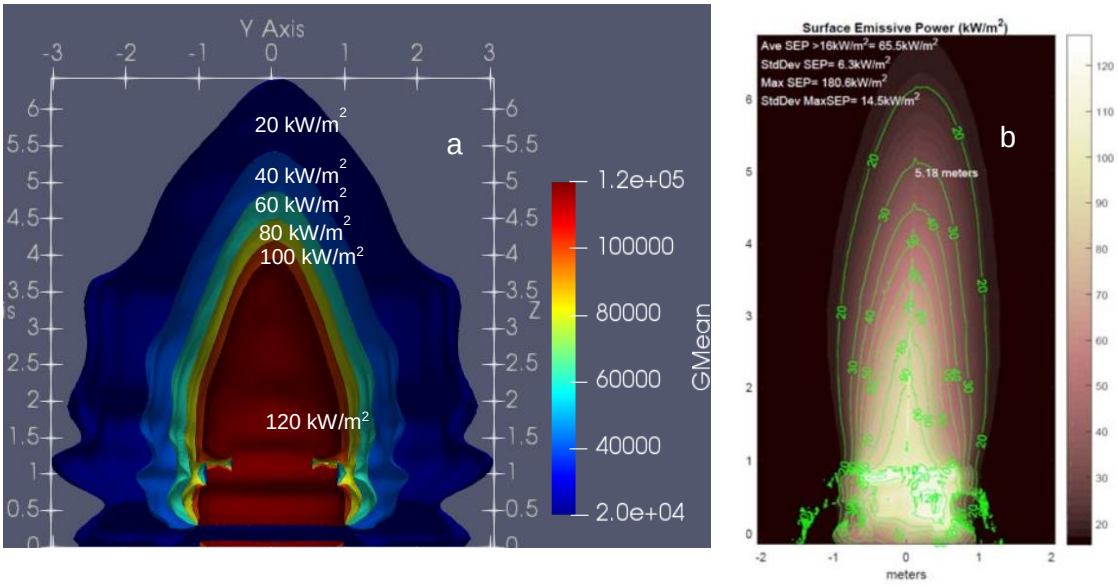

Figure 37. a) Radiation contours (Numerical) b) SEP (Experimental)

5.1.11 Wide Angle Heat Flux

5.1.11.1 OpenFOAM

Shown in Figure 38 are the transient wide angle heat fluxes from a) the numerical simulation (time-averaged), b) the experiment [2] and c) the numerical simulation (actual values). Shown in Figure 39 are the steady state values at different heights: a) heat flux versus height and b) height versus heat flux [38]. The numerical model overestimated the wide angle heat flux at all data points. The main reason for this overestimation is that different measurement distances were used in the experiments and numerical simulations. The intensity of heat flux decreases as the distance from the fire to the target increases (i.e. the decrease is proportional to the square root of the distance). The measurement distances for wide angle heat flux gauges were 9 m and 6 m for the experiments and the numerical simulations, respectively. It should be also noted that the different methods were used to calculate the heat flux (numerically) and measure the heat flux (experimentally); numerically, the wide angle heat flux is estimated by calculating the

incident heat flux at the boundaries of the domain (i.e. far from the flame at 6 m from the pool center). Experimentally, the wide angle heat flux is measured using a total heat flux gauge with a 180^o view angle, which might have different sensitivity to different wave lengths. In the numerical model, all wavelengths are considered using the WSGG radiation model. This behavior is consistently repeated for all simulations; the numerical model overestimated the wide angle heat flux compared to the experimental results.

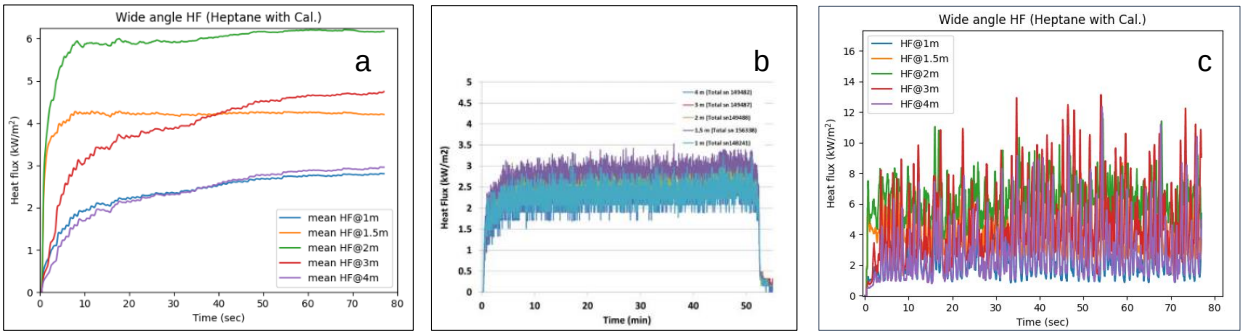

Figure 38. Wide angle heat fluxes of heptane with calorimeter: a) Numerical, time-averaged, b) Experimental, c) Numerical.

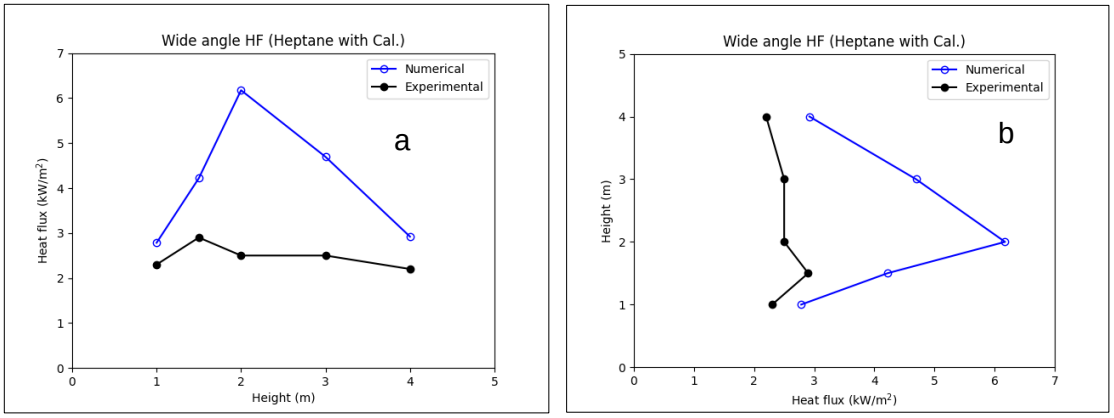

Figure 39. Average wide angle heat fluxes at different heights a) Flux vs. Height b) Height vs. Flux.

5.1.11.2 FDS

The wide angle radiometer readings from the experiments and simulations are compared in Figure 40. The simulation well-predicted the experimental results and the range of the readings is 2-3 kW/m^2. The average wide angle heat fluxes from the simulation and experiment are compared in Figure 41.

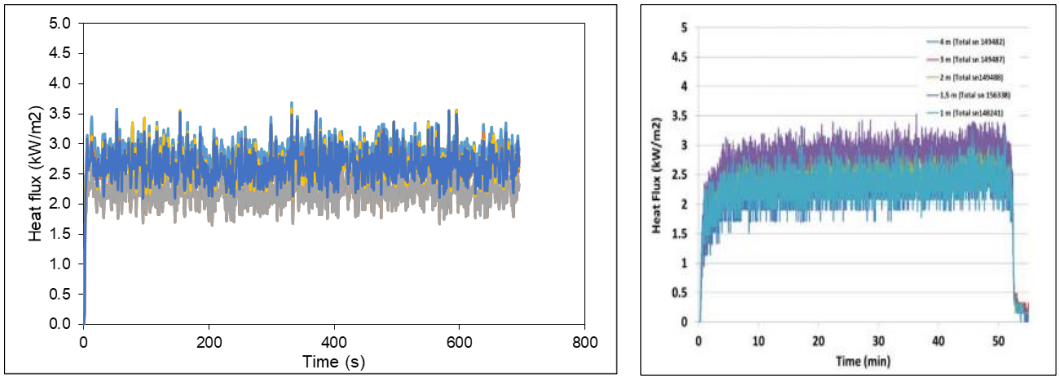

Figure 40. Wide angle radiometer readings for heptane pool fire with calorimeter from simulation (left panel) and experiment (right panel)

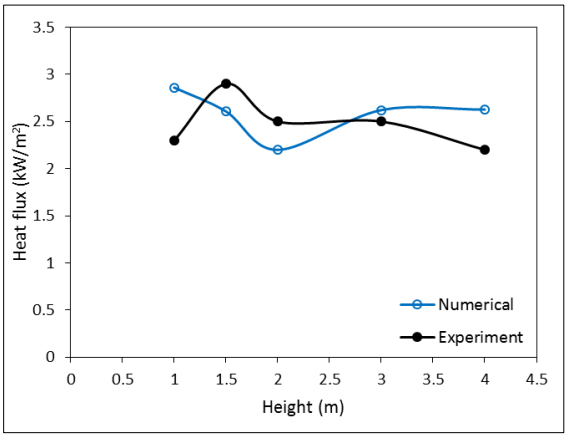

Figure 41. Average wide angle heat fluxes at different heights for heptane with calorimeter pool fire from FDS simulations

5.1.12 Narrow Angle Heat Flux

5.1.12.1 OpenFOAM

Shown in Figure 42 are the transient narrow angle heat fluxes from a) the numerical simulation (time-averaged), b) the experiment [2] and c) the numerical simulation (actual values). Shown in Figure 43 are the steady state values at different heights: a) heat flux versus height and b) height versus heat flux [38]. Both numerical and experimental results have similar profiles; near constant heat flux up to ~1.5 – 2 m, then a decreasing heat flux trend up to 4 m. However, the numerical model seems to be shifted upwards, overestimating the narrow angle heat flux values at all data points. The reason for that is the different methods used to calculate the heat flux (numerically) and measure the heat flux (experimentally); numerically, the narrow angle heat flux is estimated by sampling the radiation field close to the flame (i.e. at a distance 1.1 m from the pool center). In the numerical model, all wavelengths are considered using the WSGG radiation model. Experimentally, a 5.5^{o} view angle radiometer with a zinc selenide window was used. The zinc selenide window has 70% transmissivity in the wavelength range 2-20 μm and zero transmissivity outside this range. That explains the lower narrow angle heat fluxes from the

experimental results. It should be also noted that the surface emissive power measured by the IR camera was about 10% higher than the narrow angle radiometers.

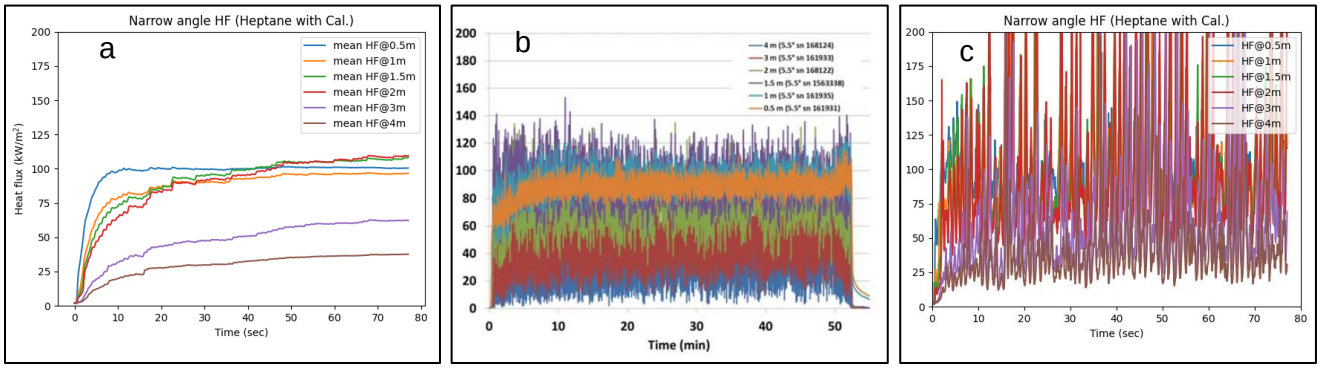

Figure 42. Narrow angle heat fluxes of heptane with calorimeter: a) Numerical, time-averaged, b) Experimental, c) Numerical.

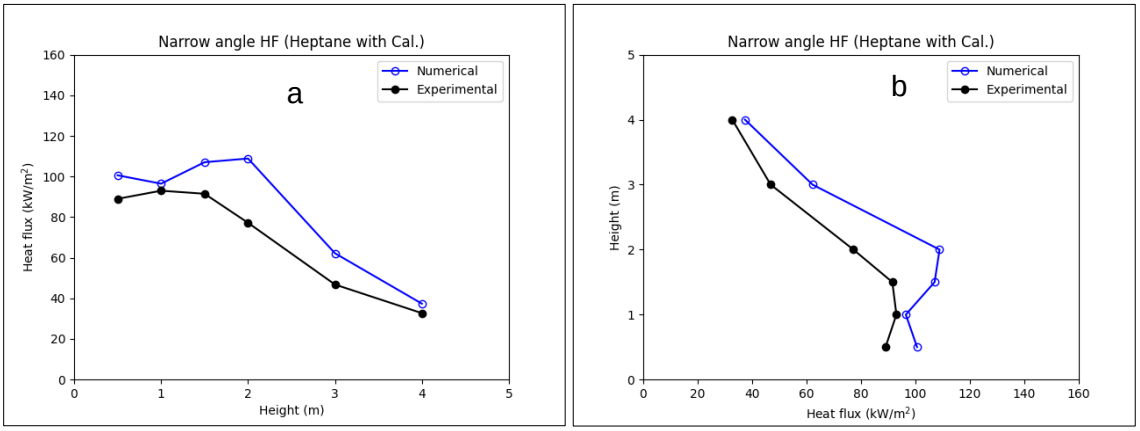

Figure 43. Average narrow angle heat fluxes at different heights a) Flux vs. Height b) Height vs. Flux.

5.1.13 **Flame Height**

5.1.13.1 OpenFOAM

Shown in Figure 44 is the flame height from a) the numerical simulation and b) the experiment [2]. Results from the two (2) numerical simulations correspond to the model where the pan is included in the domain (blue line) and the model where the pan is not in the domain (black line). Both models underestimated the flame height in this simulation as well as all other simulations. The reason is the different criteria used to define the flame height; numerically the flame height is defined by the highest point, in the domain, at which there is a nonzero value of the fuel concentration. Experimentally, the flame height is obtained using an IR camera which might have been affected by the radiation from soot particles at an elevated temperature. Given the fact that soot and high temperatures would coincide downstream from the fuel, it's expected that the numerical flame height is always lower than the flame height measured experimentally.

Another criterion for defining flame heights from fluctuating turbulent diffusion flames is the height of 50% intermittency of a visible flame. [39], [40]

On a different note, having the pan in the domain resulted in a shorter flame height (numerically). The presence of a pan creates a recirculation zone by the pan wall. This recirculation zone causes some of the flow to be attached to the pan wall resulting in a shorter flame.

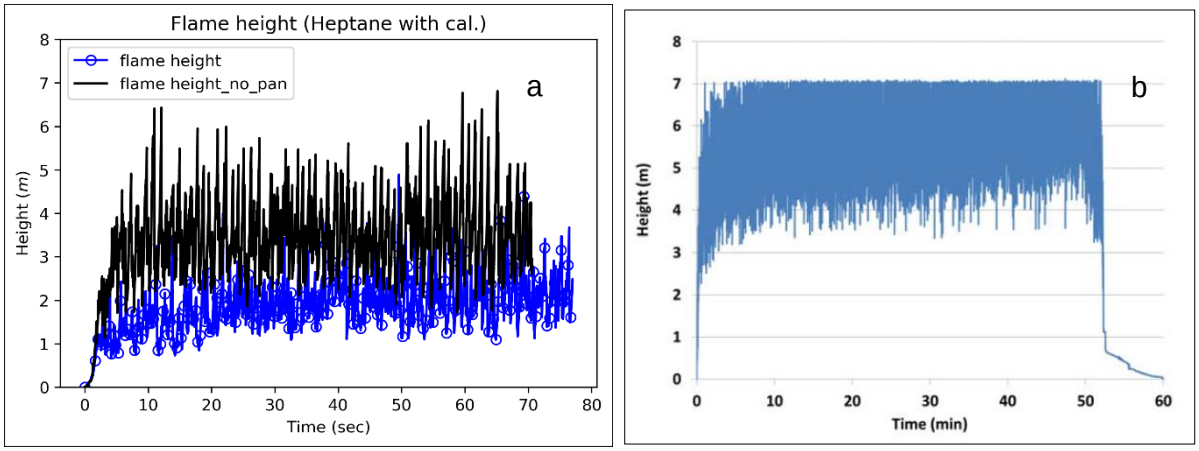

Figure 44. Flame height of heptane with calorimeter: a) Numerical, b) Experimental.

5.2 Heptane without Calorimeter

5.2.1 OpenFOAM Results Summary

Discussed in this section are the validation results for the “heptane without calorimeter” case. Numerical results are compared to experimental results from the NRC experiment at Sandia National Lab (Test 1.2) [2], [38]. Summaries of the numerical and experimental ranges are shown in Table 15.

Table 15. Results summary for the heptane without calorimeter simulation from OpenFOAM

Section	Validation parameter	Numerical range	Experimental range	Comments
5.2.3	Centerline temperature	309-931 °C with pan / 568-959 °C without pan	602 – 895 °C	Good agreement given absence of a boiling model
5.2.4	Radiative fraction	38 %	34 %	Good agreement
5.2.5	HRR	5.12 MW	5.2 MW	Good agreement
5.2.4	Soot yield	7.7%	Not reported	
5.2.6	Temperature contours	750 – 1150 K	750 – 1150 K	
5.2.8	Wide angle HF	3.3 – 5.2 kW/m^2	2.5 – 3.1 kW/m^2	Overestimated
5.2.9	Narrow angle HF	55 – 123 kW/m^2	61 – 95 kW/m^2	Overestimated
5.2.10	Flame height	2.8 m (with pan) 4.2 m (no pan)	6.8 m	Different criteria

5.2.2 FDS Results Summary

The FDS results from simulating the heptane without calorimeter case are summarized in **Error! Not a valid bookmark self-reference.**. Further discussion about each parameter is provided in the following subsections.

Table 16. Results summary for the heptane without calorimeter simulation from FDS

Section	Validation parameter	Numerical range	Experimental range	comments
5.2.3	Centerline temperature	440–800 °C	602–895 °C	Good agreement given absence of a boiling model
5.2.4	Radiative fraction	38 %	34 %	Good agreement
5.2.5	HRR	5.9 MW	5.2 MW	Slightly overpredicted
5.2.6	Temperature contours	374–1200 °C	750–1150 K	
5.2.8	Wide angle HF	1.5–3 kW/m^2	2–3.1 kW/m^2	Good agreement
NA	Flame height	6 m	6.8 m	Both are visually measured

5.2.3 Plume Centerline Temperature

5.2.3.1 OpenFOAM

Shown in Figure 45 are the transient centerline temperatures from a) the numerical simulations and b) the experiment [2]. Shown in Figure 46 are the steady state centerline temperatures: a) temperature versus height and b) height versus temperature [38]. The blue curve is the result from the model with pan in the domain. The green line is the result from the model without the pan.

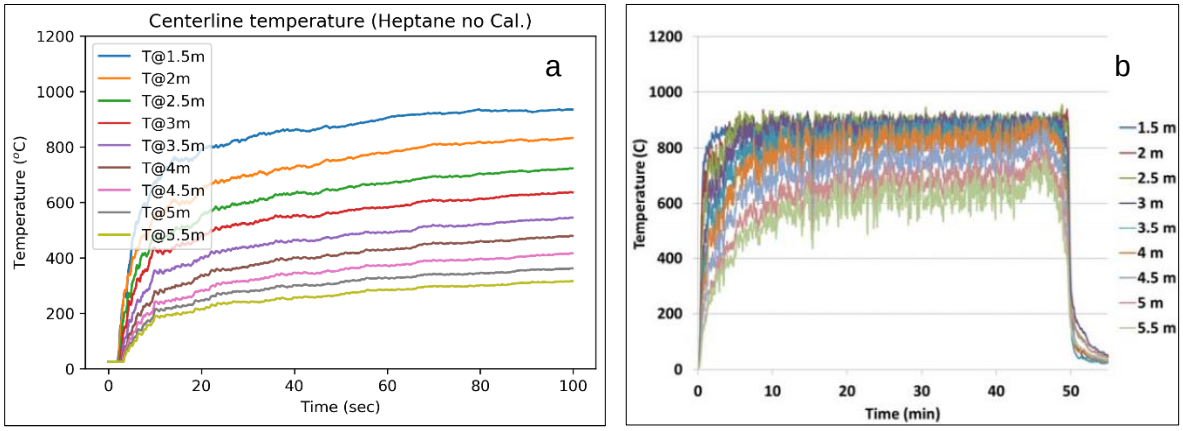

Figure 45. Center line temperature at different heights (heptane without calorimeter): a) Numerical, b) Experimental

Although the experiment did include a pan that is placed on top of the steel floor (i.e. pan rim not flush with the steel floor), the numerical model without the pan better matched the experimental results. The numerical model with the pan didn't match the overall trend and underestimated the centerline temperature. A possible explanation was discussed in section 5.1.7 but repeated here

for completeness; the boiling / bubbling phenomena hasn't been considered in the numerical model. Boiling / bubbling might have, artificially, lifted the surface of the heptane closer to the rim of the pan, making the results from the model where the pan is not included closer to the experimental results.

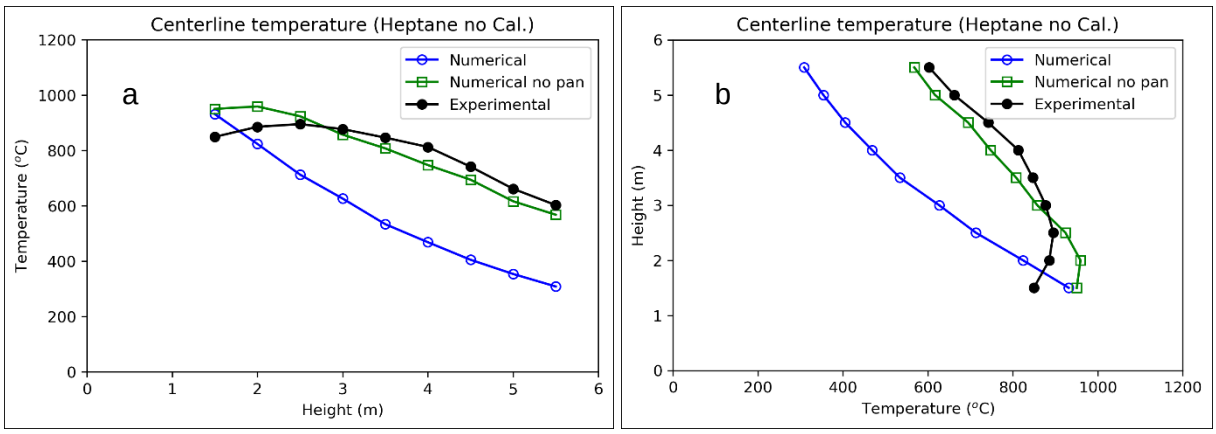

Figure 46. Average centerline temperatures at different heights a) Temp. vs. Height b) Height vs. Temperature

5.2.3.2 FDS

The results from simulating the heptane pool fire without the calorimeter are compared against the experimental results from Test 1.1. The experimental and numerical centerline temperatures are compared in Figure 47. Simulations underpredicted the experimental results. The range of temperatures in the simulations is 440-800 °C, while the experimental range is 602-895 °C.

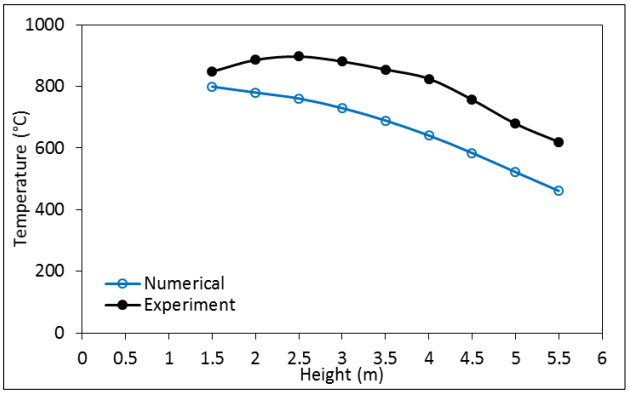

Figure 47. Average flame temperature at the centerline of the pool for heptane pool fire without the calorimeter

5.2.4 Radiative Fraction & Soot Yield

5.2.4.1 OpenFOAM

Shown in Figure 48 is the radiative heat fraction and the soot yield from the numerical simulation. There is good agreement between numerical and experimental results in terms of radiative fraction: the average radiative fraction from the numerical simulation was ~38% while average radiative fraction from the experiments was 34~39% (refer to Figure 24b). Average soot yield from numerical simulation was 7.7%. No soot yield was measured during the experiment.

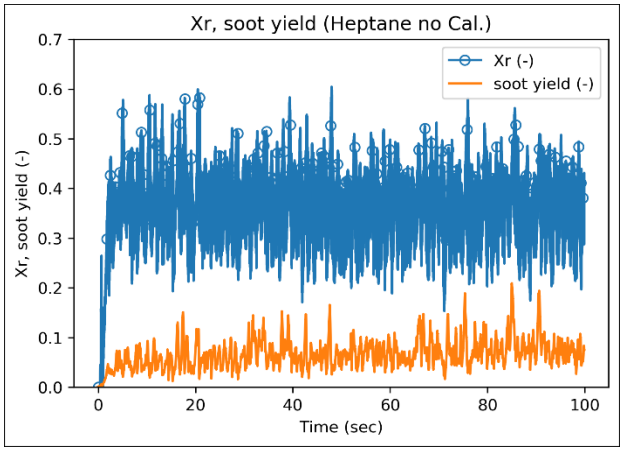

Figure 48. Numerical radiative fraction and soot yield results.

5.2.4.2 FDS

The numerical radiative fraction from FDS simulations for the heptane without calorimeter case is shown in Figure 49. The average X_r is 37.7%, which is in reasonable agreement with the experimental value (34%).

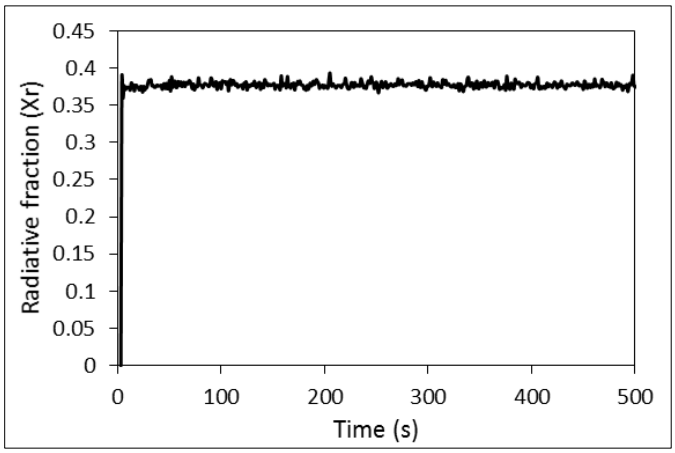

Figure 49. Numerical radiative fraction from FDS

5.2.5 Heat Release Rate (HRR)

5.2.5.1 OpenFOAM

Shown in Figure 50a are the HRR, radiative heat release and heat release due to soot oxidation from the numerical simulation. Shown in Figure 50b is the experimental HRR [2]. HRR from the numerical model was ~ 5.12 MW. HRR from the experiment was ~ 5. 2 MW.

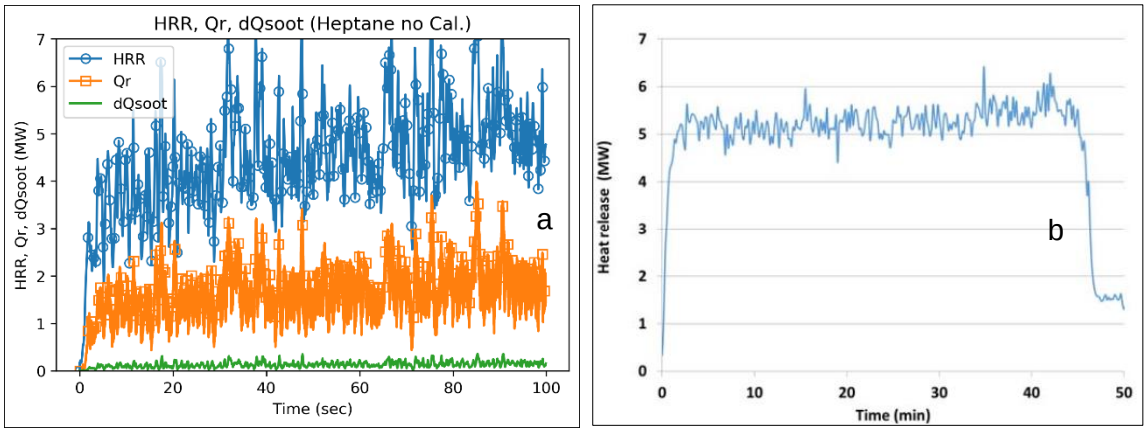

Figure 50. Time series results of heat release rate, radiative heat flux, soot radiative flux: a) Numerical, b) Experimental heat release rate

5.2.5.2 FDS

The numerical HRR for the heptane pool fire without calorimeter is presented in Figure 51. The average HRR from the figure is 5.9 MW while the experimental value is 5.6 +/- 0.2 MW.

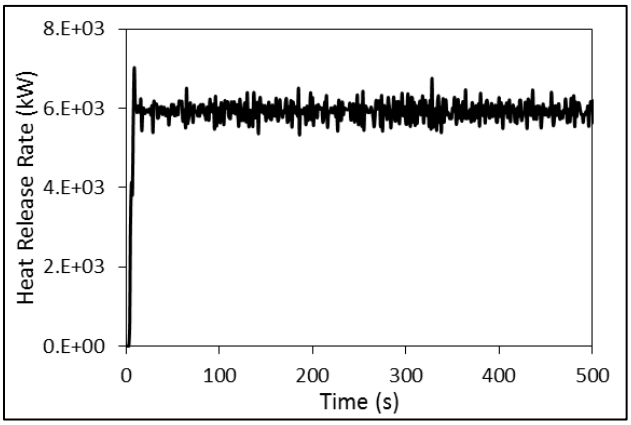

Figure 51. Numerical HRR for heptane without calorimeter pool fire from FDS

5.2.6 Temperature Contours

5.2.6.1 OpenFOAM

Shown in Figure 52a are the temperature contours from the numerical simulation. Shown in Figure 52b is a time-averaged image of the flame from the experiment [2]. Qualitatively, temperature contours and the flame image have the same shape. The effect of having the calorimeter in the domain, on the temperature contours, can be inferred by comparing Figure

52a with Figure 35a: The contours in Figure 35 are distorted around the calorimeter following the cylindrical shape of the calorimeter.

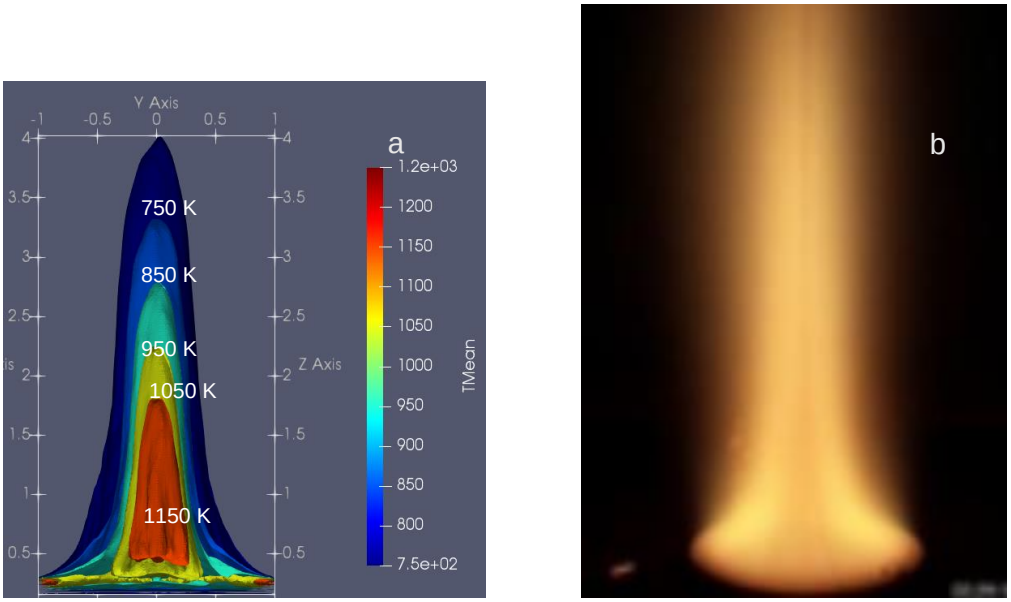

Figure 52. a) Numerical temperature contours b) Time-averaged image of the flame (experimental)

5.2.6.2 FDS

Shown in Figure 53 are the temperature contour on a “slice” at the center of the domain. The temperature values within the flame zone ranges from 374 °C to 1200 °C.

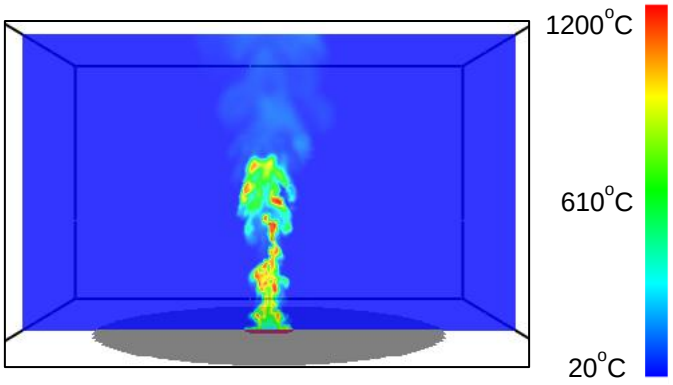

Figure 53. Temperature slice across the central plane of the flame in the simulations of heptane pool fire without calorimeter

5.2.7 Radiation Contours and SEP

5.2.7.1 OpenFOAM

Shown in Figure 54 are the radiative heat flux contours from the numerical simulation. Although no SEP was reported, experimentally, it is important to note that the radiation contours from the simulations are not equivalent to SEP. The radiative heat flux contours represent the radiation

field iso-surfaces around the flame. The SEP is the projected radiation on an IR camera. See Section 5.1.10 for more details.

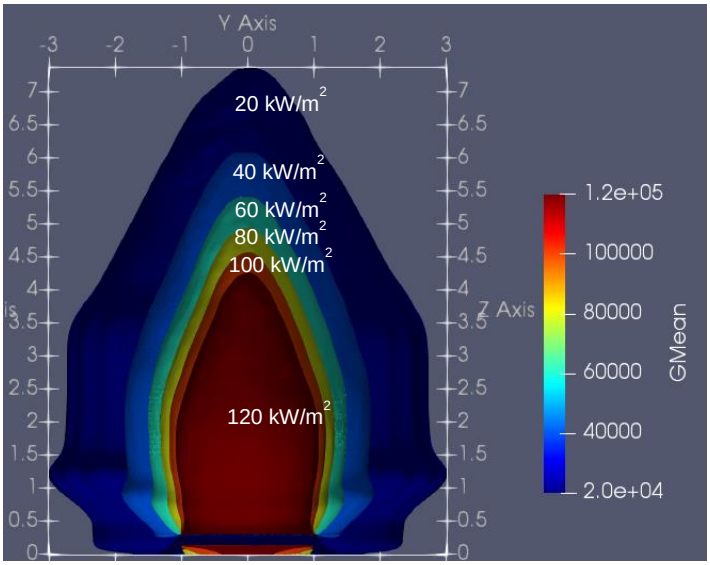

Figure 54. Radiative heat flux contours (numerical)

5.2.8 Wide Angle Heat Flux

5.2.8.1 OpenFOAM

Shown in Figure 55 are the transient wide angle heat fluxes from a) the numerical simulation (time-averaged), b) the experiment [2] and c) the numerical simulation (actual values). Shown in Figure 56 are the steady state values at different heights: a) heat flux versus height and b) height versus heat flux [38]. Similar to the previous simulation, the numerical model overestimated the wide angle heat flux at all data points. The reason is repeated here for completeness; the main reason for this overestimation is that the different measurement distances were used in the experiments and numerical simulations. The intensity of heat flux decreases as the distance from the fire to the target increases (i.e. decrease proportional to square root of the distance). The measurement distances for wide angle heat flux gauges were 9 m and 6 m for the experiments and the numerical simulations, respectively. Also, it should be noted that, numerically, the wide angle heat flux is estimated by calculating the incident heat flux at the boundaries of the domain (i.e. far from the flame). Experimentally, the wide angle heat flux is measured using a total heat flux gauge with a 180^{o} view angle, which might have different sensitivity to different wave lengths. In the numerical model, all wavelengths are considered using the WSGG radiation model.

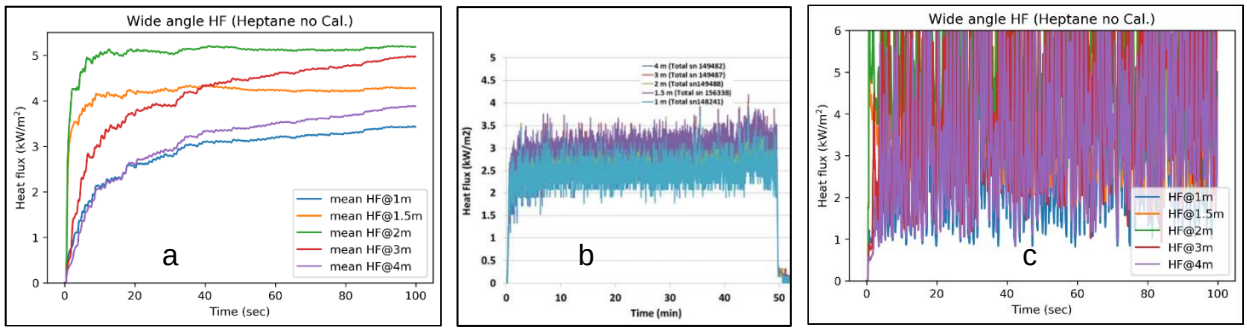

Figure 55. Wide angle heat fluxes of heptane without calorimeter: a) Numerical, time-averaged, b) Experimental, c) Numerical.

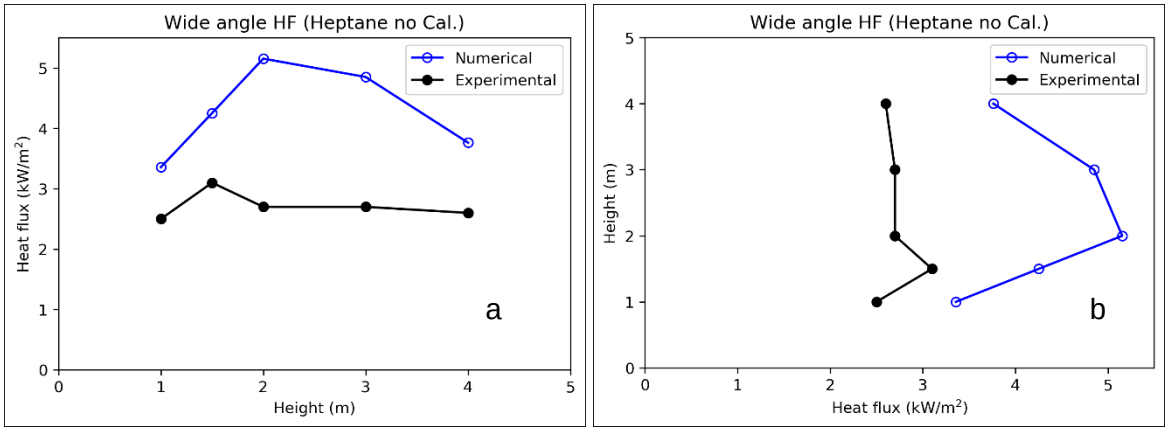

Figure 56. Average wide angle heat fluxes at different heights a) Flux vs. Height b) Height vs. Flux.

5.2.8.2 FDS

The wide angle radiometer readings from the experiments and simulations for heptane pool fire without calorimeter are compared in Figure 57. The simulation well-predicted the experimental results and the range of the readings is 1.5-3 kW/m^2. The average wide angle heat fluxes from the simulation and experiment are compared in Figure 58.

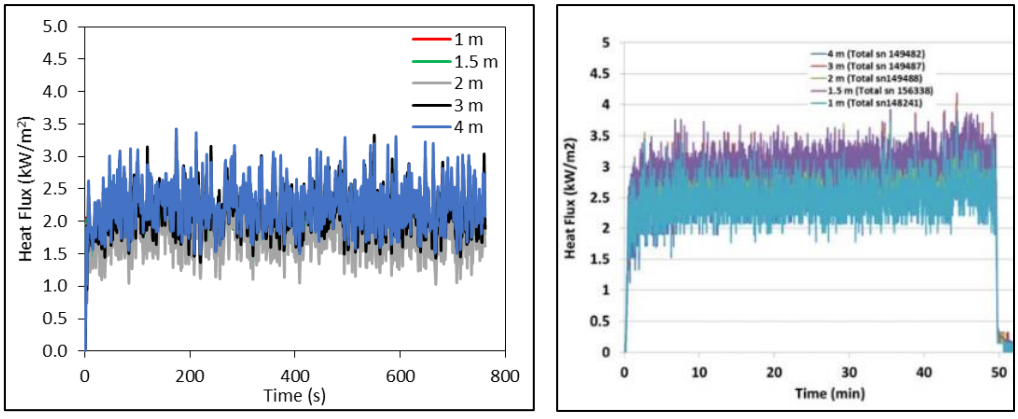

Figure 57. Wide angle radiometer readings for heptane pool fire without calorimeter from simulation (left panel) and experiment (right panel)

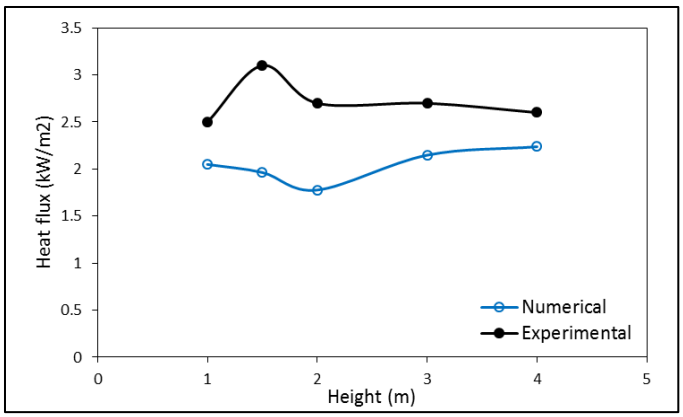

Figure 58. Average wide angle heat fluxes at different heights for heptane without calorimeter pool fire from FDS simulations

5.2.9 Narrow Angle Heat Flux

5.2.9.1 OpenFOAM

Shown in Figure 59 are the transient narrow angle heat fluxes from a) the numerical simulation (time-averaged), b) the experiment [2] and c) the numerical simulation (actual values). Shown in Figure 60 are the steady state values at different heights: a) heat flux versus height and b) height versus heat flux [38]. Figure 59 indicates that there is a general agreement between numerical and experimental results in terms of range, however, the steady state results in Figure 60 indicate a mismatch in trend and values. The numerical model overestimated the heat flux in the middle section while matched the experimental results otherwise. This behavior is not consistent with all other simulations results and needs further investigation to explain.

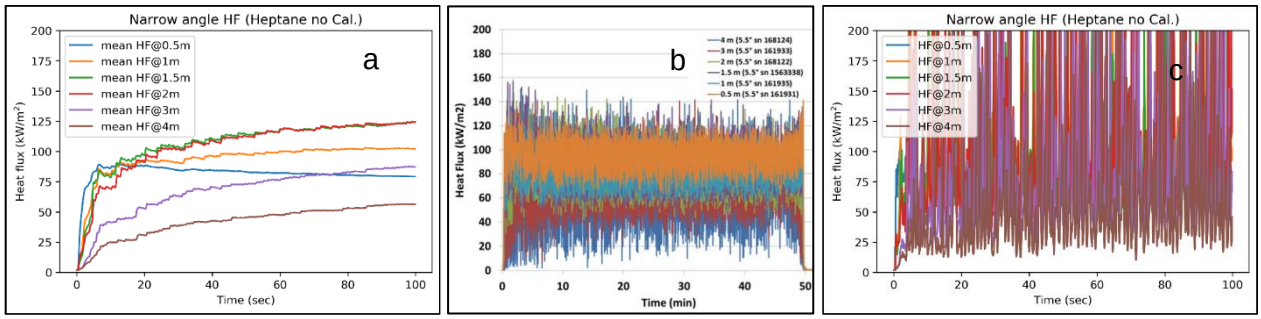

Figure 59. Narrow angle heat fluxes of heptane without calorimeter: a) Numerical, time-averaged, b) Experimental, c) Numerical.

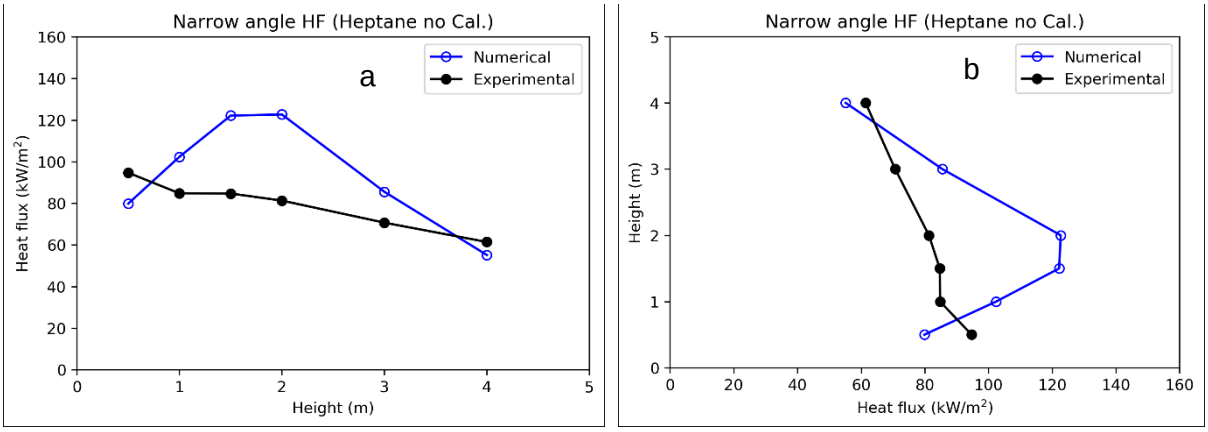

Figure 60. Average narrow angle heat fluxes at different heights a) Flux vs. Height b) Height vs. Flux.

5.2.10 **Flame Height**

5.2.10.1 OpenFOAM

Shown in Figure 61 is the flame height from the numerical simulation. Experimentally, the flame height was obtained from an averaged image of video clips. In Figure 61, the blue line is the result from the model that included the pan, while the black line is the result from the model that did not include the pan. Both numerical models underestimated the flame height (see Table 15). The reason is the different criteria used to define the flame height; numerically the flame height is defined by the highest point, in the domain, at which there is a nonzero value of the fuel concentration. Experimentally, in this test, the flame height is obtained using an averaged image of a video clip, which in reality is an averaged image of the glowing soot. Given the fact that glowing soot at high temperatures would exist downstream from the fuel, it's expected that the numerical flame height is always lower than the flame height measured experimentally. Similar to the previous case, having the pan in the domain resulted in a shorter flame height (numerically).

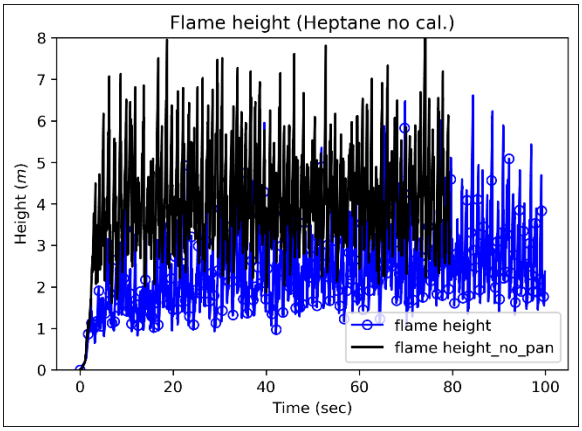

Figure 61. Flame height of heptane without calorimeter.

5.3 Bakken with Calorimeter

5.3.1 OpenFOAM Results Summary

Discussed in this section are the validation results for the “Bakken with calorimeter” case. Numerical results are compared to experimental results from the NRC experiment at Sandia National Laboratories (Test 2.5) [2], [38]. Summary of the numerical and experimental ranges are shown in Table 17.

Table 17. Results summary for the Bakken with calorimeter simulation from OpenFOAM

Section	Validation parameter	Numerical range	Experimental range	Comments
5.3.3	Centerline temperature	233 – 972 °C	236 – 978 °C	Good agreement
5.3.4	Exterior to calorimeter temperature	555 – 1135 °C	790 - 1070 °C	Good agreement given absence of calorimeter conductivity in the numerical model
5.3.5	Radiative fraction	44%	47 %	Good agreement
5.3.6	Heat flux to calorimeter	76 – 178 kW/m^2	64 – 136 kW/m^2	Good agreement
5.3.7	Calorimeter temperature	479 – 1196 °C	796 – 1031 °C	Good agreement given absence of calorimeter conductivity in the numerical model
5.3.8	HRR	3.77 MW	3.6 MW	Good agreement
5.3.5	Soot yield	15%	Not reported	
5.3.9	Temperature contours	750 – 1150 K	750 – 1150 K	
5.3.11	Wide angle HF	2.6 – 6.5 kW/m^2	1.9 – 2.4 kW/m^2	Overestimated
5.3.12	Narrow angle HF	30 – 143 kW/m^2	15.2 – 90 kW/m^2	Overestimated
5.3.13	Flame height	1.6 m	4.46 m	Different criteria

5.3.2 FDS Results Summary

The FDS results from simulating the Bakken with calorimeter case are summarized in Table 18. Further discussion about each parameter is provided in the following subsections.

Table 18. Results summary for Bakken with calorimeter simulation from FDS

Section	Validation parameter	Numerical range	Experimental range	Comments
5.3.3	Centerline temperature	331– 866 °C	236 – 978 °C	Reasonable agreement
5.3.4	Exterior to calorimeter temperature	113 – 900 °C	790 - 1070 °C	Underpredicted
5.3.5	Radiative fraction	39 %	47 %	Good agreement
5.3.6	Heat flux to calorimeter	11.2-111 kW/m2	64 – 136 kW/m2	
5.3.7	Calorimeter temperature	362 – 1161 °C	796 – 1031 °C	Slightly underpredicted
5.3.8	HRR	3.95 MW	3.8 MW	Good agreement
5.3.11	Wide angle HF	1.5-2.5 kW/m2	1.9 – 2.4 kW/m2	Good estimate
NA	Flame height	4.8 m	4.3 m	Different criteria

5.3.3 Plume Centerline Temperature

5.3.3.1 OpenFOAM

Shown in Figure 62 are the transient centerline temperatures from (a) the numerical simulations and (b) the experiments [2]. Shown in Figure 63 are the steady state centerline temperatures: a) temperature versus height and b) height versus temperature [38]. There is good agreement between the numerical and experimental results in terms of trend, range and values at each data point.

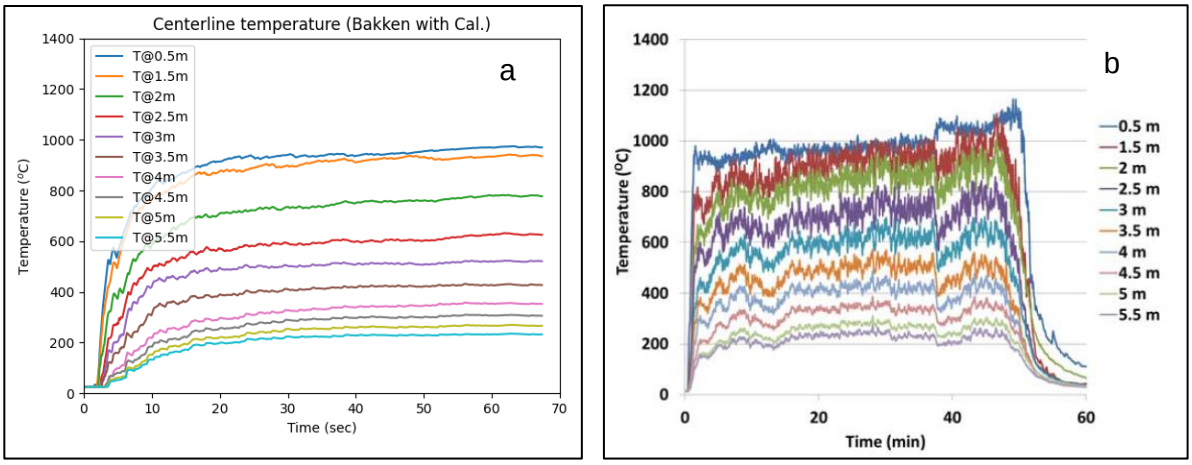

Figure 62. Centerline temperatures at different heights (Bakken with calorimeter): a) Numerical, b) Experimental.

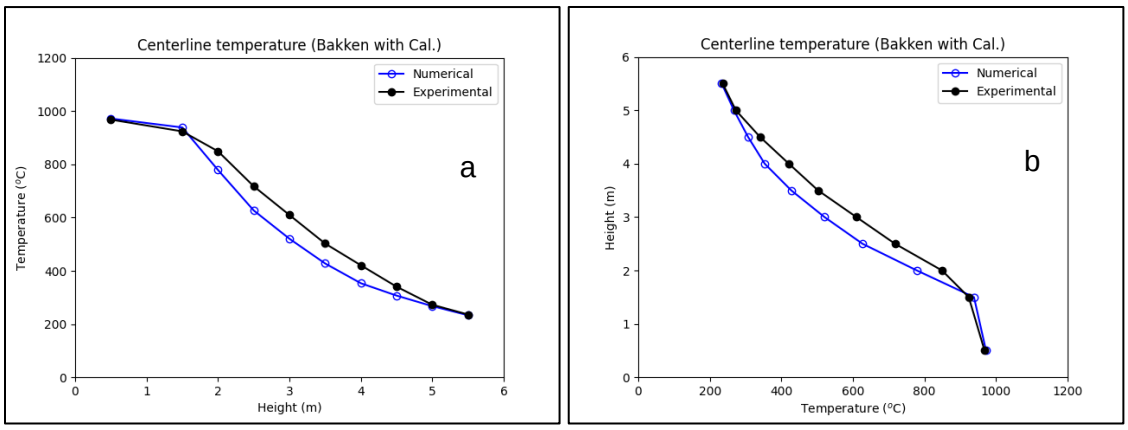

Figure 63. Average centerline temperatures at different heights a) Temp. vs. Height b) Height vs. Temp.

5.3.3.2 FDS

The results from simulating the Bakken pool fire with the calorimeter in the domain are compared against the experimental results from Test 2.5. Compared in Figure 64 are the experimental and numerical temperatures at the centerline of the flame. The range of temperatures from the simulations is 331-866 °C, while the experimental range is 236-978 °C. There is good agreement between the two sets.

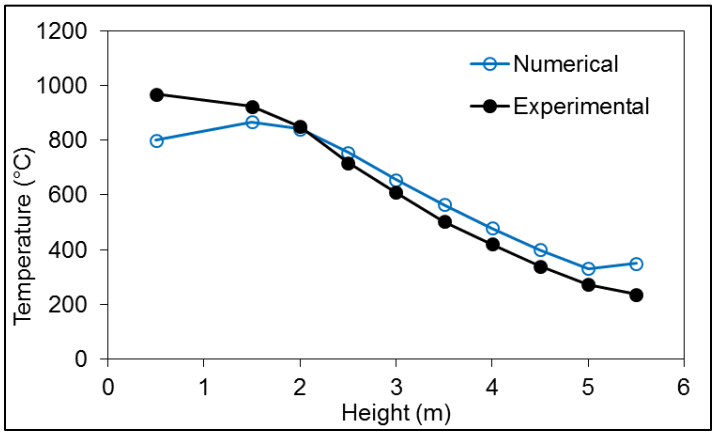

Figure 64. Average flame temperature at the centerline of the pool for Bakken pool fire with the calorimeter from the experiments (black line) and simulations (blue line)

5.3.4 Exterior to Calorimeter Temperature

5.3.4.1 OpenFOAM

Shown in Figure 65 are the exterior to calorimeter temperatures from a) the numerical simulation and b) the experiment [2]. Shown in Figure 66 are the steady state values at different angles: numerical and experimental [38].

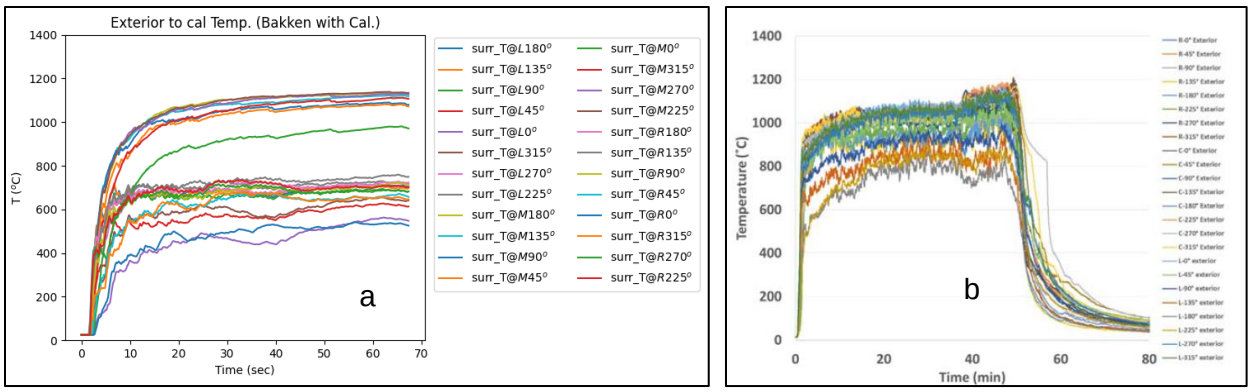

Figure 65. Exterior to calorimeter temperatures at different angular-positions: a) Numerical, b) Experimental

There is good agreement between numerical and experimental results on the center cross section. However, the numerical results underestimated the surrounding temperature on the left and right cross sections. A possible reason for this discrepancy is that, in the experimental setup, the surrounding thermocouples are attached to the calorimeter through steel rods. This would result in heating the thermocouple by conduction from the calorimeter to the thermocouples. Both numerical and experimental results indicate that the surrounding temperature is higher under the calorimeter than the temperature above the calorimeter.

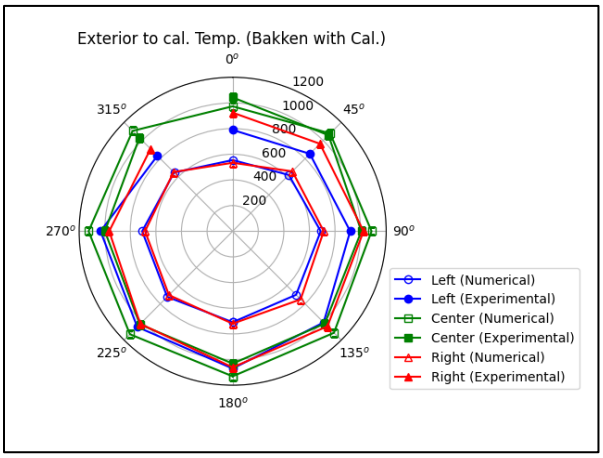

Figure 66. Spider plot of Exterior to calorimeter temperatures (°C) at different angular-positions.

5.3.4.2 FDS

The temperatures surrounding the calorimeter are shown in Figure 67. Two numerical plots are presented; raw data and time-averaged data. The experimental range is 796-1031 °C while the numerical range is 113-900 °C. Similar to the heptane with calorimeter simulations, the lower numerical temperatures are measured at the right and left planes. The spider plot comparing the average temperatures surrounding the calorimeter at different angles and planes from the simulation and experiment is shown in Figure 68. The numerical temperatures at the left and right planes are greatly lower than the experimental one. The simulated temperatures at the central plane are in reasonable agreement with the experimental temperatures, except for the

temperature above the calorimeter. Such trend is again attributed to; (1) the squared cross section of the calorimeter in the model (2) the absence of baffles in the simulations, (3) in the experiment, the surrounding thermocouples are attached to the calorimeter through a steel rod.

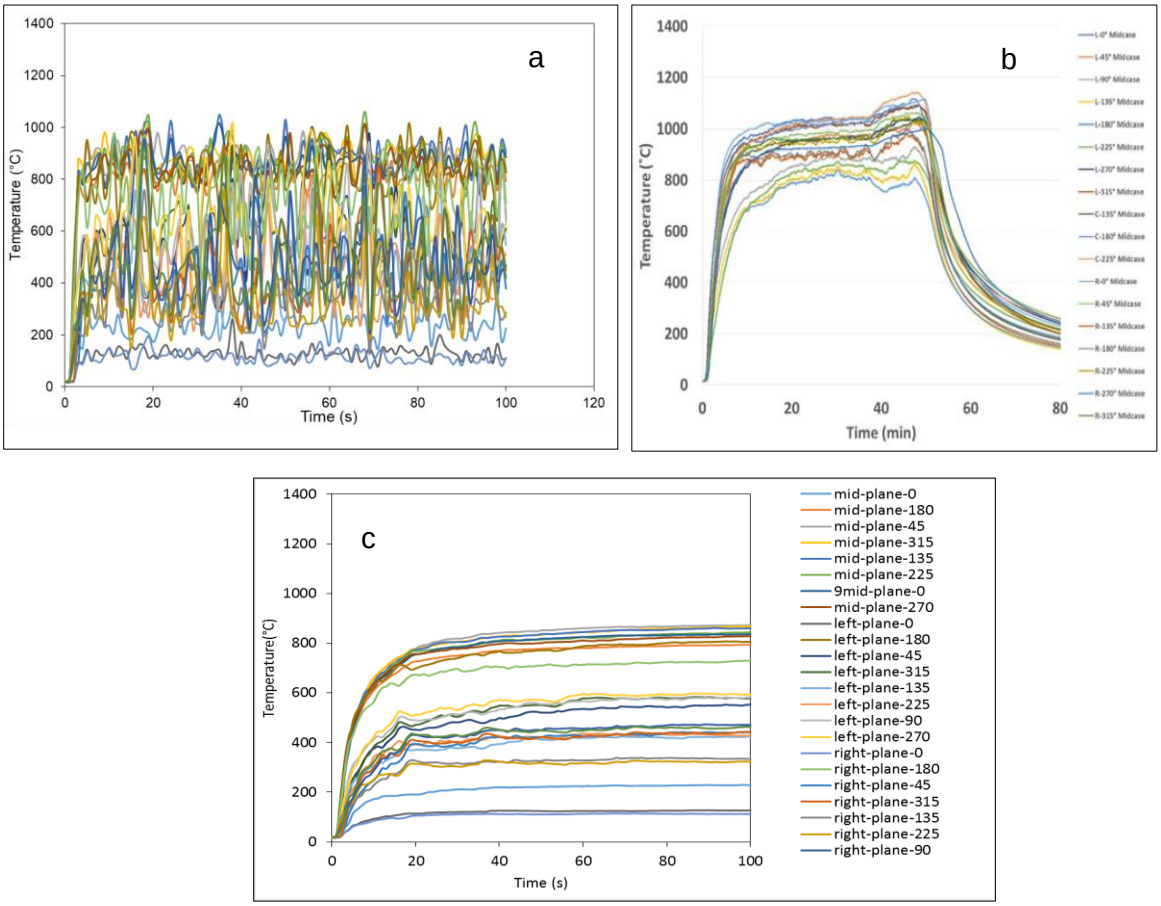

Figure 67. Temperatures surrounding the calorimeter from Bakken pool fire from a) simulations, b) experimental and c) time-averaged (numerical)

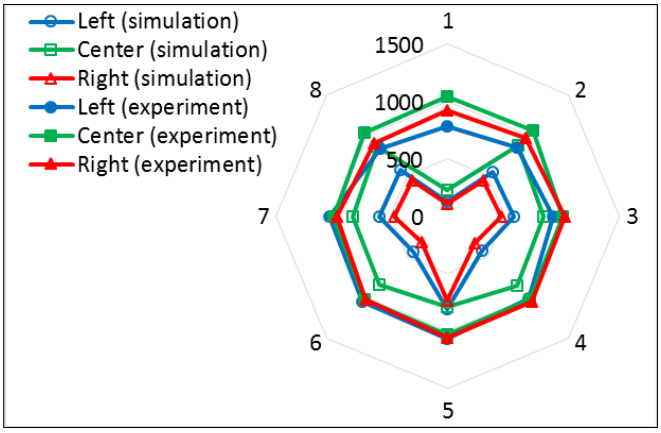

Figure 68. Spider plot of exterior to calorimeter temperatures (°C) at different angular-positions for Bakken pool fire

It is worth noting that, numerically, surrounding temperatures reach steady-state values almost instantaneously, while it takes about 10 ~ 20 minutes experimentally, to reach a steady state value. The reason is the absence of any thermal mass in the numerical model for solid objects such as the calorimeter, the steel floor, the fuel pan or the facility walls. However, during the experiments it takes few minutes for solid objects to reach a steady state. Consequently, thermocouples attached to solid objects takes longer time, in the experiment, to read a steady value.

5.3.5 Radiative Fraction & Soot Yield

5.3.5.1 OpenFOAM

Shown in Figure 69 is the radiative heat fraction and the soot yield from the numerical simulation. There is good agreement between numerical and experimental results; radiative fraction from the numerical simulation was ~ 44% (refer to Figure 24). Radiative fraction from the Bakken experiments ranged from 38 to 51% (refer to Figure 24b).

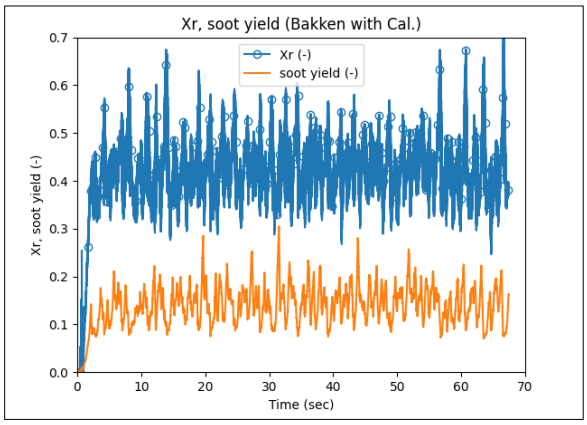

Figure 69. Numerical radiative fraction and soot yield results.

5.3.5.2 FDS

The numerical radiative fraction from FDS simulations for the Bakken with calorimeter case is shown in Figure 70. The average X_r is 39%, while the experimental value is 47%.

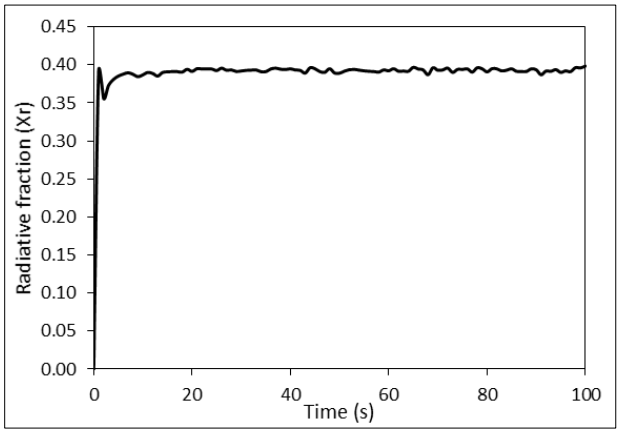

Figure 70. Numerical radiative fraction from FDS for the Bakken with calorimeter simulation

5.3.6 Heat Flux to Calorimeter

5.3.6.1 OpenFOAM

Shown in Figure 71 are the transient heat fluxes to the calorimeter from a) the numerical simulation and b) the experiment [2]. Shown in Figure 72 are the steady state values at different angular positions: numerical and experimental [38]. Shown in Figure 73 is the heat flux distribution over the calorimeter from the numerical simulation: a) top, b) side and c) bottom. There is good agreement between numerical and experimental results in terms of range and heat flux values to the calorimeter on the left and right cross sections. The numerical model seems to have overestimated the heat flux in the center cross section. However, there are only a few data points reported from the experiment due to thermocouple failure. Both numerical and experimental results indicate that the heat flux to the calorimeter is higher on the bottom of, rather than that on the top of the calorimeter.

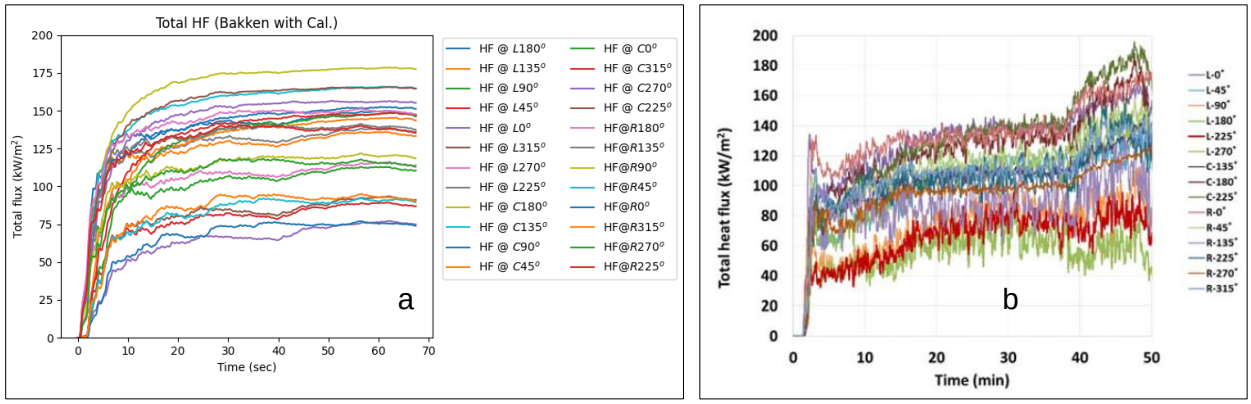

Figure 71. Total heat flux to calorimeter at different angular-positions: a) Numerical, b) Experimental

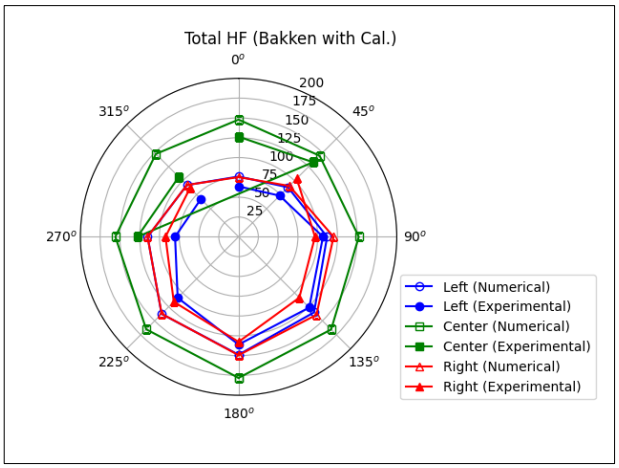

Figure 72. Spider plot of total heat flux (kW/m^2) to calorimeter at different angular-positions.

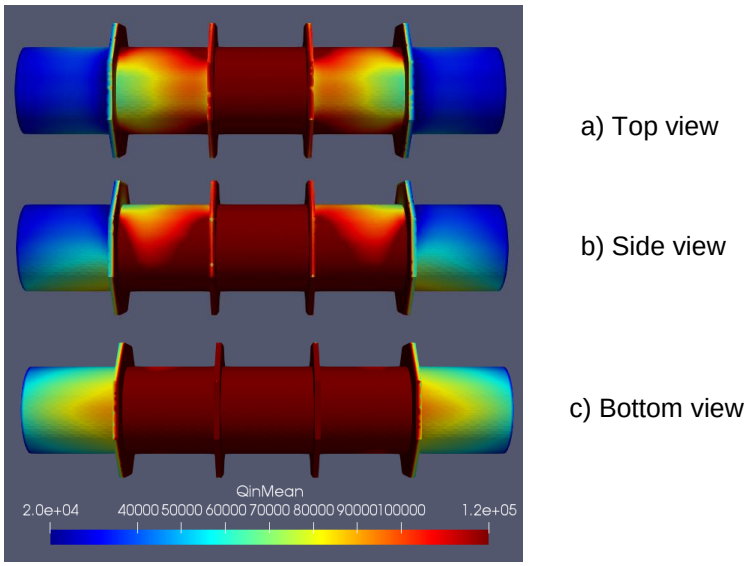

Figure 73. Heat flux (W/m^2) distribution (numerical): a) top view, b) side view, c) bottom view

5.3.6.2 FDS

Shown in Figure 74 are the contours of incident heat flux to the calorimeter. The maximum flux is 111 kW/m^2 and located on the bottom at the center plane of the calorimeter. Lower fluxes are observed on the sides of the calorimeter.

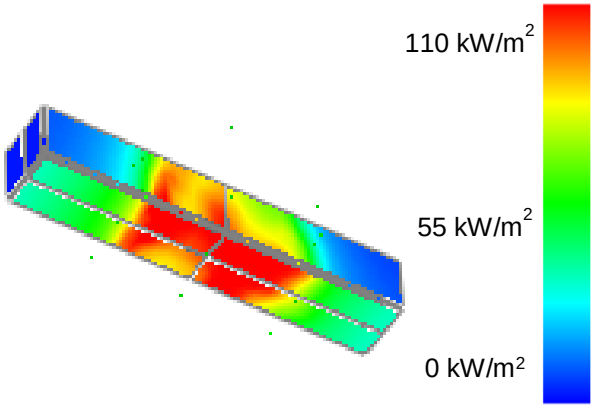

Figure 74. Incident heat flux on the calorimeter surface from Bakken pool fire simulation

5.3.7 Calorimeter Temperature

5.3.7.1 OpenFOAM

Shown in Figure 75 are the transient calorimeter temperatures from a) the numerical simulation and b) the experiment [2]. Shown in Figure 76 are the steady state values at different angular positions from the numerical and experimental results [38]. Shown in Figure 77 is the temperature distribution over the calorimeter from the numerical simulation: a) top, b) side and c) bottom.

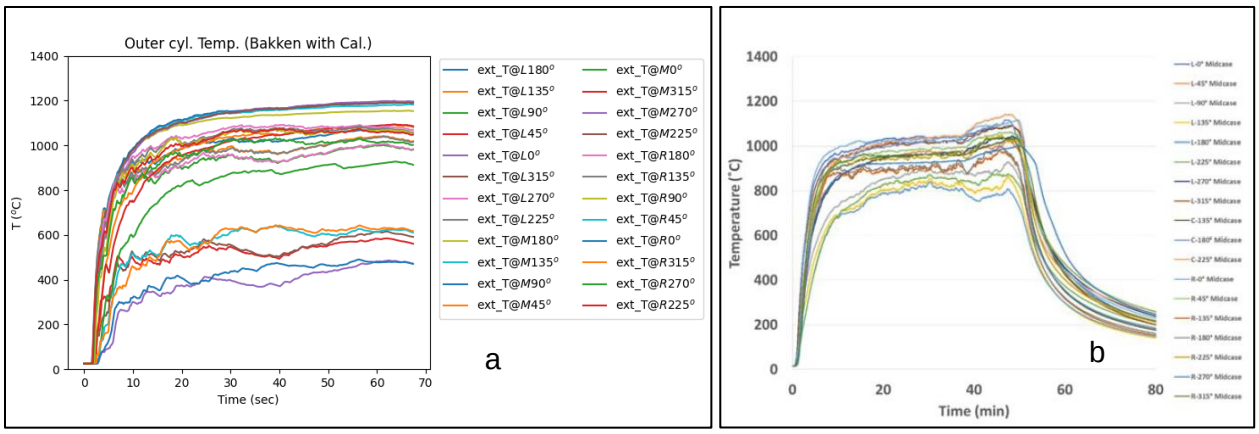

Figure 75. Outer cylinder temperatures at different angular-positions: a) Numerical, b) Experimental.

There is good agreement between numerical and experimental results in terms of range and values of each data point except for the top part of the left and right cross sections; the numerical model underestimated the temperature on the right and left top data point. The reason for this discrepancy is that, in the numerical model, the physical mass and thermal momentum of the calorimeter are not modeled. Heat transfer along the surface of the calorimeter is not modeled, while in the experimental setup, heat transfer to the top thermocouples could be conducted through the steel cylinders. Both numerical and experimental results indicates that the temperature on the bottom of the calorimeter is higher than the top.

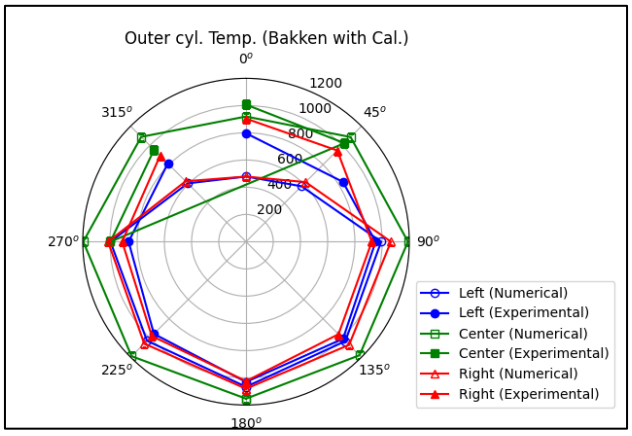

Figure 76. Spider plot of outer cylinder temperatures (°C) at different angular-positions.

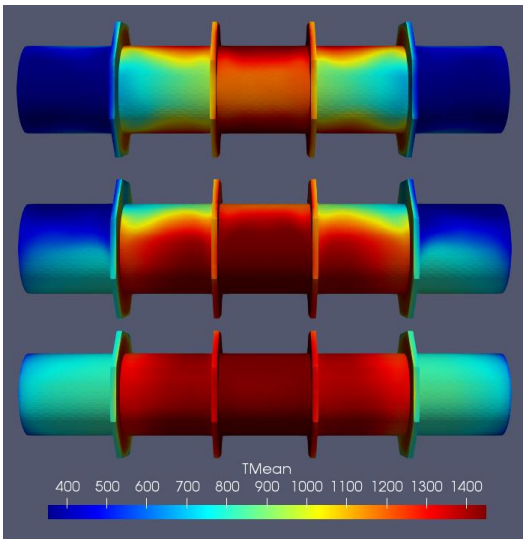

a) Top view

b) Side view

c) Bottom view

Figure 77. Calorimeter temperature distribution (K) (numerical): a) top view, b) side view, c) bottom view

5.3.8 Heat Release Rate (HRR)

5.3.8.1 OpenFOAM

Shown in Figure 78a are the HRR, radiative heat release and heat release due to soot oxidation from the numerical simulation. Shown in Figure 78b is the experimental HRR [2]. There is good agreement between the numerical and experimental results in terms of HRR. Numerical HRR was ~ 3.77 MW, while the experimental HRR was ~ 3.6 MW.

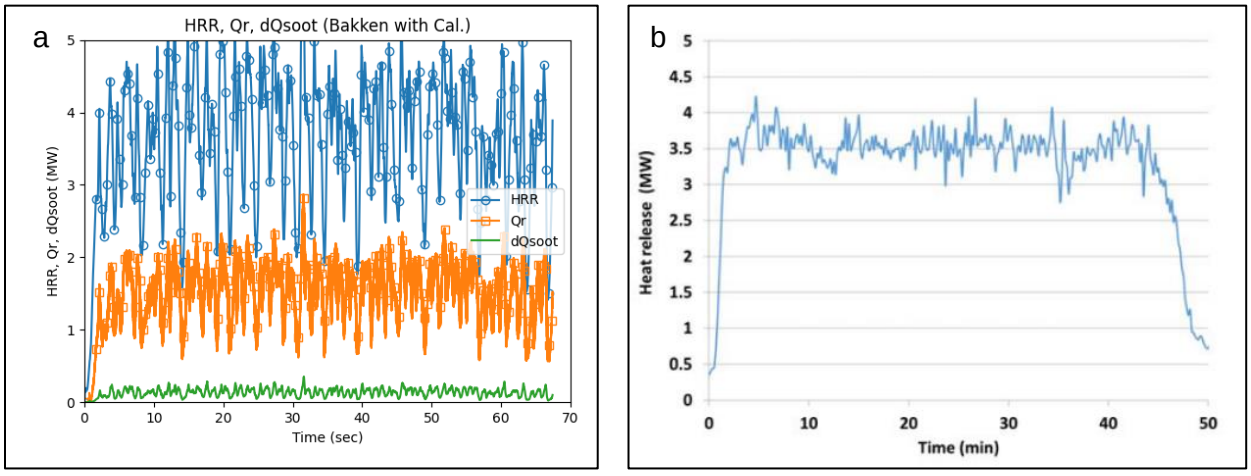

Figure 78. Time series results of heat release rate, radiative heat flux, soot radiative flux: a) Numerical, b) Experimental heat release rate.

5.3.8.2 FDS

The numerical HRR for the Bakken pool fire with calorimeter is presented in Figure 79. The numerical average HRR is 3.9 MW while the experimental value is 3.8 +/- 0.2 MW.

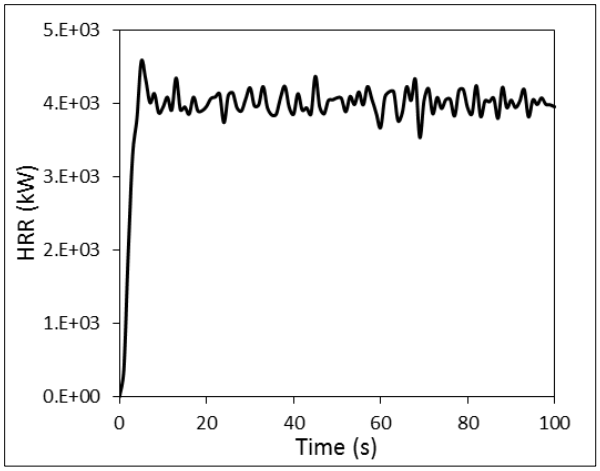

Figure 79. Numerical HRR for Bakken with calorimeter pool fire from FDS

5.3.9 Temperature Contours

5.3.9.1 OpenFOAM

Shown in Figure 80 are the temperature contours from a) the numerical simulation and b) the experiment [2]. The plotted contours are for temperatures values 750, 850, 950, 1050 and 1150 K. There is good agreement between numerical and experimental results in terms of shape and height of each contour except for the 850 K and 750 K contours. A possible reason for this difference is the way temperature contours are obtained experimentally; an infrared camera was used which might have been affected by the difference in emissivity from different flame areas. The numerical results would be closer to gas temperature measurements by a suction pyrometer equipped with a thermocouple.

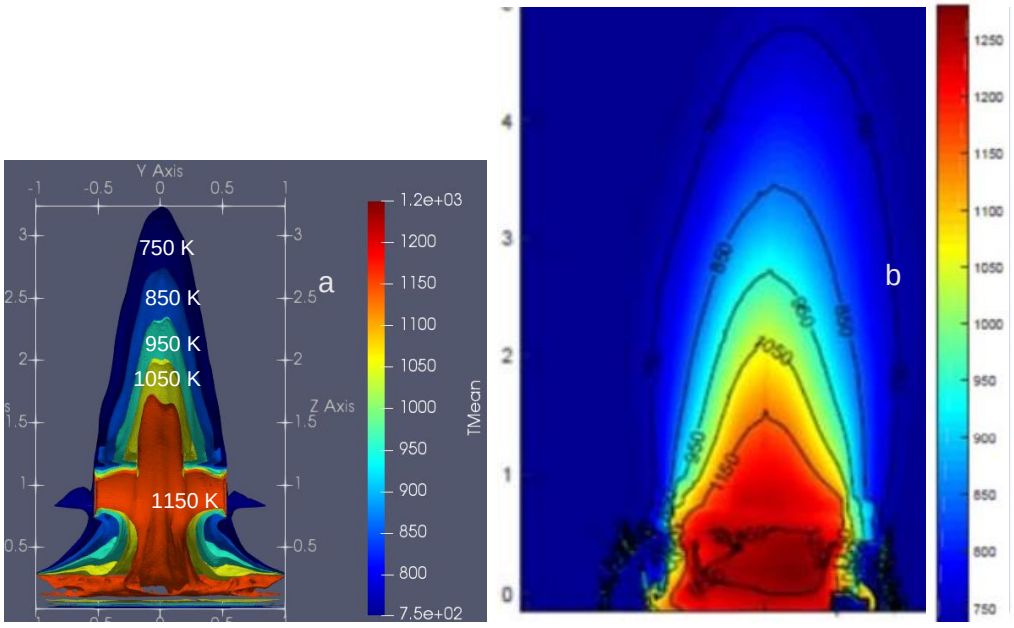

Figure 80. Temperature contours (Bakken with calorimeter): a) Numerical, b) Experimental

5.3.9.2 FDS

Shown in Figure 81are the temperature contours on the bottom surface of the calorimeter, which indicates higher temperatures compared to the top surface and the sides. The temperature range is 362-1161 °C.

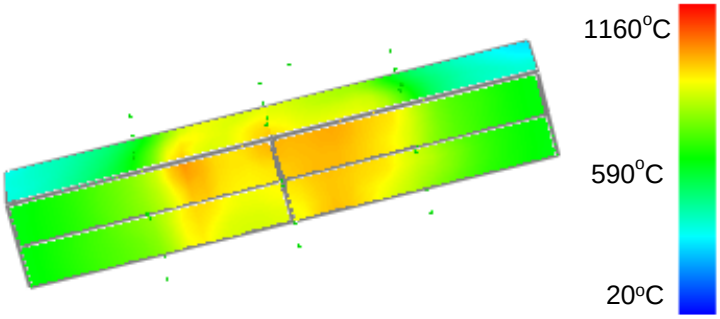

Figure 81. Temperature distribution on the bottom surface of the calorimeter from Bakken pool fire simulation

5.3.10 Radiation Contours and SEP

5.3.10.1 OpenFOAM

Shown in Figure 82a are the radiative heat flux contours from the numerical simulation. Shown in Figure 82b are the SEP contours from the experiment [2].

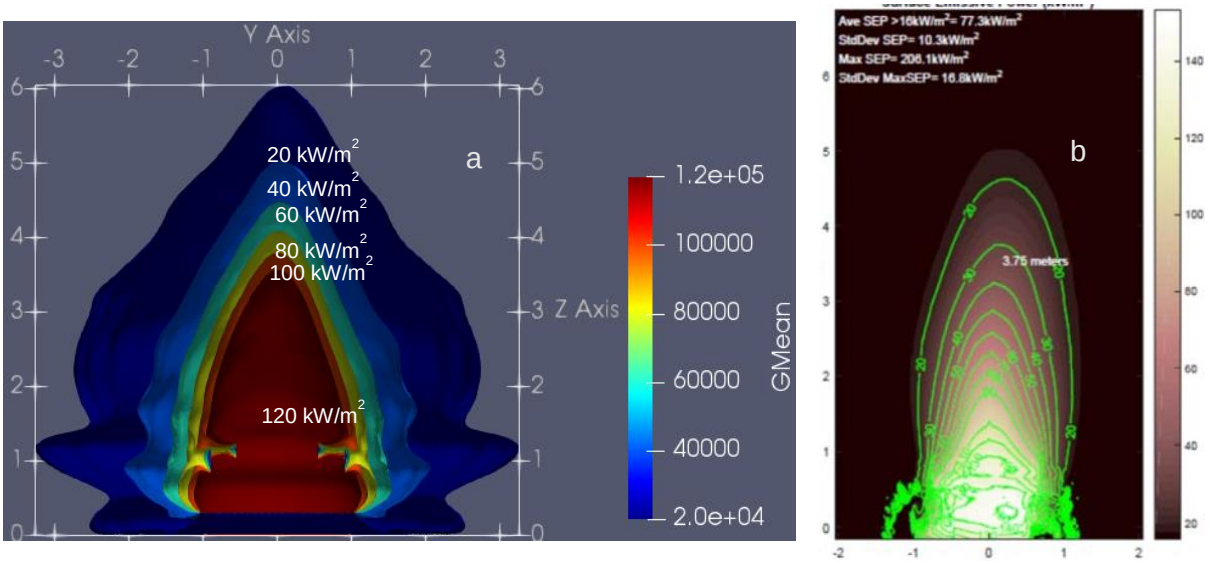

Figure 82. a) Radiative heat flux contours (numerical) b) SEP (experimental)

It is important to note that the radiative contours from the simulations are not equivalent to the SEP contours; the radiative contours represent the radiation field iso-surfaces around the flame. The SEP is the projected radiation on a single point in the field of view of the IR camera that is sensitive only to medium wave lengths of 3-5 micrometer located at a distance from the flame. Nonetheless, both have the same values for qualitative comparison. The presence of the

calorimeter seems to have distorted the numerical and experimental contours in the same manner (see results of radiation contours and SEP in Section 5.4.7, Figure 99 in comparison with Figure 82).

5.3.11 Wide Angle Heat Flux

5.3.11.1 OpenFOAM

Shown in Figure 83 are the transient wide angle heat fluxes from a) the numerical simulation (time-averaged), b) the experiment [2] and c) the numerical simulation (actual values). Shown in Figure 84 are the steady state values at different heights: a) heat flux versus height and b) height versus heat flux [38].

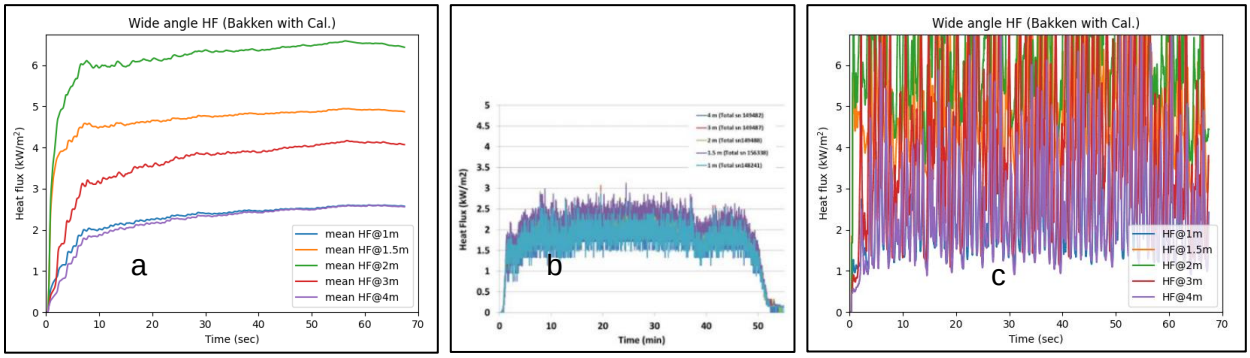

Figure 83. Wide angle heat fluxes of Bakken with calorimeter: a) Numerical, time-averaged, b) Experimental, c) Numerical (actual values).

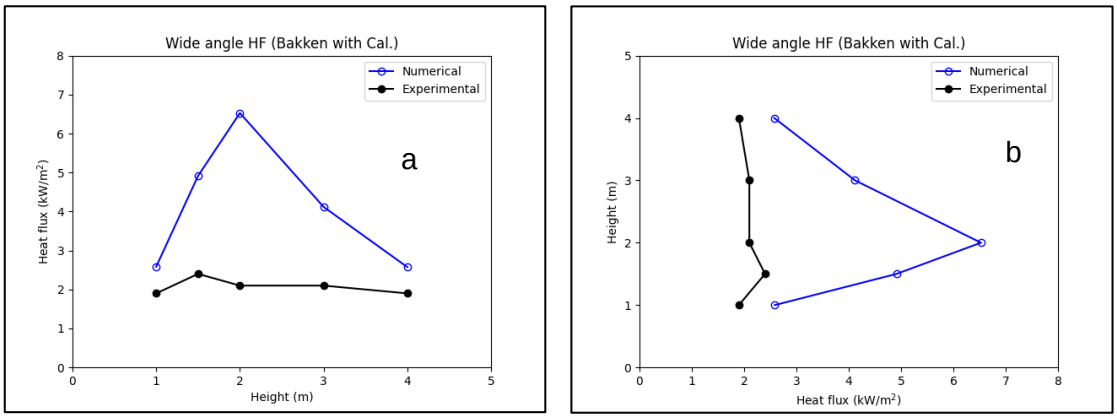

Figure 84. Average wide angle heat fluxes at different heights a) Flux vs. Height b) Height vs. Flux.

The numerical model overestimated the wide angle heat flux at all data points. As mentioned before, the main reason is the different distances at which the heat flux meters are located in the experiment (9 m) and the simulation (6 m). Also, experimentally, the wide angle heat flux is measured using a total heat flux gauge with a 180° view angle, which might have different sensitivity to different wave lengths. In the numerical model, all wavelengths are considered using the WSGG radiation model.

5.3.11.2 FDS

The wide angle radiometer readings from the experiment and simulation are compared in Figure 85. The simulations well-predicted the experimental results; where the range of both the numerical and experimental heat fluxes are 1.5-2.5 kW/m^2. The average wide angle heat fluxes from the simulation and experiment are compared in Figure 86.

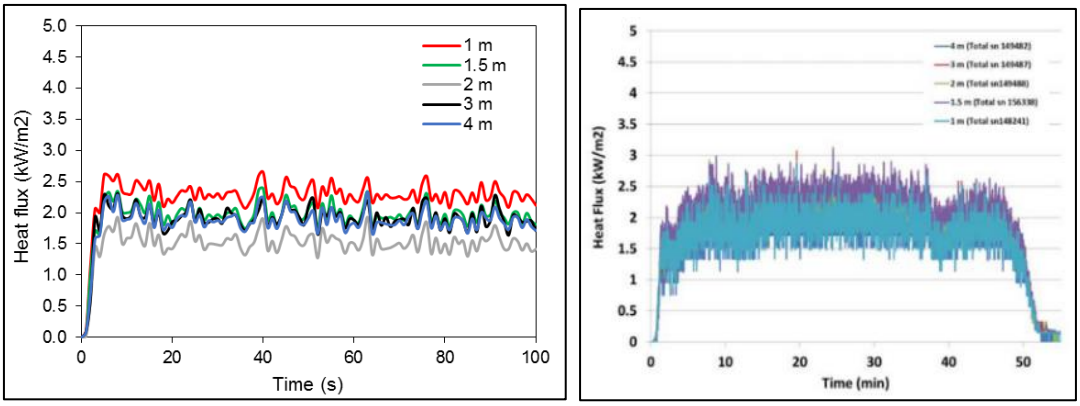

Figure 85. Wide angle radiometer readings for Bakken pool fire with calorimeter from simulations (left panel) and experiments (right panel)

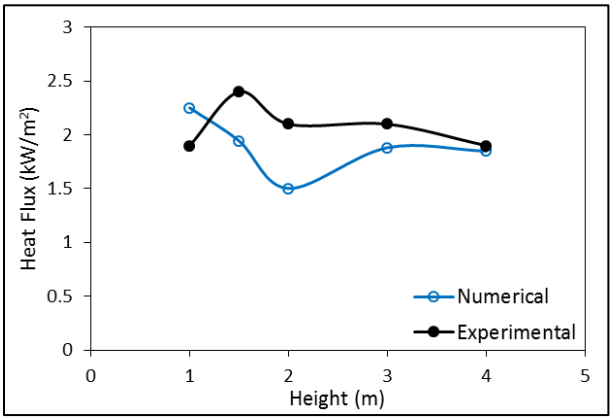

Figure 86. Average wide angle heat fluxes at different heights for Bakken with calorimeter pool fire from FDS simulations

5.3.12 Narrow Angle Heat Flux

5.3.12.1 OpenFOAM

Shown in Figure 87 are the transient narrow angle heat fluxes from a) the numerical simulation (time-averaged), b) the experiment [2] and c) the numerical simulation (actual values). Shown in Figure 88 are the steady state values at different heights: a) heat flux versus height and b) height versus heat flux [38]. Both numerical and experimental results have the same profile. However, the numerical model seems to be shifted upwards, overestimating the narrow angle heat flux values at all data points. The reason for that is the different methods used to calculate the heat flux (numerically) and measure the heat flux (experimentally); numerically, the narrow angle heat flux is estimated by sampling the radiation field close to the flame (i.e. at a distance

of 1.1 m from the pool center). In the numerical model, all wavelengths are considered using the WSGG radiation model. Experimentally, a 5.5° view angle radiometer with a zinc selenide window was used. The zinc selenide window has 70% transmissivity in the wavelength range 2-20 μm and zero transmissivity outside this range. That explains the lower narrow angle heat fluxes from the experimental results. It should be also noted that the surface emissive power measured by the IR camera was about 10% higher than the narrow angle radiometers.

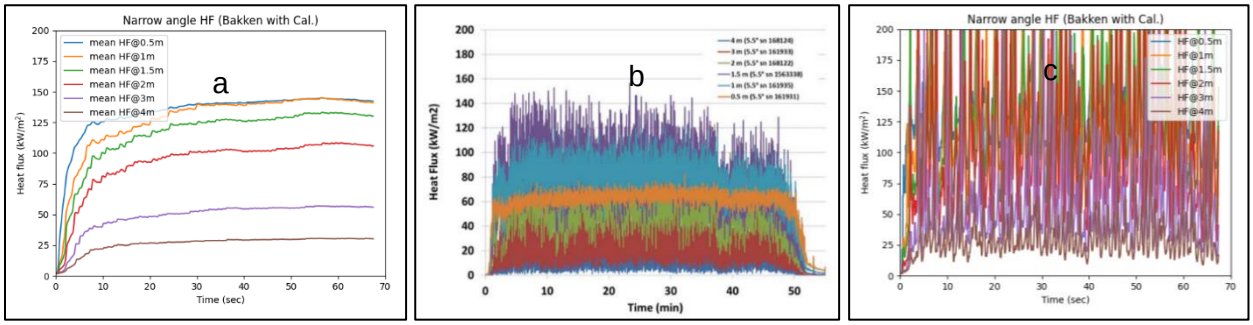

Figure 87. Narrow angle heat fluxes of Bakken with calorimeter: a) Numerical, time-averaged, b) Experimental, c) Numerical.

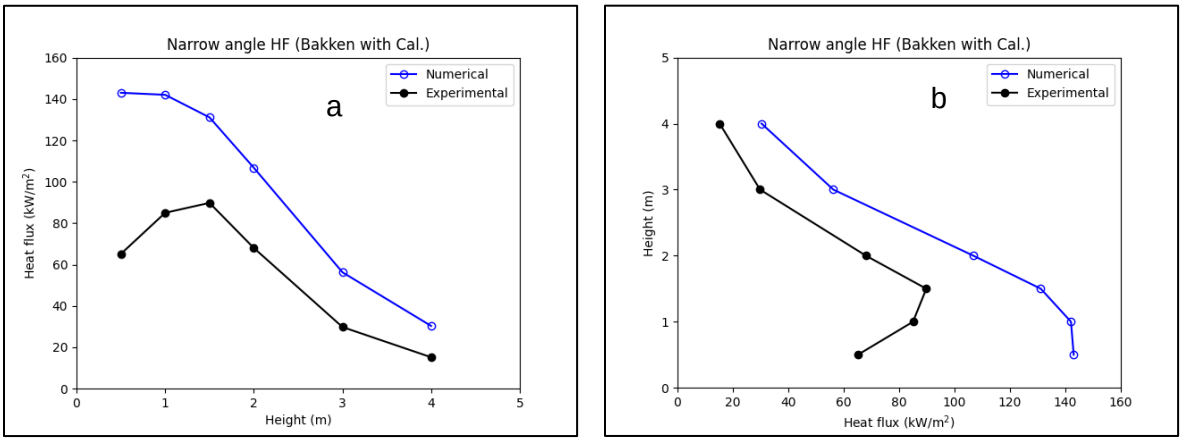

Figure 88. Average narrow angle heat fluxes at different heights: a) Flux vs. Height b) Height vs. Flux.

5.3.13 **Flame Height**

5.3.13.1 OpenFOAM

Shown in Figure 89 is the flame height from a) the numerical simulation and b) the experiment [2]. The numerical model underestimated the flame height. The reason is the different criteria used to define the flame height; numerically the flame height is defined by the highest point, in the domain, at which there is a nonzero value of the fuel concentration. Experimentally, the flame height is obtained using an IR camera which might have been affected by the radiation from soot particles at an elevated temperature. Given the fact that soot and high temperatures would coincide downstream from the fuel, it's expected that the numerical flame height is always lower than the flame height measured experimentally.

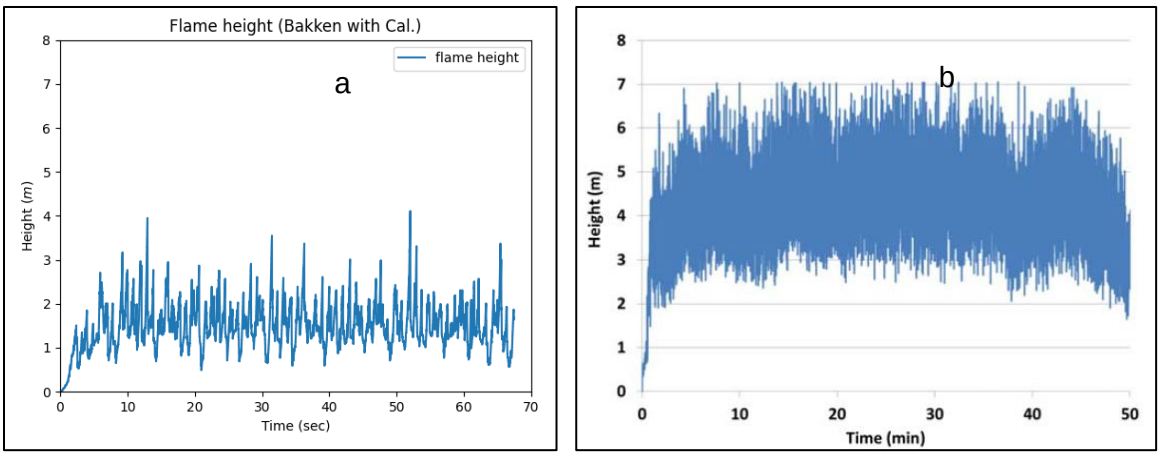

Figure 89. Flame height of Bakken with calorimeter: a) Numerical, b) Experimental.

5.4 Bakken without Calorimeter

5.4.1 OpenFOAM Results Summary

Discussed in this section are the validation results for the “Bakken without calorimeter” case. Numerical results are compared to experimental results from the NRC experiment at Sandia National Laboratories (Test 2.1) [2], [38]. Summary of the numerical and experimental ranges are shown in Table 19.

Table 19. Results summary for the Bakken without calorimeter simulation from OpenFOAM

Section	Validation parameter	Numerical range	Experimental range	Comments
5.4.3	Centerline temperature	278 – 882 C	268 – 943 C	Good agreement
5.4.4	Radiative fraction	42 %	38 – 51 %	Good agreement
5.4.5	HRR	4.5 MW	4.8 MW	Good agreement
5.4.4	Soot yield	13 %	Not reported	
5.4.6	Temperature contours	750 – 1150 K	750 – 1150 K	
5.4.8	Wide angle HF	3.6 – 6.3 kW/m^2	2.2 – 2.8 kW/m^2	Overestimated
5.4.9	Narrow angle HF	53 – 141 kW/m^2	21 – 121 kW/m^2	Overestimated
5.4.10	Flame height	2.13 m	5.35 m	Different criteria

5.4.2 FDS Results Summary

The FDS results from simulating the Bakken without calorimeter case are summarized in Table 20. Further discussion about each parameter is provided in the following subsections.

Table 20. Results summary for Bakken without calorimeter simulation from FDS

Section	Validation parameter	Numerical range	Experimental range	Comments
5.4.3	Centerline temperature	348 – 770 C	268 – 943 C	Reasonable agreement
5.4.4	Radiative fraction	38 %	44 %	Underestimated
5.4.5	HRR	4.4 MW	4.8 MW	Good agreement
5.4.8	Wide angle HF	1 – 1.5 kW/m^2	1.5 – 2.8 kW/m^2	Slightly underestimated
NA	Flame height	5 m	4.5 m	Good agreement

5.4.3 Plume Centerline Temperature

5.4.3.1 OpenFOAM

Shown in Figure 90 are the transient centerline temperatures from (a) the numerical simulations and (b) the experiments [2]. Shown in Figure 91 are the steady state centerline temperatures: a) temperature versus height and b) height versus temperature [38]. There is good agreement between the numerical and experimental results in terms of trend, range and values at each data point.

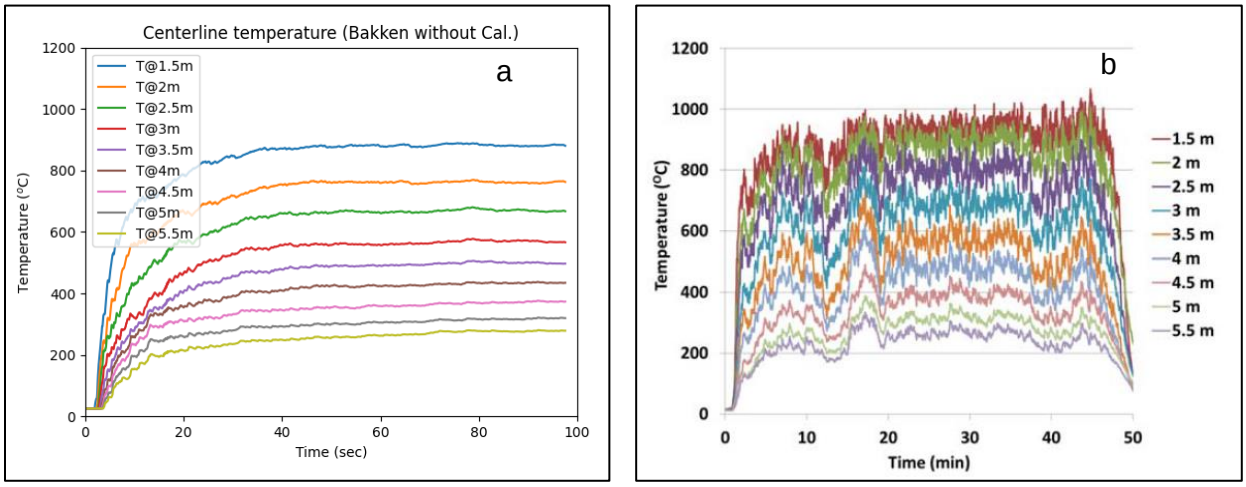

Figure 90. Centerline temperatures at different heights (Bakken without calorimeter): a) Numerical, b) Experimental.

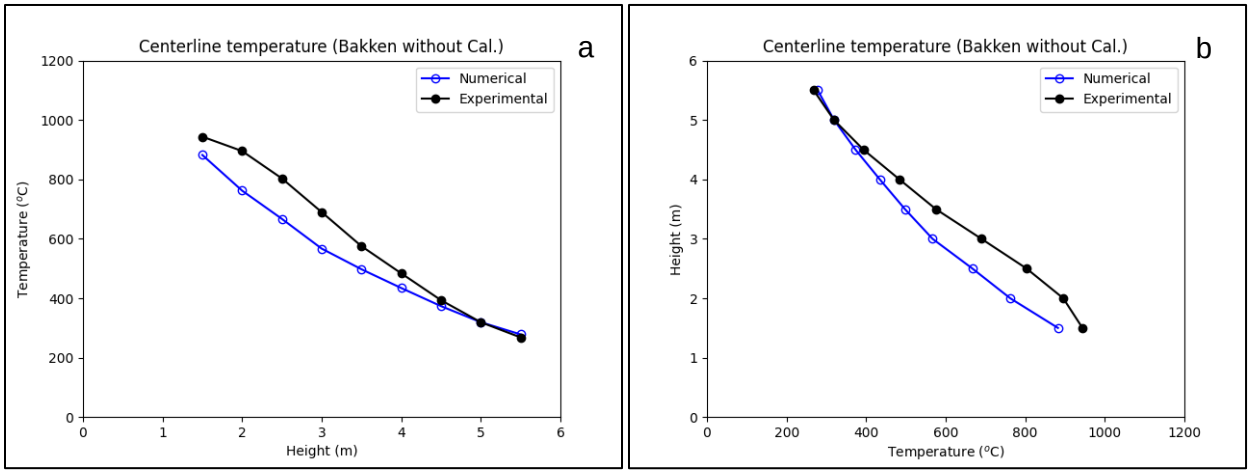

Figure 91. Average centerline temperatures at different heights a) Temp. vs. Height b) Height vs. Temp.

5.4.3.2 FDS

The results from simulating the Bakken pool fire without the calorimeter are compared against the experimental results from Test 2.1. Compared in Figure 92 are the experimental and numerical centerline temperatures. There is reasonable agreement between both sets. The

range of temperatures in the simulations is 348-770 °C, while the experimental range is 268-943 °C.

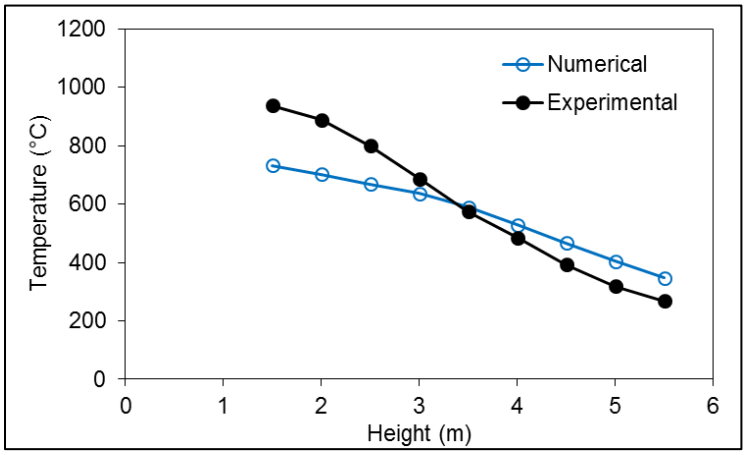

Figure 92. Average flame temperature at the centerline of the pool for Bakken pool fire without the calorimeter from the experiments (black line) and simulations (blue line)

5.4.4 Radiative Fraction & Soot Yield

5.4.4.1 OpenFOAM

Shown in Figure 93 are the radiative heat fraction and the soot yield from the numerical simulation. There is good agreement between numerical and experimental results; radiative fraction from the numerical simulation was ~ 42% (refer to Figure 24b). Radiative fraction from the Bakken experiments ranged from 38 to 51%.

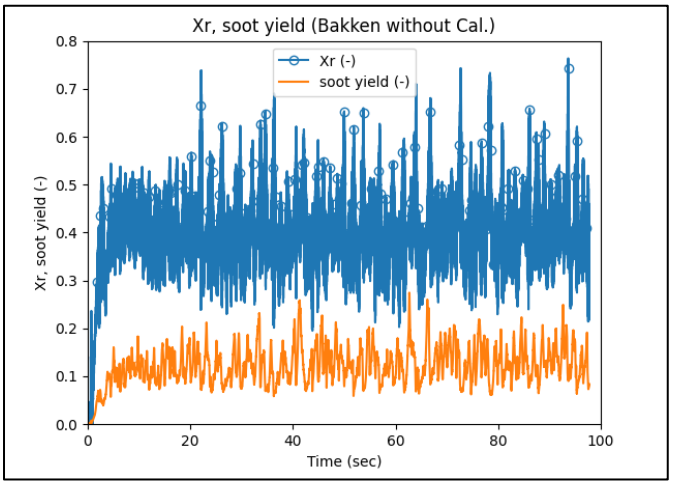

Figure 93. Numerical radiative fraction and soot yield results.

5.4.4.2 FDS

The numerical radiative fraction from FDS simulations for the Bakken with calorimeter case is shown in Figure 94. The average X_r is 38%, while the experimental value is 44%.

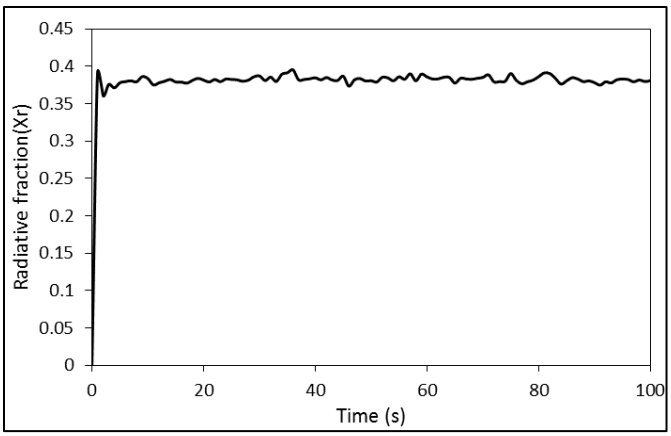

Figure 94. Numerical radiative fraction for Bakken without calorimeter pool fire

5.4.5 Heat Release Rate (HRR)

5.4.5.1 OpenFOAM

Shown in Figure 95a are the HRR, radiative heat release and heat release due to soot oxidation from the numerical simulation. Shown in Figure 95b is the experimental HRR [2]. There is good agreement between the numerical and experimental results in terms of HRR. Numerical HRR was ~ 4.5 MW, while the experimental HRR was ~ 4.8 MW.

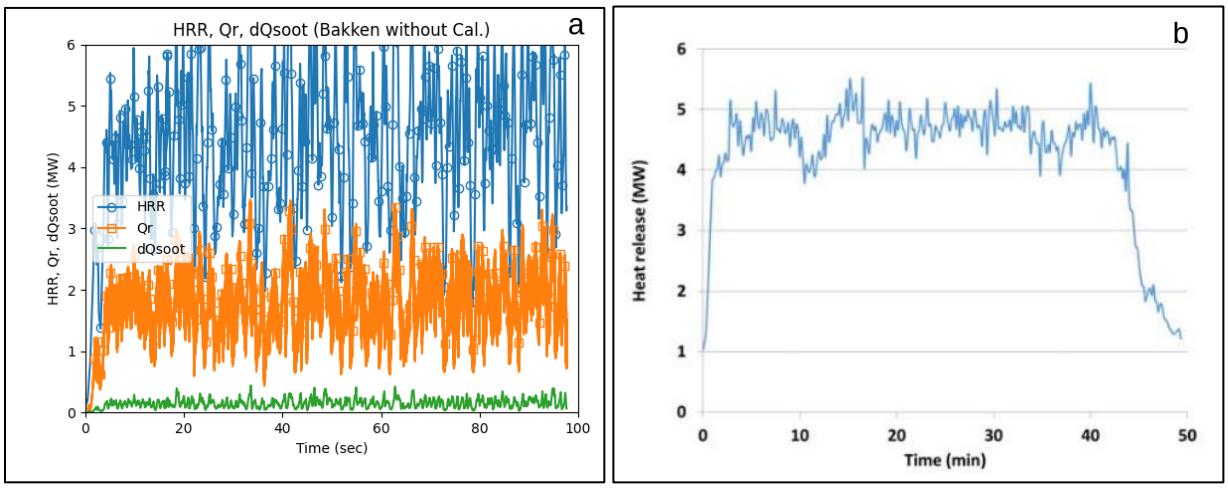

Figure 95. Time series results of heat release rate, radiative heat flux, soot radiative flux: a) Numerical, b) Experimental heat release rate.

5.4.5.2 FDS

The numerical HRR for the Bakken pool fire without calorimeter is presented in Figure 96. The numerical average HRR is 4.3 MW while the experimental value is 4.8 +/- 0.2 MW.

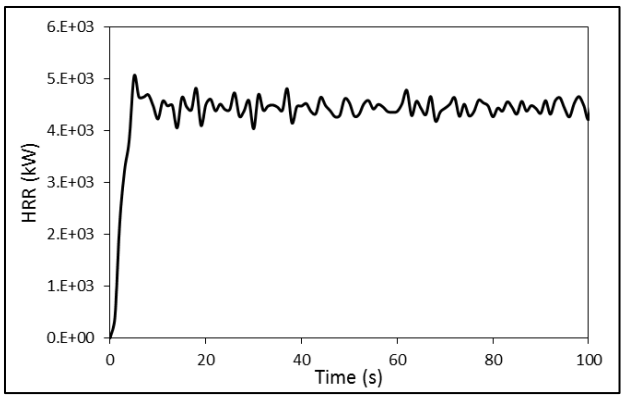

Figure 96. Numerical HRR for Bakken without calorimeter pool fire

5.4.6 Temperature Contours

5.4.6.1 OpenFOAM

Shown in Figure 97 are the temperature contours from a) the numerical simulation and b) the experiment [2]. The plotted contours are for temperatures values 750, 850, 950, 1050 and 1150 K. There is good agreement between numerical and experimental results in terms of shape and height of each contour except for the 750 K contour. A possible reason for this difference is the way temperature contours are obtained experimentally; an infrared camera was used which might have been affected by the difference in emissivity from different flame areas. The numerical results would be similar to gas temperature measurements made by a suction pyrometer equipped with a thermocouple.

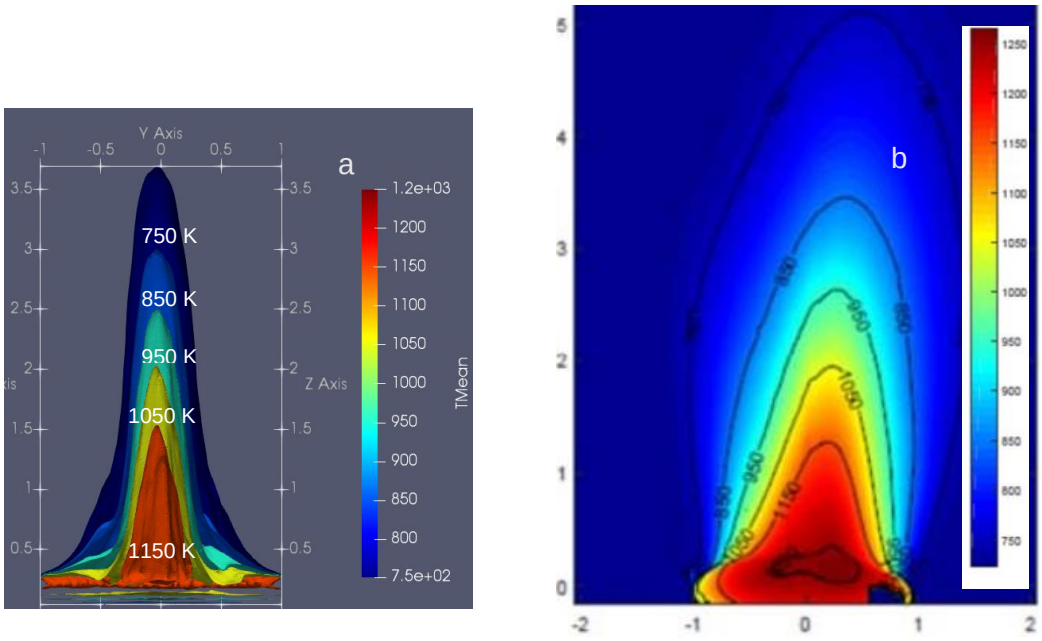

Figure 97. Temperature contours: a) Numerical, b) Experimental

5.4.6.2 FDS

Shown in Figure 98 are the temperature contours in the middle of the domain. The temperature within the flame ranges from 342 °C to 1200 °C.

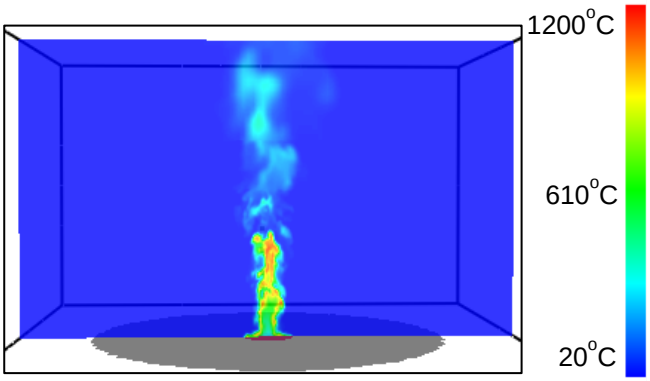

Figure 98. Temperature slice across the central plane of the flame in the simulations of Bakken pool fire without calorimeter

5.4.7 Radiation Contours and SEP

5.4.7.1 OpenFOAM

Shown in Figure 99a are the radiative heat flux contours from the numerical simulation. Shown in Figure 99b are the SEP contours from the experiment [2]. It is important to note that the radiative contours are not equivalent to the SEP contours; the radiative contours represent the radiation field iso-surfaces around the flame. The SEP is the projected radiation on a single point in the field of view of the IR camera that is sensitive only to medium wave lengths of 3-5 micrometer located at a distance from the flame. Nonetheless, both have the same values for qualitative comparison.

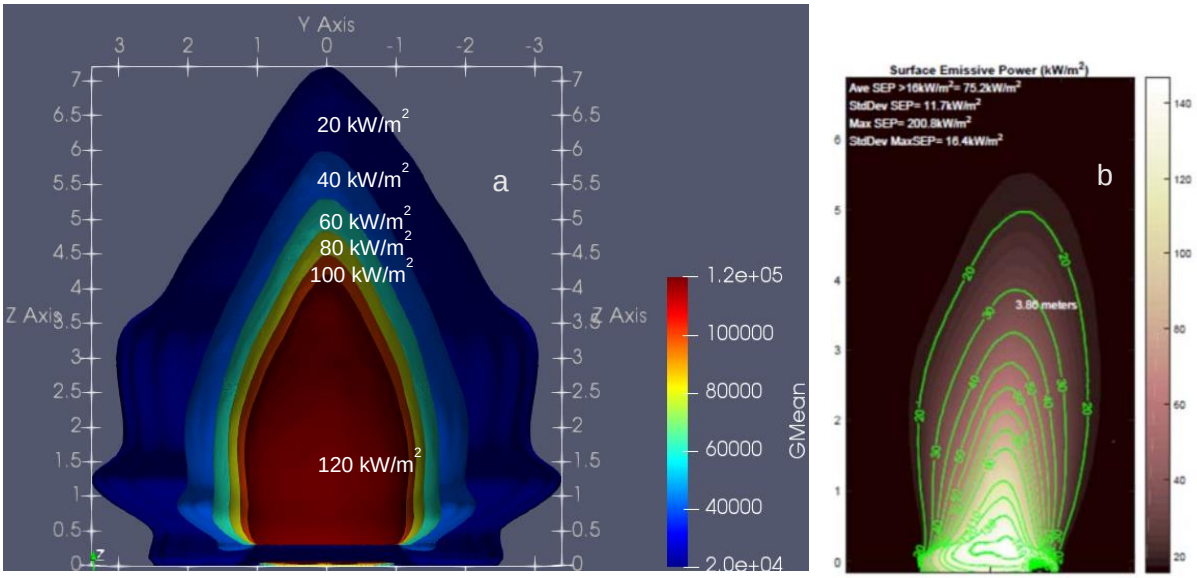

Figure 99. a) Radiative heat flux (Numerical) b) SEP (Experimental)

5.4.8 Wide Angle Heat Flux

5.4.8.1 OpenFOAM

Shown in Figure 100 are the transient wide angle heat fluxes from a) the numerical simulation (time-averaged), b) the experiment [2] and c) the numerical simulation (actual values). Shown in Figure 101 are the steady state values at different heights: a) heat flux versus height and b) height versus heat flux [38]. The numerical model overestimated the wide angle heat flux at all data points. As mentioned before, the main reason is the different distances at which the heat flux meters are located in the experiment (9 m) and the simulation (6 m). The intensity of heat flux decreases as the distance from the fire to the target increases (i.e. decrease proportional to square root of the distance).

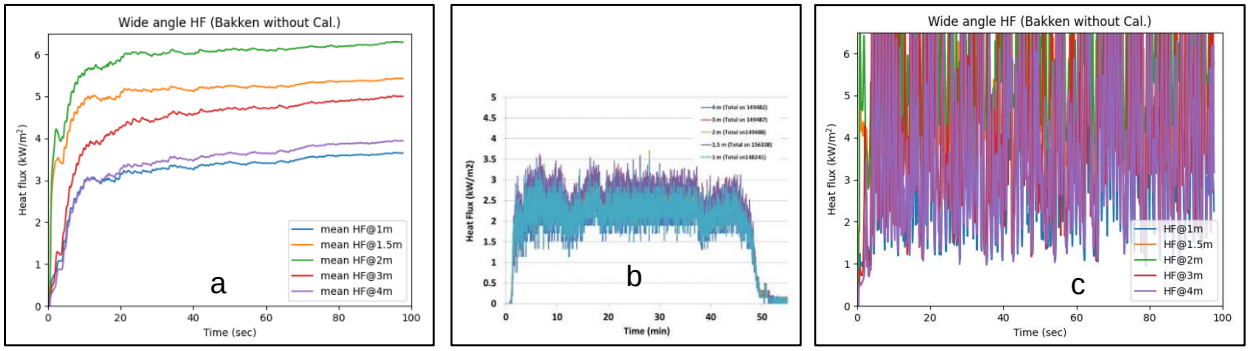

Figure 100. Wide angle heat fluxes of Bakken without calorimeter: a) Numerical, time-averaged, b) Experimental. c) Numerical.

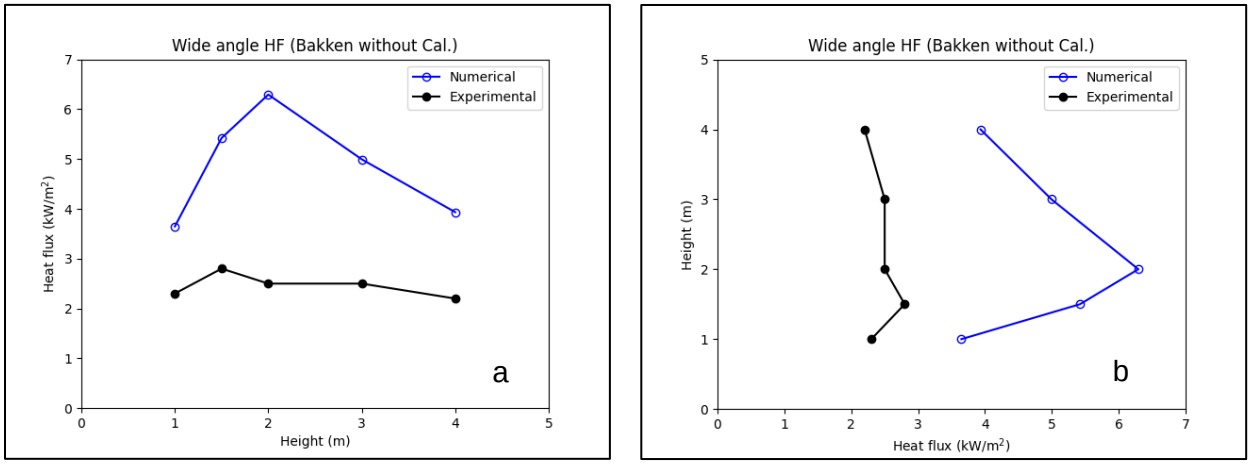

Figure 101. Average wide angle heat fluxes at different heights: a) Flux vs. Height b) Height vs. Flux.

Also, experimentally, the wide angle heat flux is measured using a total heat flux gauge with a 180° view angle, which might have different sensitivity to different wave lengths. In the numerical model, all wavelengths are considered using the WSGG radiation model.

5.4.8.2 FDS

The wide angle radiometer readings are presented in Figure 102. It can be seen that the simulations slightly underestimated the experimental values. The experimental range of heat flux is 1.5-3 kW/m^2; while the numerical one is 1-1.5 kW/m^2. The average wide angle heat fluxes from the simulation and experiment are compared in Figure 103.

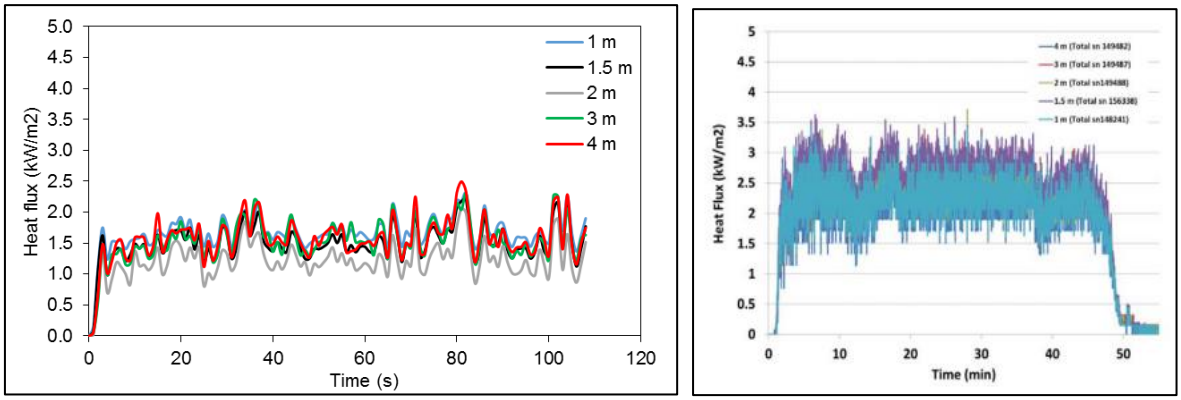

Figure 102. Wide angle radiometer readings for Bakken pool fire without calorimeter from simulations (left panel) and experiments (right panel)

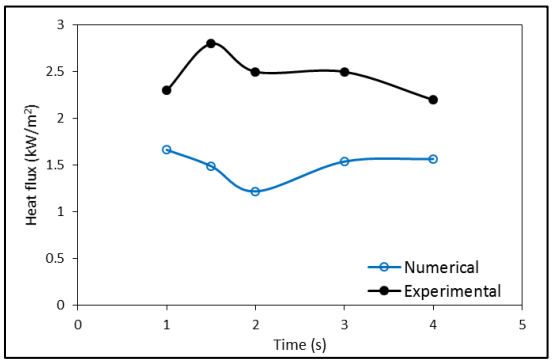

Figure 103. Average wide angle heat fluxes at different heights for Bakken without calorimeter pool fire from FDS simulations

5.4.9 Narrow Angle Heat Flux

5.4.9.1 OpenFOAM

Shown in Figure 104 are the transient narrow angle heat fluxes from a) the numerical simulation (time-averaged), b) the experiment [2] and c) the numerical simulation (actual values). Shown in Figure 105 are the steady state values at different heights: a) heat flux versus height and b) height versus heat flux [38]. The numerical model overestimated the narrow angle heat flux values at all data points except the first point at 0.5 m. The reason for that is the different methods used to calculate the heat flux (numerically) and measure the heat flux (experimentally); numerically, the narrow angle heat flux is estimated by sampling the radiation field close to the flame (i.e. at a distance of 1.1 m from the pool center). In the numerical model, all wavelengths are considered using the WSGG radiation model. Experimentally, a 5.5^o view angle radiometer with a zinc selenide window was used. The zinc selenide window has 70%

transmissivity in the wavelength range 2-20 μm and zero transmissivity outside this range. That explains the lower narrow angle heat fluxes from the experimental results.

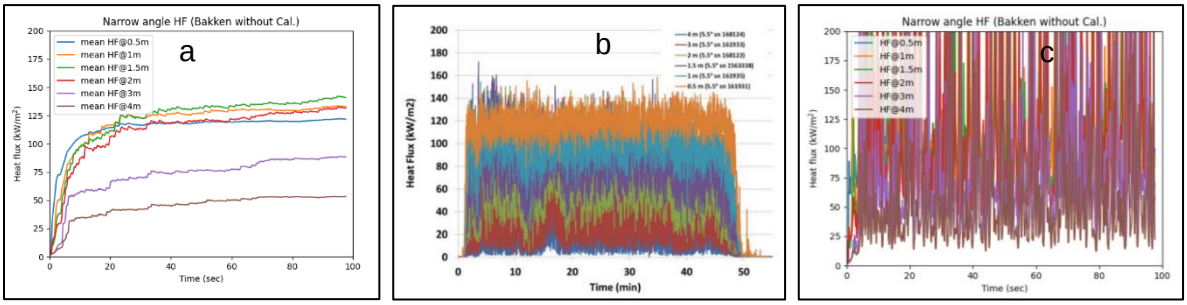

Figure 104. Narrow angle heat fluxes of Bakken without calorimeter: a) Numerical, time-averaged, b) Experimental, c) Numerical.

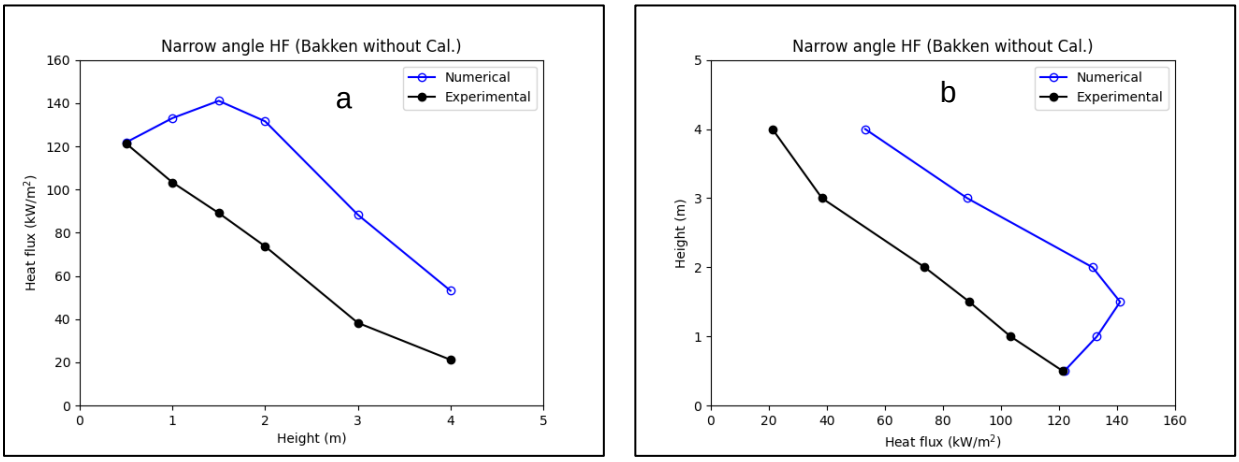

Figure 105. Average narrow angle heat fluxes at different heights: a) Flux vs. Height b) Height vs. Flux.

5.4.10 **Flame Height**

5.4.10.1 OpenFOAM

Shown in Figure 106 is the flame height from a) the numerical simulation and b) the experiment [2]. The numerical model underestimated the flame height. The reason is the different criteria used to define the flame height; numerically the flame height is defined by the highest point, in the domain, at which there is a nonzero value of the fuel concentration. Experimentally, the flame height is obtained using an IR camera which might have been affected by the radiation from soot particles at an elevated temperature. Given the fact that soot and high temperatures would coincide downstream from the fuel, it's expected that the numerical flame height is always lower than the flame height measured experimentally.

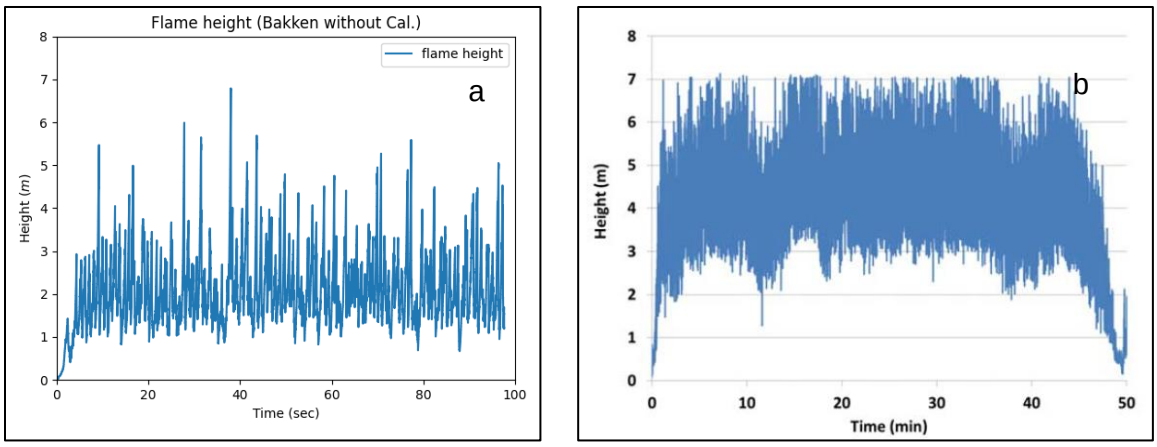

Figure 106. Flame height of Bakken without calorimeter: a) Numerical, b) Experimental.

5.5 Dilbit with Calorimeter

5.5.1 OpenFOAM Results Summary

Discussed in this section are the validation results for the “dilbit with calorimeter” case. Numerical results are compared to experimental results from the NRC experiment at Sandia National Lab (Test 3.5) [2], [38]. Summary of the numerical and experimental ranges are shown in Table 21.

Table 21. Results summary for the dilbit with calorimeter simulation from OpenFOAM

Section	Validation parameter	Numerical range	Experimental range	Comments
5.5.3	Centerline temperature	179 – 971 °C	140 – 1000 °C	Good agreement given variability in experimental results
5.5.4	Exterior to calorimeter temperature	421 – 1097 °C	680 – 1050 °C	Good agreement given absence of calorimeter conductivity in the numerical model
5.5.5	Radiative fraction	44%	60 %	Good agreement given experimental uncertainty
5.5.6	Heat flux to calorimeter	55 – 193 kW/m^2	40 – 145 kW/m^2	Good agreement given variability in experimental results
5.5.7	Calorimeter temperature	364 –1177 °C	695 – 1020 °C	Good agreement
5.5.8	HRR	3.2 MW	2.48 – 3.7 MW*	Good agreement
5.5.5	Soot yield	27%	Not reported	
5.5.9	Temperature contours	750 – 1150 K	750 -1150 K	
5.5.11	Wide angle HF	2 – 6 kW/m^2	1.1 – 1.9 kW/m^2	Overestimated
5.5.12	Narrow angle HF	19 – 121 kW/m^2	5 – 75 kW/m^2	Overestimated
5.5.13	Flame height	1.2 m	3.2 m	Different criteria

* lower limit from NRC-Sandia report [2]. Upper limit for NRC analysis report [38]

5.5.2 FDS Results Summary

The results from simulating the dilbit pool fire with the calorimeter are compared against the experimental results from Test 3.5. It is worth-noting that the results from the dilbit experiments were non-uniform over the duration of the experiment and an average burning rate (mass flux) was applied in the simulations. The results from FDS simulations are summarized in Table 22.

Table 22. Results summary for dilbit with calorimeter simulation from FDS

Section	Validation parameter	Numerical range	Experimental range	Comments
5.5.3	Centerline temperature	200 – 700 °C	140 – 1000 °C	Reasonable agreement given variability in experimental results
5.5.4	Exterior to calorimeter temperature	150-1000 °C	680 – 1050 °C	Underestimated
5.5.5	Radiative fraction	39.4%	60 %	Good agreement given experimental uncertainty
5.5.6	Heat flux to calorimeter	14 –111 kW/m^2	40 – 145 kW/m^2	Slightly underpredicted
5.5.7	Calorimeter temperature	500 – 933 °C	695 – 1020 °C	Slightly underpredicted
5.5.8	HRR	2.67 MW	2.48 – 3.7 MW*	Good agreement
5.5.11	Wide angle HF	1 – 2 kW/m^2	1.1 – 1.9 kW/m^2	Good agreement
NA	Flame height	3.8 m	3.6 m	

* lower limit from NRC-Sandia report [2]. Upper limit for NRC analysis report [38]

5.5.3 Plume Centerline Temperature

5.5.3.1 OpenFOAM

Shown in Figure 107 are the transient centerline temperatures from (a) the numerical simulations and (b) the experiment [2]. Shown in Figure 108 are the steady state centerline temperatures: a) temperature versus height and b) height versus temperature [38]. The two experimental lines are from the same experiment but with different time periods where fire parameters were different [38]. There is good agreement between the numerical and experimental results in terms of trend, range and values at each data point except for the middle section, where the numerical simulation overestimated the temperature. A possible reason is that the input flow rate in the numerical model might be higher than the actual burning rate during the experiment. The numerical input flow rate was taken as the mean value between 2.9 kg/min and 3.7 kg/min (see Section 6.3.5.3 in the Sandia report). However, given the variablity in the transient trend (Figure 107b), we could conclude that there is good agreement in general between the numerical and experimental results.

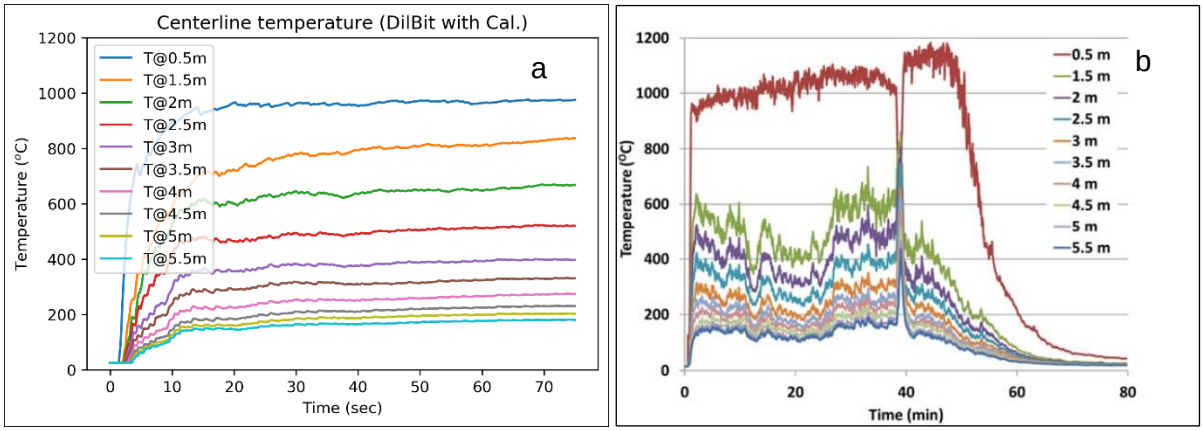

Figure 107. Centerline temperatures at different heights (dilbit with calorimeter): a) Numerical, b) Experimental.

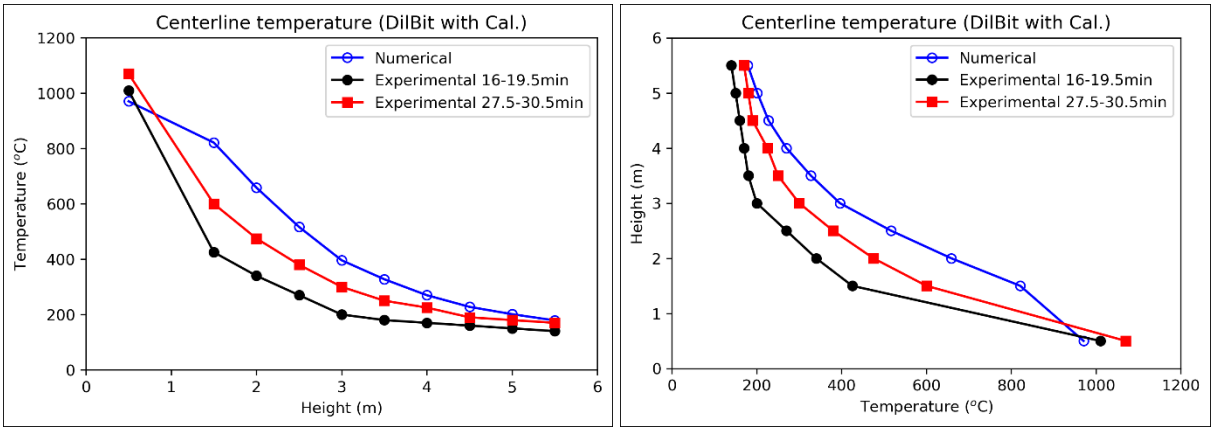

Figure 108. Average centerline temperatures at different heights: a) Temp vs. Height b) Height vs. Temp.

5.5.3.2 FDS

The experimental and numerical centerline temperatures are compared in Figure 109. Two sets of experimental average temperatures from the same test are shown, during 16 - 19.5 min and 27.5 - 30.5 min. Simulation results are in good agreement with the experiments in terms of trend and range. The numerical model overestimated the temperatures at the heights from 1.5 m to 3.5 m. A possible reason could be that the burning rate used in the simulation is higher than the burning rates in the experiment during the period reported; 16 - 19.5 min and 27.5 - 30.5 min. Nonetheless, the average temperature values from the simulations are closer to the experimental ones during the period from 27.5 to 30.5 min. This indicates that the burning rate specified in the simulation (3.4 kg/min) is close to the burning rate during that period.

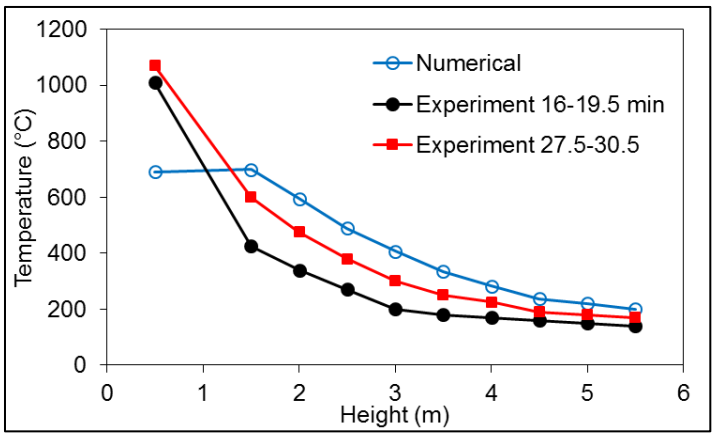

Figure 109. Average flame temperature at the centerline of the pool for dilbit pool fire with the calorimeter at 9 different heights from the simulations

5.5.4 Exterior to calorimeter Temperature

5.5.4.1 OpenFOAM

Shown in Figure 110 are the exterior to calorimeter temperatures from a) the numerical simulation and b) the experiment [2]. Shown in Figure 111 are the steady state values at different angular positions for the numerical and experimental results [38]. There is good agreement between numerical and experimental results on the center cross section. However, the numerical results underestimated the surrounding temperature on the left and right cross sections. A possible reason for this discrepancy is that, in the experimental setup, the surrounding thermocouples are attached to the calorimeter through steel rods. This would result in heating the thermocouple by conduction from the calorimeter to the thermocouples. Both numerical and experimental results indicate that the surrounding temperature is higher under the calorimeter than the temperature above the calorimeter.

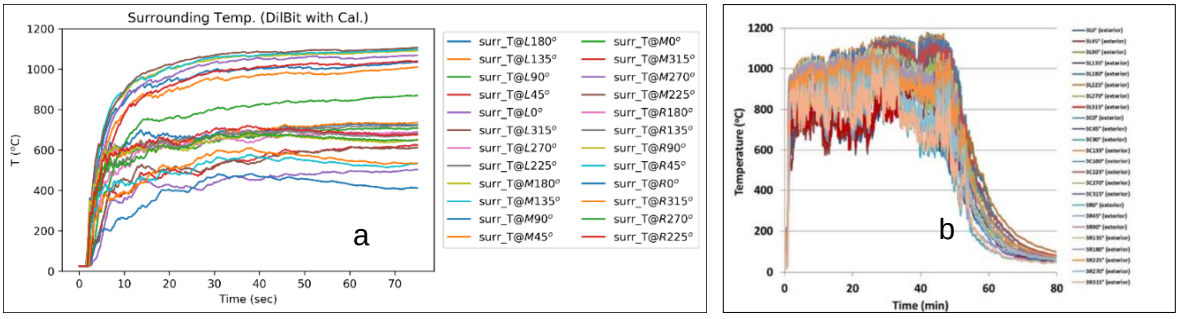

Figure 110. Exterior to calorimeter temperatures at different angular-positions: a) Numerical, b) Experimental.

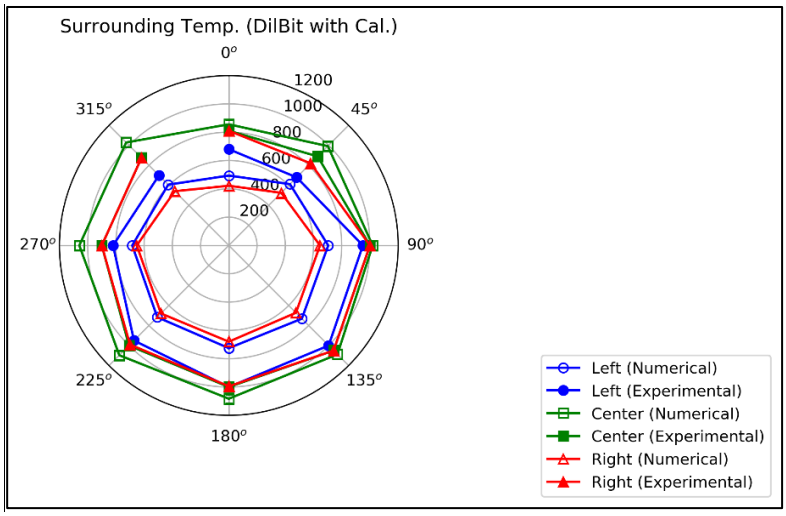

Figure 111. Spider plot of Exterior to calorimeter temperatures (°C) at different angular-positions.

5.5.4.2 FDS

The temperature values surrounding the calorimeter are shown in Figure 112. The experimental range is 680-1050 °C while the numerical range is 150-1000 °C. The spider plot comparing the average temperatures surrounding the calorimeter at different angles and planes from the simulation and experiment is shown in Figure 113. Similar to the previous observations, much lower temperatures are observed from the simulations at the left and right planes. The simulated temperatures at the central plane are in reasonable agreement with the experimental temperatures, except for the temperature above the calorimeter.

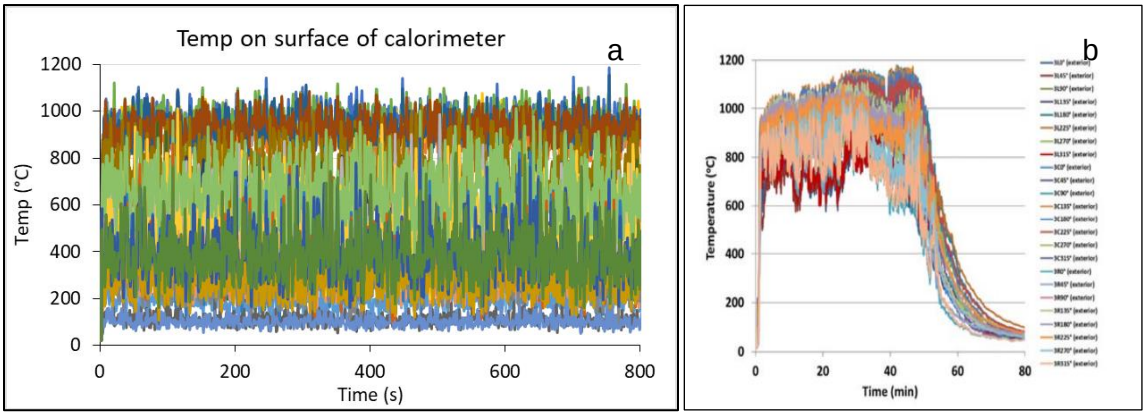

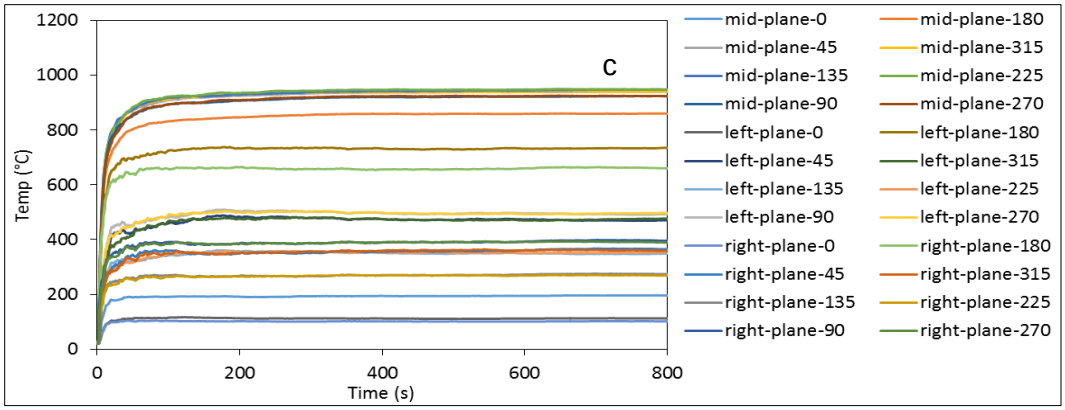

Figure 112. Temperatures on surface of calorimeter from dilbit pool fire from a) simulations as raw data, b) experimental and c) time-averaged (numerical)

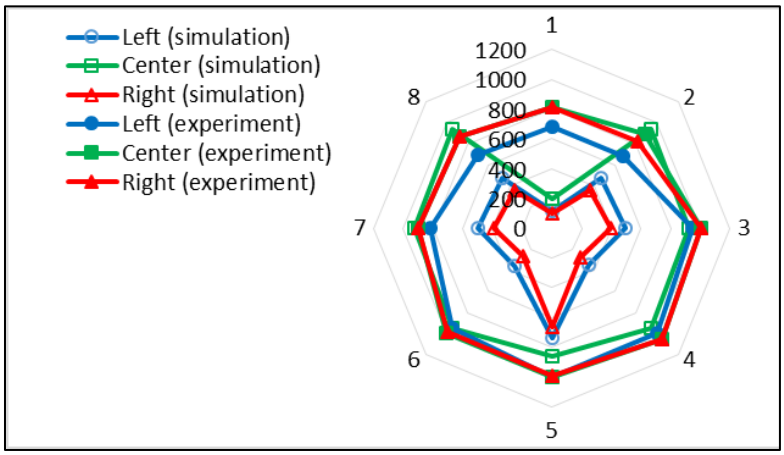

Figure 113. Spider plot of exterior to calorimeter temperatures (°C) at different angular-positions for dilbit pool fire

5.5.5 Radiative Fraction & Soot Yield

5.5.5.1 OpenFOAM

Shown in Figure 114 is the radiative heat fraction and the soot yield from the numerical simulation. Numerical radiative heat fraction was ~ 44%. Experimental radiative heat fraction was 60%. It is important to take into consideration that the experimental heat fraction was estimated from one experiment only based on the measured HRR with significant uncertainty in the measurements, unlike heptane and Bakken where several experiments were used to obtain a range of radiative heat fractions. Also, it is important to note the maximum possible radiative fraction estimated empirically by De Ris [37] is ~ 43%. De Ris [37] estimated the radiative fraction as a function of the smoke point height through an empirical fitting of experimental values (see Figure 114b).

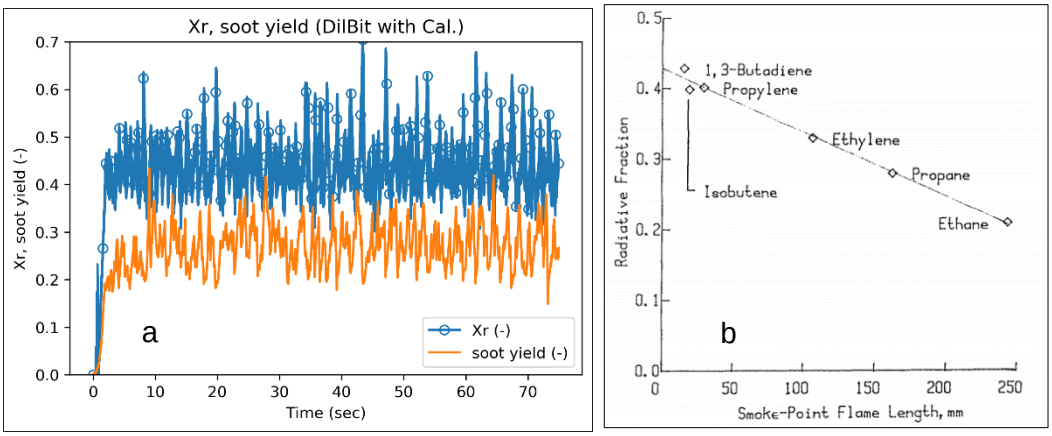

Figure 114. a) Numerical radiative fraction and soot yield results b) Radiative fraction for various hydrocarbons versus smoke point height from literature [37]

5.5.5.2 FDS

The numerical radiative fraction from FDS simulations for the dilbit with calorimeter case is shown in Figure 115. The average numerical X_r is 39%, while the experimental value is 60%.

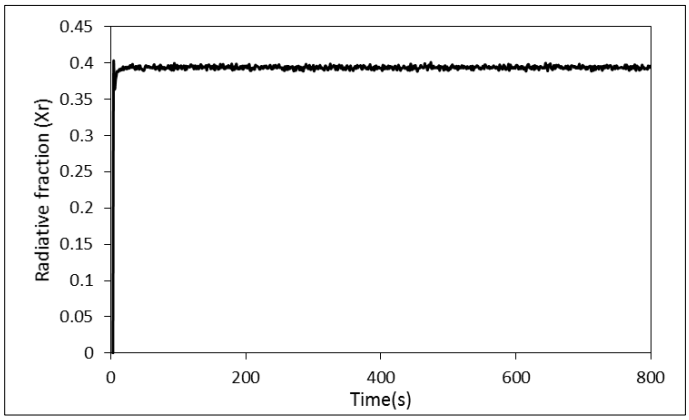

Figure 115. Numerical radiative fraction from FDS for dilbit with calorimeter simulation

5.5.6 Heat Flux to Calorimeter

5.5.6.1 OpenFOAM

Shown in Figure 116 are the transient heat fluxes to the calorimeter from a) the numerical simulation and b) the experiment [2]. Shown in Figure 117 are the steady state values at different angular positions for the numerical and experimental results [38]. Shown in Figure 118 is the heat flux distribution over the calorimeter from the numerical simulation: a) top, b) side and c) bottom. There is good agreement between numerical and experimental results on the left and right cross sections. However, the numerical model overestimated the heat flux on the center cross section. Given the variability in the transient heat flux (Figure 116b), there is good agreement in general. Both numerical and experimental values indicate that the bottom was subjected to a higher heat flux than the top of the calorimeter (see Figure 117 and Figure 118).

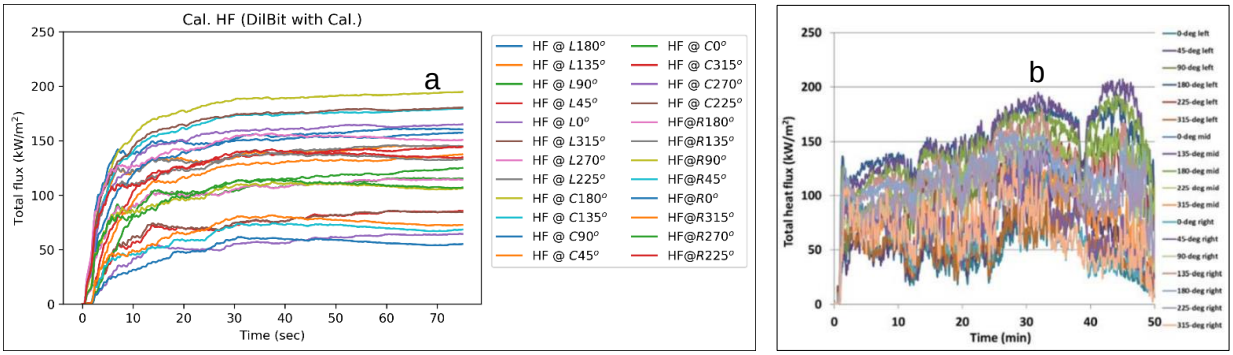

Figure 116. Total heat flux to calorimeter at different angular-positions: a) Numerical, b) Experimental.

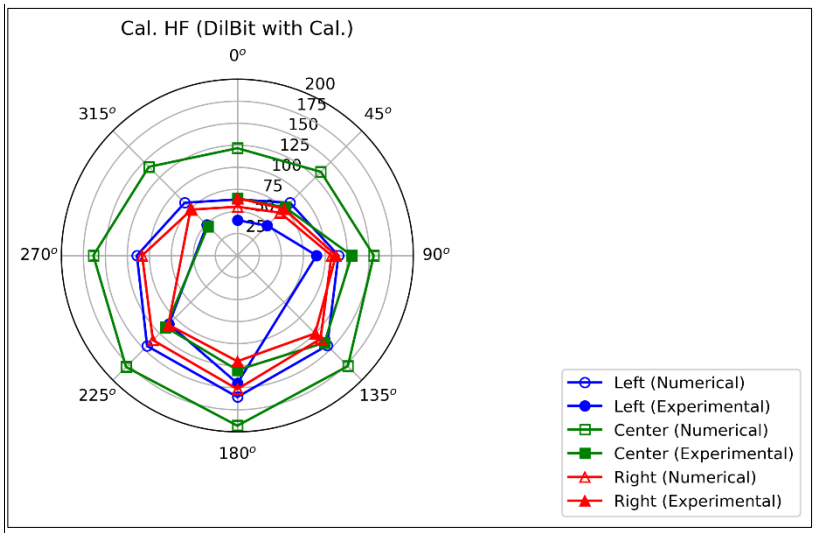

Figure 117. Spider plot of total heat flux (kW/m^2) to calorimeter at different angular-positions.

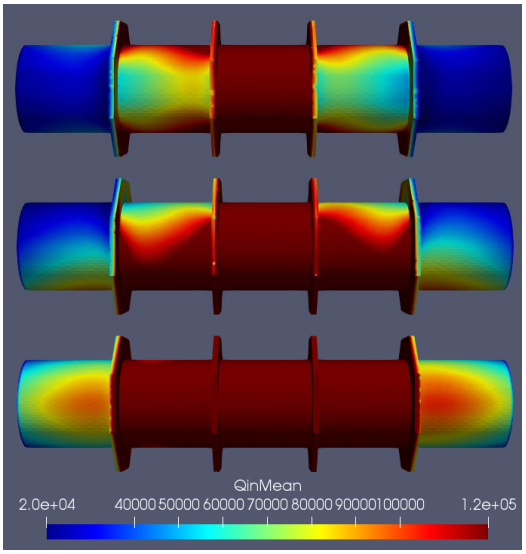

a) Top view

b) Side view

c) Bottom view

Figure 118. Heat flux (W/m^2) distribution (numerical): a) top view, b) side view, c) bottom view

5.5.6.2 FDS

Shown in Figure 119 are the contours of incident heat flux to the calorimeter. The maximum flux is 111 kW/m^2 located at the center of the bottom surface of the calorimeter. Lower fluxes are observed on the sides.

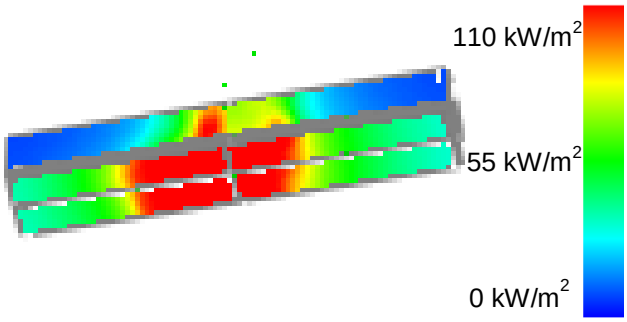

Figure 119. Incident heat flux on the calorimeter surface from dilbit pool fire simulation

5.5.7 Calorimeter Temperature

5.5.7.1 OpenFOAM

Shown in Figure 120 are the transient calorimeter temperatures from a) the numerical simulation and b) the experiment [2]. Shown in Figure 121 are the steady state values at different angular positions for the numerical and experimental results [38]. Shown in Figure 122 is the temperature distribution over the calorimeter from the numerical simulation: a) top, b) side and c) bottom. There is good agreement between numerical and experimental results in terms of range and values of each data point except for the top part of the left and right cross sections: the numerical model underestimated the temperature on the right and left top data point. The reason for this discrepancy is that, in the numerical model, the physical mass and thermal momentum of the calorimeter are not modeled. Heat transfer along the surface of the calorimeter is not modeled, while in the experimental setup, heat transfer to the top thermocouples could be conducted through the steel cylinders. Both numerical and experimental results indicates that the temperature on the bottom of the calorimeter is higher than the top.

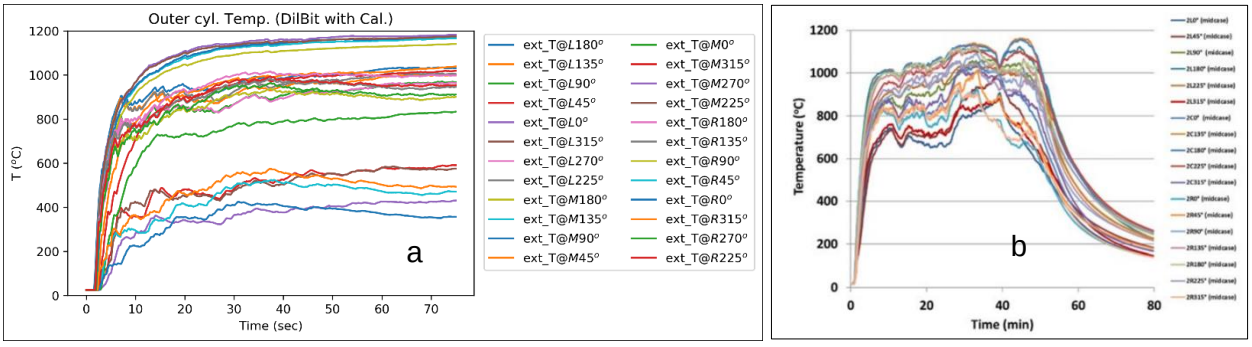

Figure 120. Outer cylinder temperatures at different angular-positions: a) Numerical, b) Experimental.

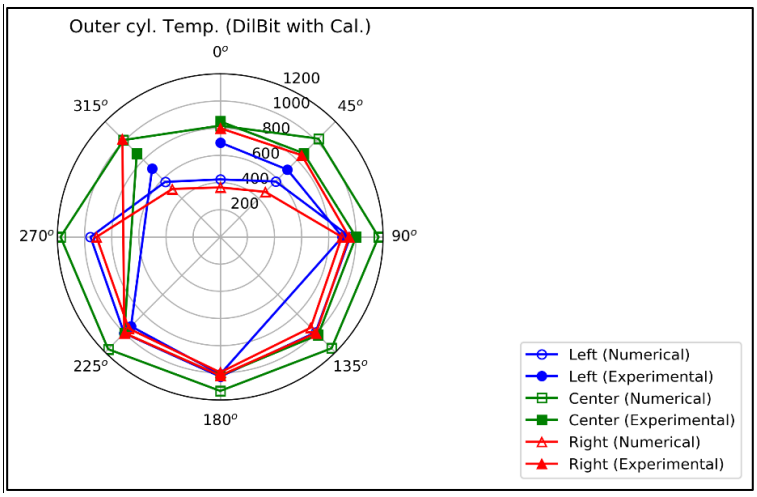

Figure 121. Spider plot of outer cylinder temperatures (°C) at different angular-positions.

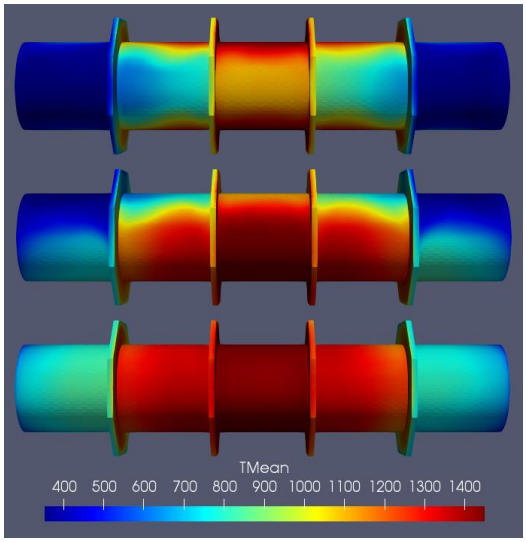

a) Top view

b) Side view

c) Bottom view

Figure 122. Calorimeter temperature distribution (K) (numerical): a) top view, b) side view, c) bottom view.

5.5.8 Heat Release Rate (HRR)

5.5.8.1 OpenFOAM

Shown in Figure 123 are the HRR, radiative heat release and heat release due to soot oxidation from the numerical simulation. Numerically, the HRR was ~ 3.2 MW. Experimentally, two values of HRR were reported: 2.48 MW estimated from the burning rate (test 3.5) and 3.7 MW calculated from data collected using the gas analyzer from a different test (test 3.4, the only test where gas analyzer data was collected) [2], [38].

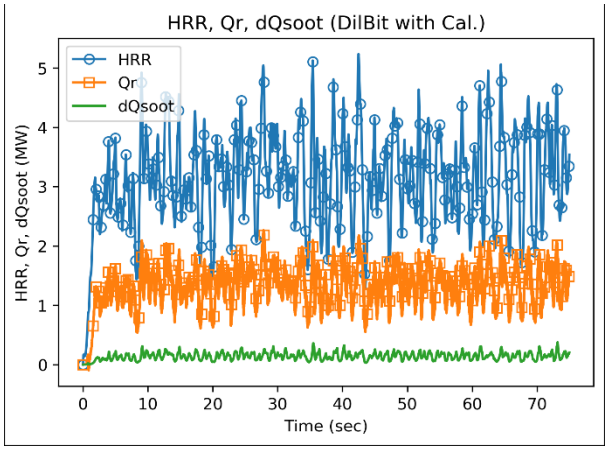

Figure 123. Time series results of heat release rate, radiative heat flux, soot radiative flux.

5.5.8.2 FDS

The numerical HRR for the dilbit pool fire with calorimeter is presented in Figure 124. The numerical average HRR is 2.67 MW while the experimental value is 2.48 +/- 0.2 MW.

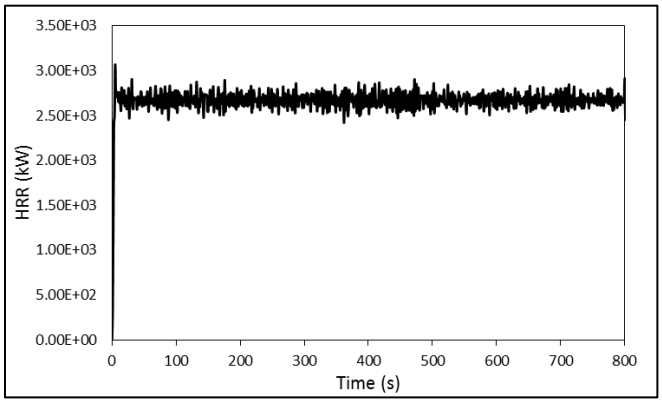

Figure 124. Numerical HRR for dilbit with calorimeter pool fire

5.5.9 Temperature Contours

5.5.9.1 OpenFOAM

Shown in Figure 125 are the temperature contours from a) the numerical simulation and b) the experiment [2]. The plotted contours are for temperatures values 750, 850, 950, 1050 and 1150 K. There is a mismatch between numerical and experimental contours in terms of shape. The IR camera seem to have been angled differently in this experiments given that the projection of the pan is visible in the experimental picture.

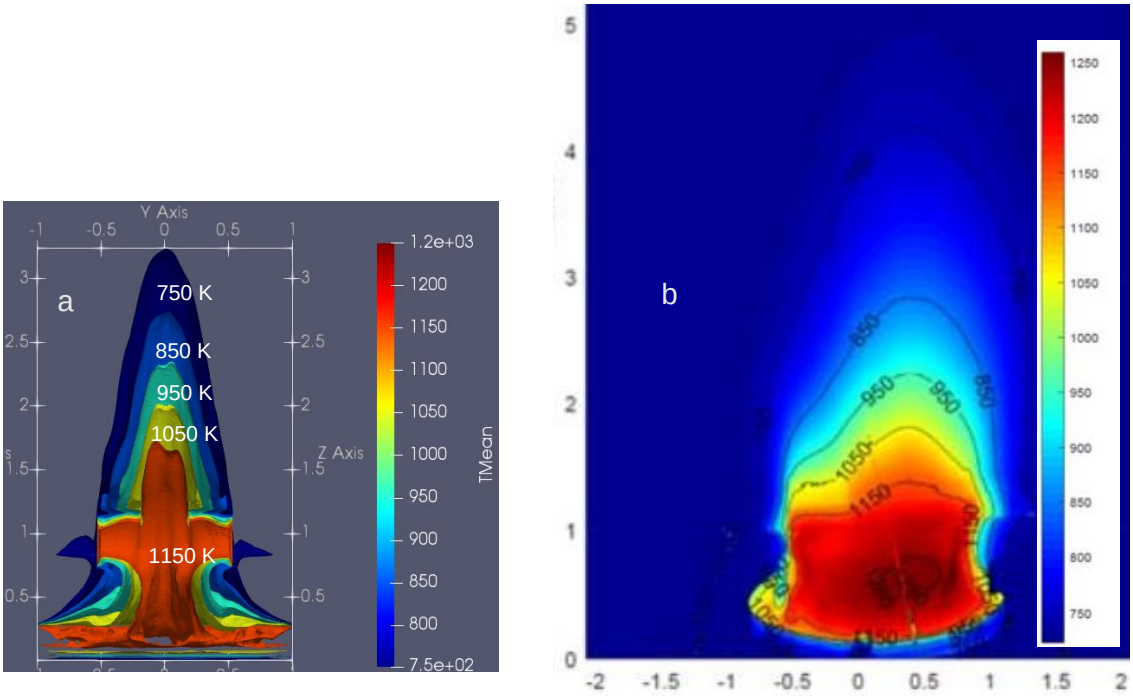

Figure 125. Temperature contours: a) Numerical, b) Experimental

5.5.9.2 FDS

Shown in Figure 126 are the temperature contours at the middle of the domain. The flame temperature ranges from 610-1200 °C. Shown in Figure 127 are the temperature contours on the bottom surface of the calorimeter, which indicates higher temperatures compared to the top surface and the sides. The temperature range is 500-933 °C.

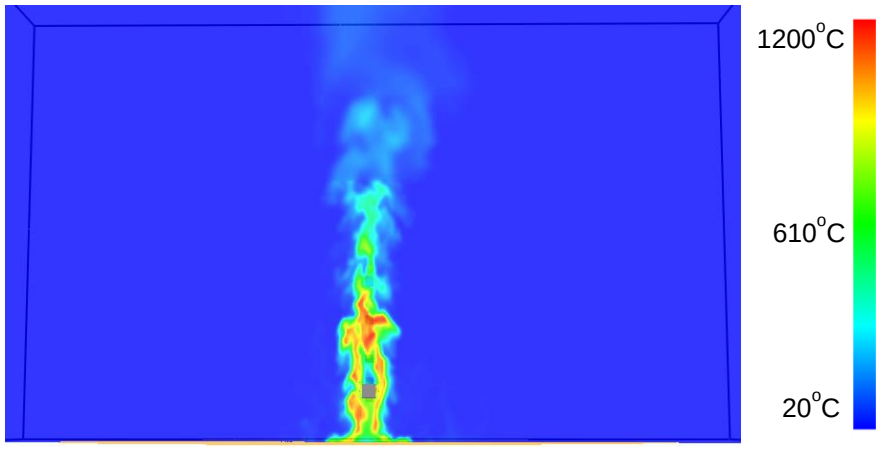

Figure 126. Temperature (°C) slice across the central plane of the flame in the simulations of dilbit pool fire with calorimeter

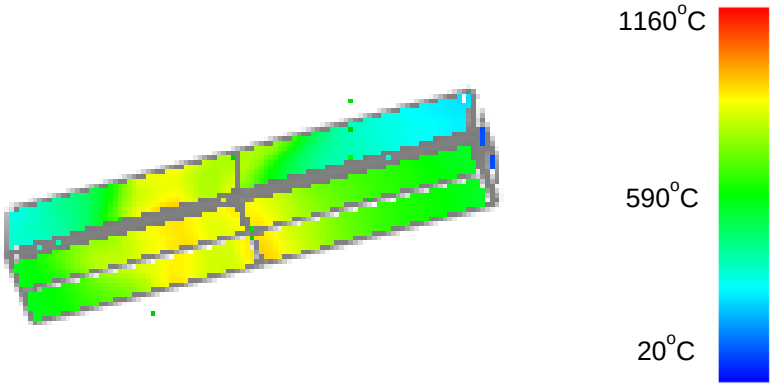

Figure 127. Temperature distribution on the calorimeter surface from dilbit pool fire simulation

5.5.10 Radiation Contours and SEP

5.5.10.1 OpenFOAM

Shown in Figure 128a are the radiative heat flux contours from the numerical simulation. Shown in Figure 128b are the SEP contours from the experiment [2]. It is important to note that the radiative contours are not equivalent to the SEP contours; the radiative contours represent the radiation field iso-surfaces around the flame. The SEP is the projected radiation on a single point in the field of view of the IR camera that is sensitive only to medium wave lengths of 3-5 micrometers located at a distance from the flame. Nonetheless, both have the same values for qualitative comparison. The presence of the calorimeter seems to have distorted the numerical and experimental contours in the same manner (see results of radiation contours and SEP in Section 5.6.7, Figure 145 in comparison with Figure 128)

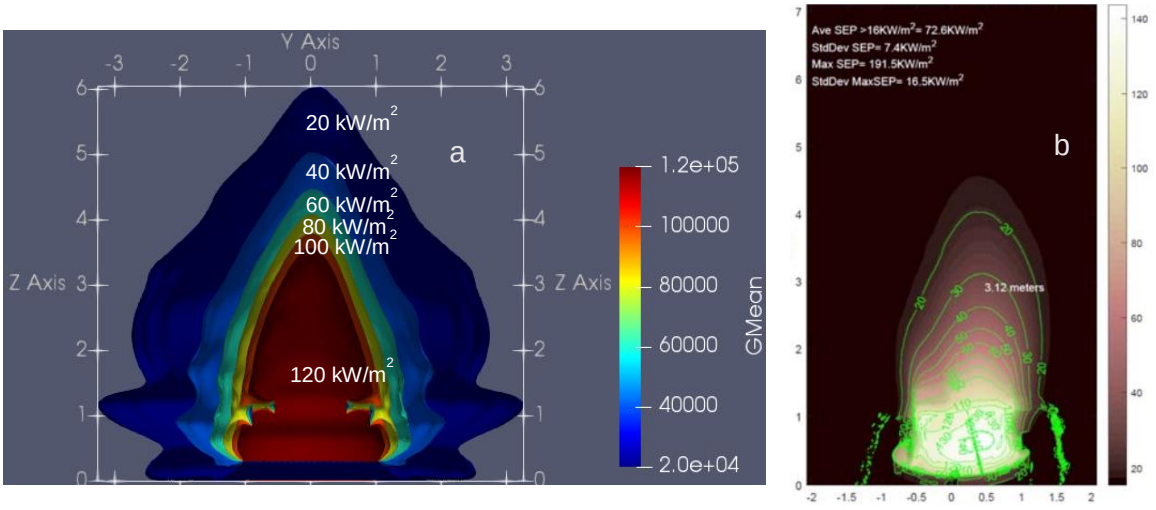

Figure 128. a) Radiative heat flux contours (numerical) b) SEP (experimental)

5.5.11 Wide Angle Heat Flux

5.5.11.1 OpenFOAM

Shown in Figure 129 are the transient wide angle heat fluxes from a) the numerical simulation (time-averaged), b) the experiment [2] and c) the numerical simulation (actual values). Shown in Figure 130 are the steady state values at different heights: a) heat flux versus height and b) height versus heat flux [38]. The two experimental lines are from the same experiment but different time periods where fire parameters were different [38]. The numerical model overestimated the wide angle heat flux at all data points. As mentioned before, the main reason is the different distances at which the heat flux meters are located in the experiment (9 m) and the simulation (6 m).

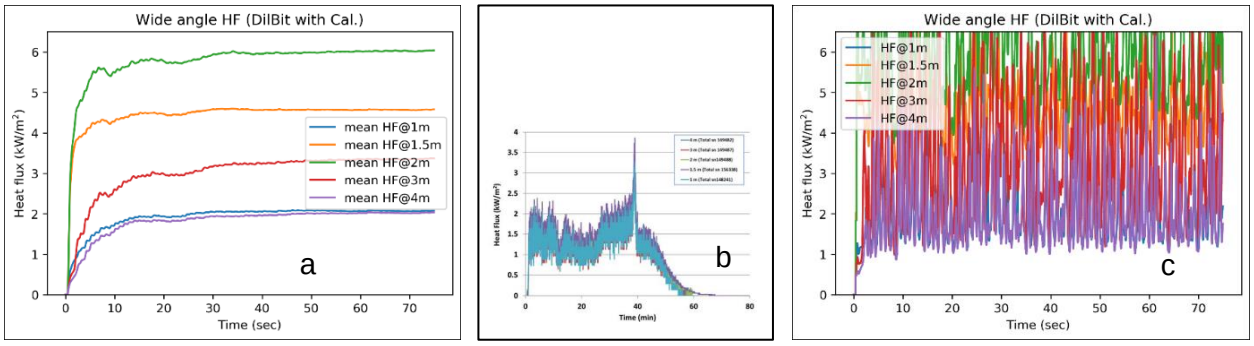

Figure 129. Wide angle heat fluxes of dilbit with calorimeter: a) Numerical, time-averaged, b) Experimental, c) Numerical.

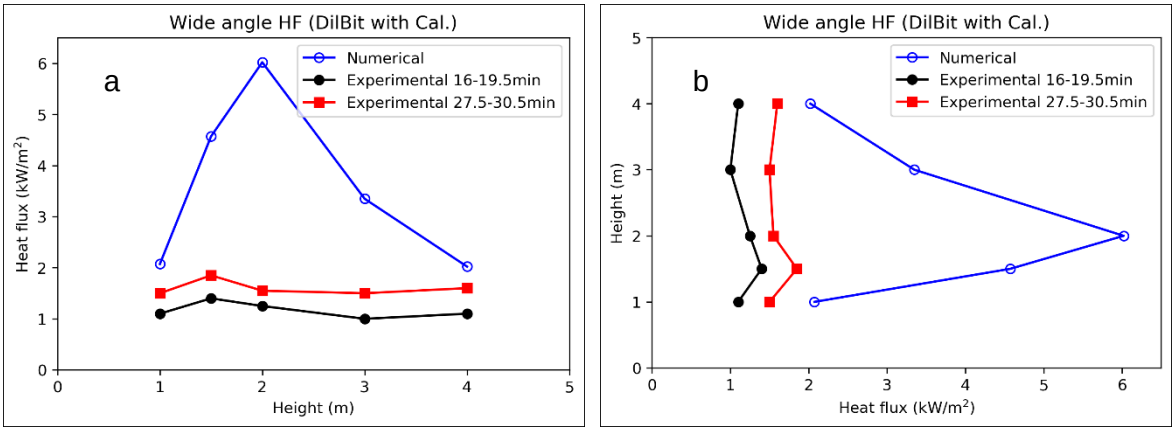

Figure 130. Average wide angle heat fluxes at different heights a) Flux vs. Height b) Height vs. Flux.

Also, experimentally, the wide angle heat flux is measured using a total heat flux gauge with a 180° view angle, which might have different sensitivity to different wave lengths. In the numerical model, all wavelengths are considered using the WSGG radiation model.

5.5.11.2 FDS

The wide angle radiometer readings from the simulation and experiment are compared in Figure 131. The simulation well-predicted the experimental results. The numerical range is 1-1.8 kW/m^2 while the experimental one is 1-2 kW/m^2. The average wide angle heat fluxes from the simulation and experiment are shown in Figure 132. Two sets of experimental data are

presented; average of 16-19.5 min and 27.5-30.5 min. Similar to the average flame temperature; better agreement can be seen between the numerical average heat flux and the experimental average during 27.5-30.5 min.

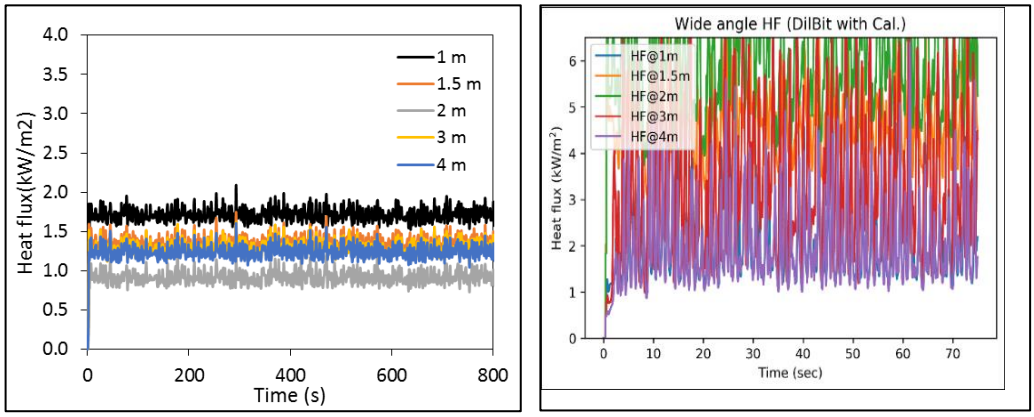

Figure 131. Wide angle radiometer readings for dilbit pool fire simulation (left) and experiment (right) with calorimeter

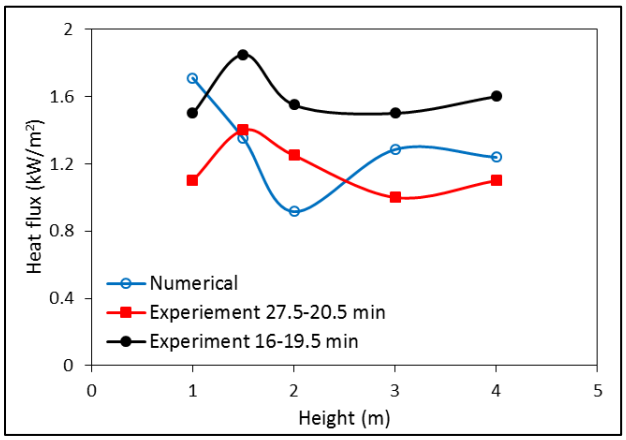

Figure 132. Average wide angle heat fluxes at different heights for dilbit with calorimeter pool fire from FDS simulations

5.5.12 Narrow Angle Heat Flux

5.5.12.1 OpenFOAM

Shown in Figure 133 are the transient narrow angle heat fluxes from a) the numerical simulation (time-averaged), b) the experiment [2] and c) the numerical simulation (actual values). Shown in Figure 134 are the steady state values at different heights: a) heat flux versus height and b) height versus heat flux [38]. The two experimental lines are from the same experiment but different time periods where fire behaviour was different [38]. Both numerical and experimental results have the same profile. However, the numerical model seems to be shifted upwards, overestimating the narrow angle heat flux values at all data points. The reason for that is the different methods used to calculate the heat flux (numerically) and measure the heat flux (experimentally); numerically, the narrow angle heat flux is estimated by sampling the radiation

field close to the flame (i.e. at a distance of 1.1 m from the pool center). In the numerical model, all wavelengths are considered using the WSGG radiation model. Experimentally, a 5.5° view angle radiometer with a zinc selenide window was used. The zinc selenide window has 70% transmissivity in the wavelength range 2-20 μm and zero transmissivity outside this range. That explains the lower narrow angle heat fluxes from the experimental results.

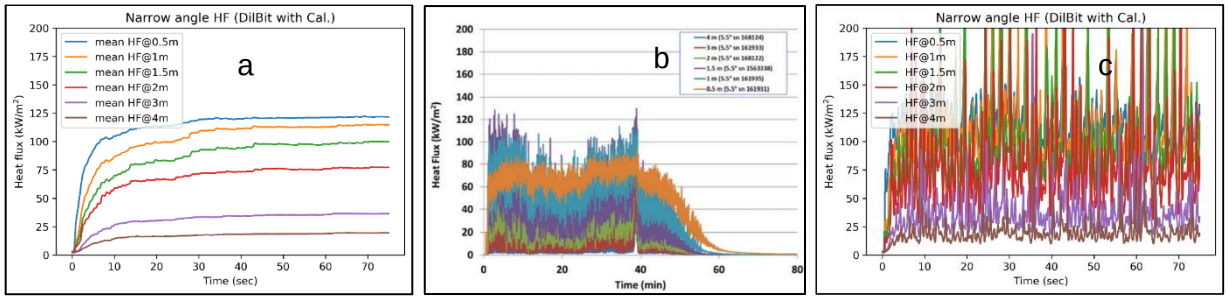

Figure 133. Narrow angle heat fluxes of dilbit with calorimeter: a) Numerical, time-averaged, b) Experimental. c) Numerical.

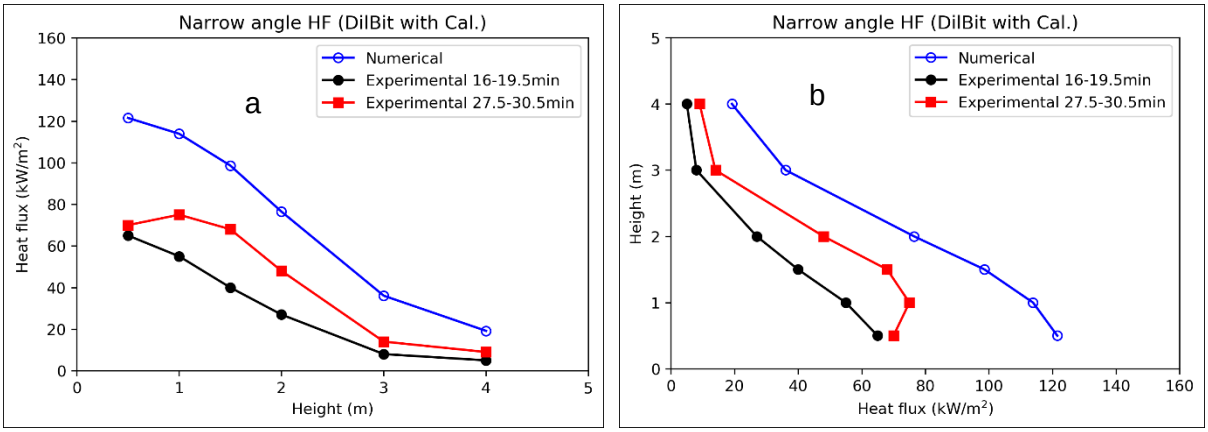

Figure 134. Average narrow angle heat fluxes at different heights a) Flux vs. Height b) Height vs. Flux.

5.5.13 Flame Height

5.5.13.1 OpenFOAM

Shown in Figure 135 is the flame height from a) the numerical simulation and b) the experiment [2]. The numerical model underestimated the flame height. The reason is the different criteria used to define the flame height; numerically the flame height is defined by the highest point, in the domain, at which there is a nonzero value of the fuel concentration. Experimentally, the flame height is obtain used an IR camera which might have been affected by the radiation from soot particles at an elevated temperature. Given the fact that soot and high temperatures would coincide downstream from the fuel, it's expected that the numerical flame height is always lower than the flame height measured experimentally.

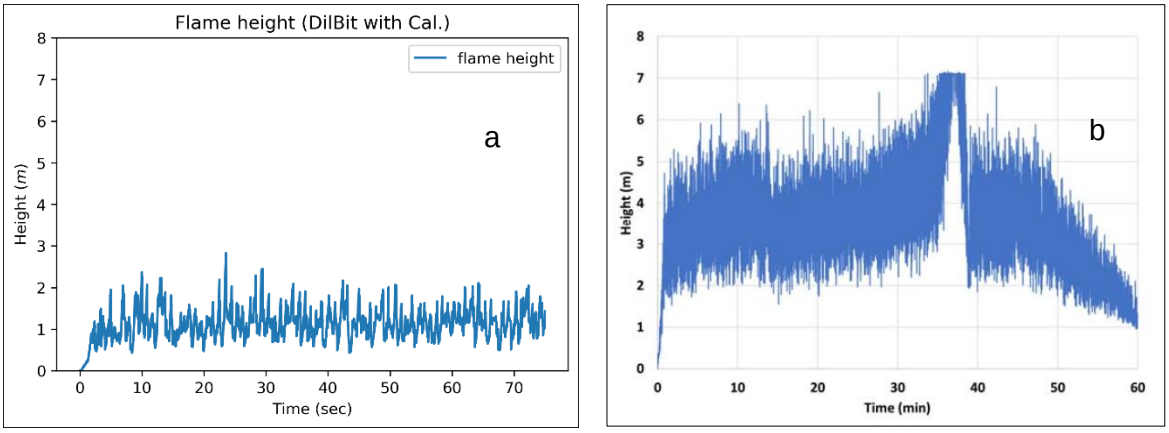

Figure 135. Flame height of dilbit with calorimeter: a) Numerical, b) Experimental.

5.6 Dilbit without Calorimeter

5.6.1 OpenFOAM Results Summary

Discussed in this section are the validation results for the “dilbit without calorimeter” case. Numerical results are compared to experimental results from the NRC experiment at Sandia National Laboratories (Test 3.1) [2]. Summary of the numerical and experimental ranges are shown in Table 23.

Table 23. Results summary for the dilbit without calorimeter simulation from OpenFOAM

Section	Validation parameter	Numerical range	Experimental range	Comments
5.6.3	Centerline temperature	193 – 696°C	90 – 575 °C	Good agreement given propagated experimental uncertainty (i.e. burning rate)
5.6.4	Radiative fraction	43%	60 %	Good agreement given experimental uncertainty
5.6.5	HRR	3.1 MW	2.31 MW – 3.7 MW *	Good agreement
5.6.4	Soot yield	27.7 %	Not reported	
5.6.6	Temperature contours	750 – 1150 K	750 - 1150 K	
5.6.8	Wide angle HF	2.1 – 5.2 kW/m^2	1.2 – 2.4 kW/m^2	Overestimated
5.6.9	Narrow angle HF	20 – 100 kW/m^2	5 – 120 kW/m^2	Overestimated
5.6.10	Flame height	1.17 m	3.4 m	Different criteria

* lower limit from NRC-Sandia report [2]. Upper limit for NRC analysis report [38]

5.6.2 FDS Results Summary

The results from simulating the dilbit pool fire without the calorimeter are compared against the experimental results from Test 3.3. An average burning rate was used.

The results from FDS simulations are summarized in Table 24. It can be seen that, there is a large difference between the numerical and experimental radiative fractions. Experimentally, the radiative fraction was calculated form the estimated HRR and the convective portion of the HRR that is estimated from the exhaust gases temperature and exhaust flow rate. The discrepancy between the numerical and experimental radiative fraction might be attributed to the experimental uncertainty in measuring the HRR and the convective part of the fire. Given the fact that this calculation was done for one experiment only and the large uncertainty in the dilbit HRR value, there is large degree of uncertainty in the 60% radiative fraction value. Also, it is important to note the maximum possible radiative fraction estimated empirically by De Ris [37] is ~ 43% (see Figure 114).

Table 24. Results summary for dilbit without calorimeter simulation from FDS

Section	Validation parameter	Numerical range	Experimental range	Comments
5.6.3	Centerline temperature	210 – 677 °C	90 – 575°C	Good agreement given propagated experimental uncertainty (i.e. burning rate)
5.6.4	Radiative fraction	39%	60 %	Underpredicted
5.6.5	HRR	2.37 MW	2.31 MW – 3.7 MW *	Good agreement
5.6.8	Wide angle HF	1 – 3 kW/m^2	1.2 – 3 kW/m^2	Good agreement
NA	Flame height	4 m	3.4 m	

5.6.3 Plume Centerline Temperature

5.6.3.1 OpenFOAM

Shown in Figure 136 are the transient centerline temperatures from (a) the numerical simulations and (b) the experiment [2]. Shown in Figure 137 are the steady state centerline temperatures: a) temperature versus height and b) height versus temperature [38]. The two experimental lines are from the same experiment but with different time periods where fire parameters were different [38]. There is good agreement between the numerical and experimental results in terms of temperature profile. However, the numerical data points are consistently shifted by ~120°C. The reason might be attributed to a difference between the input flow rate in the numerical model and the actual burning rate in the experiment at which the steady values are obtained. The numerical input flow rate was taken as the mean value between 2.73 kg/min and 3.23 kg/min (see Section 6.3.3.3 in the Sandia report).

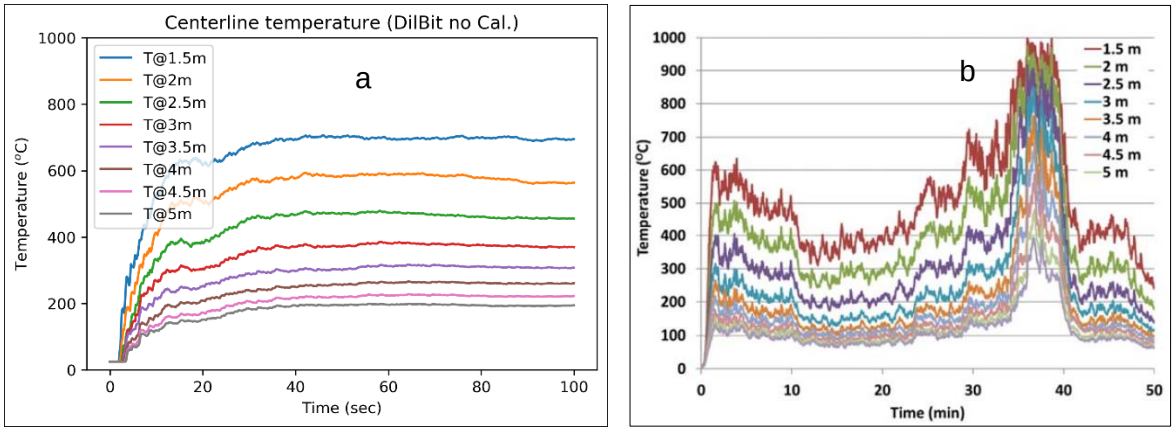

Figure 136. Centerline temperatures at different heights (dilbit without calorimeter): a) Numerical, b) Experimental.

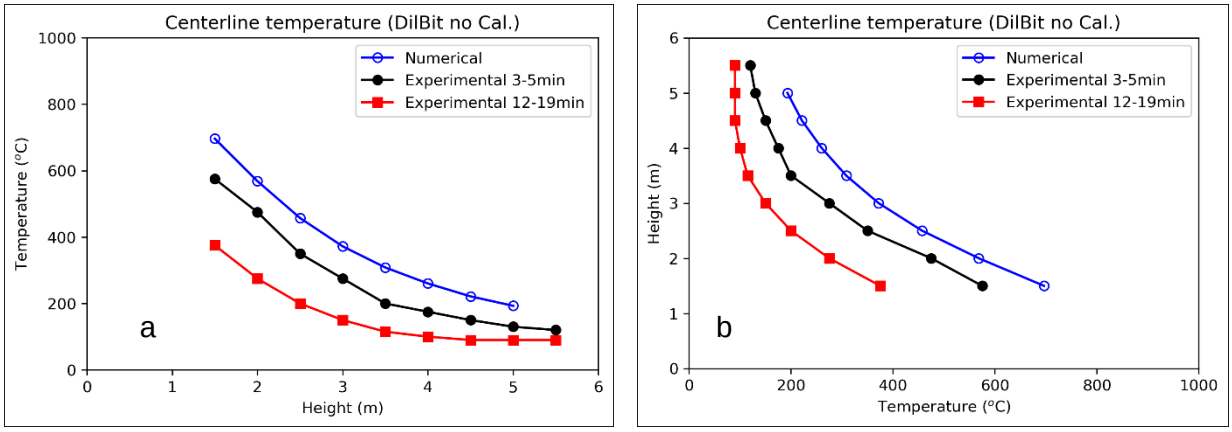

Figure 137. Average centerline temperatures at different heights a) Temp. vs. Height b) Height vs. Temp.

5.6.3.2 FDS

The experimental and numerical centerline temperatures are shown in Figure 138. Two sets of experimental averages from the same test are shown: one during the time period from 3 to 5 min and the second on is from 12 to 19 min. The two durations corresponds to two semi steady intervals of dilbit burning rate/HRR. The temperatures are overpredicted by the simulations. This might be due to a constant mass flux (burning rate) imposed in the numerical simulations, while the actual burning rate in the experiments is transient (i.e. decreasing with time). The numerical temperature range is 210 – 677 °C and the experimental range across the whole experimental duration is 90 – 575 °C.

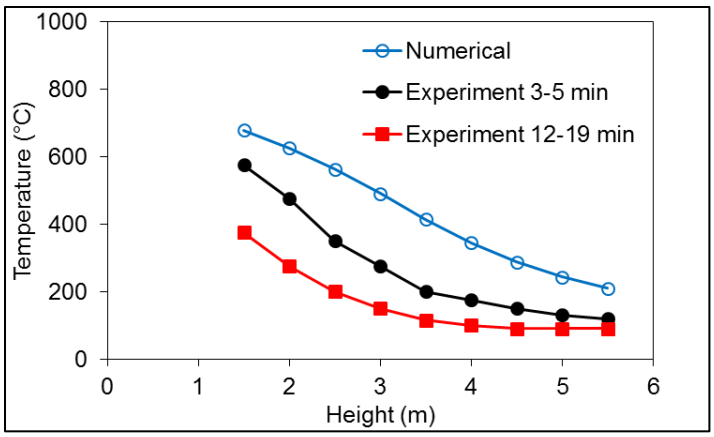

Figure 138. Average flame temperature at the centerline of the pool for dilbit pool fire without the calorimeter from the simulation and experiment

5.6.4 Radiative Fraction & Soot Yield

5.6.4.1 OpenFOAM

Shown in Figure 139 is the radiative heat fraction and the soot yield from the numerical simulation. Numerical radiative heat fraction was ~ 43%. Experimental radiative heat fraction was 60% (see Figure 24b) (i.e. based on the measured HRR with significant uncertainty in the measurements). Please see the discussion in Section 5.5.5 for the explanation of the discrepancy between the two values.

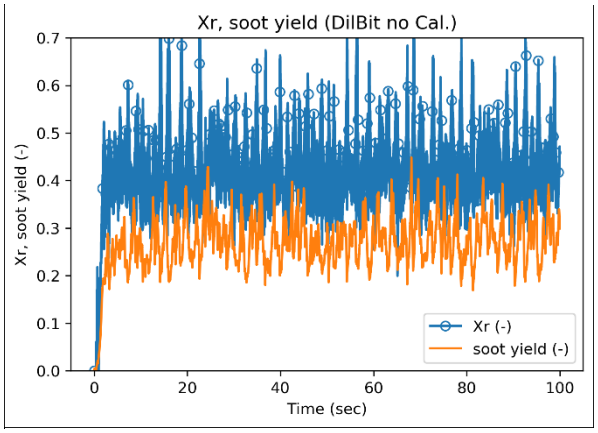

Figure 139. Numerical radiative fraction and soot yield results.

5.6.4.2 FDS

The numerical radiative fraction from FDS simulations for the dilbit without calorimeter case is shown in Figure 140. The average numerical X_r is 39%, while the experimental value is 60%.

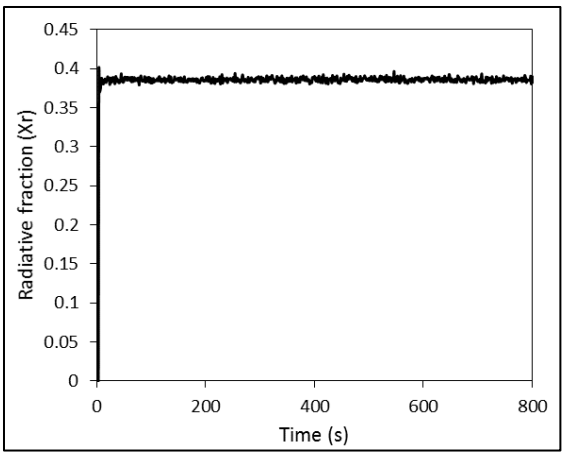

Figure 140. Numerical radiative fraction for dilbit without calorimeter from FDS simulation.

5.6.5 Heat Release Rate (HRR)

5.6.5.1 OpenFOAM

Shown in Figure 141 are the HRR, radiative heat release and heat release due to soot oxidation from the numerical simulation. Numerical, the HRR was ~3.1 MW. Experimentally, two values of HRR were reported: 2.3 MW estimated from the burning rate (test 3.3) and 3.7 MW calculated from data collected using the gas analyzer from a different test (test 3.4, the only test where gas analyzer data was collected) [2], [38].

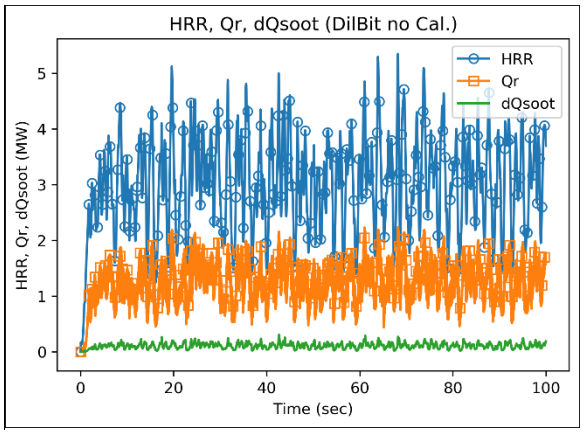

Figure 141. Time series results of heat release rate, radiative heat flux, soot radiative flux.

5.6.5.2 FDS

The numerical HRR for the dilbit pool fire without calorimeter is presented in Figure 142. The numerical average HRR is 2.37 MW while the experimental value is 2.3 +/- 0.2 MW.

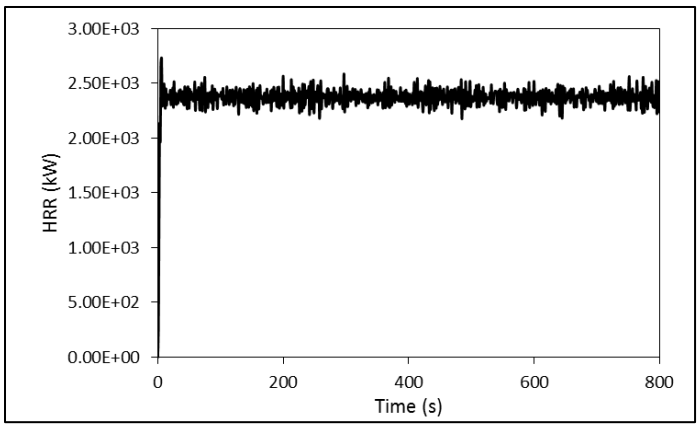

Figure 142. Numerical HRR for dilbit without calorimeter pool fire in FDS

5.6.6 Temperature Contours

5.6.6.1 OpenFOAM

Shown in Figure 143 are the temperature contours from a) the numerical simulation and b) the experiment [2]. The plotted contours are for temperatures values 750, 850, 950, 1050 and 1150 K. There is a mismatch between numerical and experimental contours in terms of shape. The IR camera seem to have been angled differently in this experiments given that the projection of the pan is visible in the experimental picture.

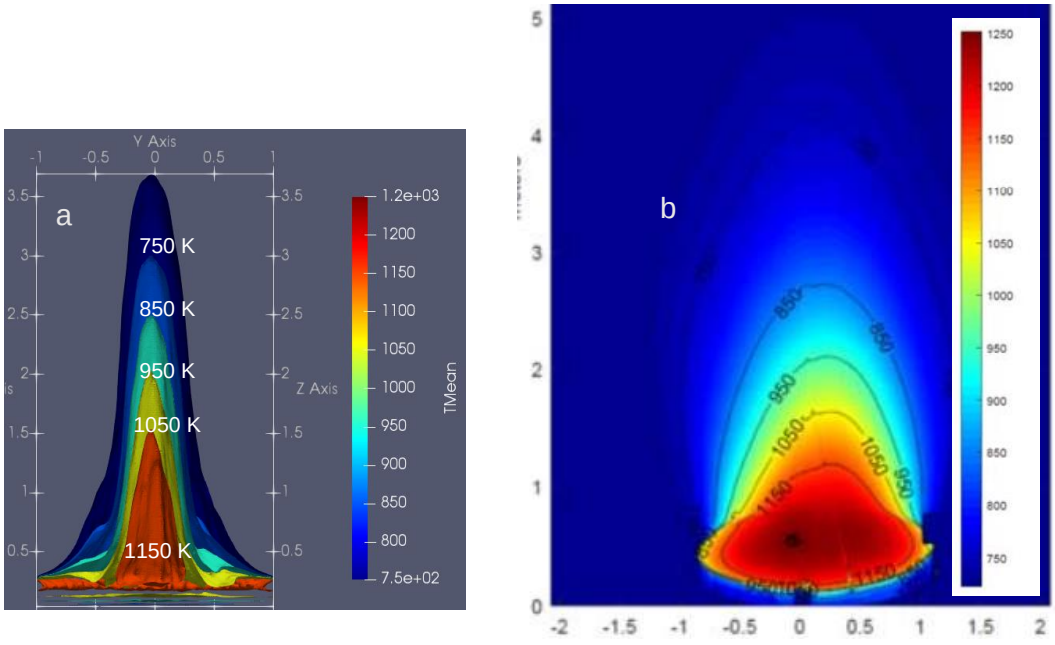

Figure 143. Temperature contours: a) Numerical, b) Experimental

5.6.6.2 FDS

The temperature contour at the middle cross section of the domain is shown in Figure 144. The temperature within the flame zone ranges from 610 °C to 1100 °C.

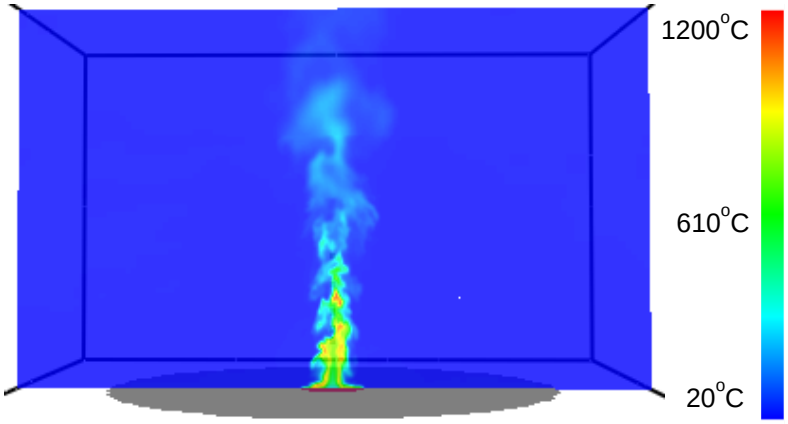

Figure 144. Temperature (°C) slice across the central plane of the flame in the simulations of dilbit pool fire without calorimeter

5.6.7 Radiation Contours and SEP

5.6.7.1 OpenFOAM

Shown in Figure 145a are the radiative heat flux contours from the numerical simulation. Shown in Figure 145b are the SEP contours from the experiment [2]. It is important to note that the radiative contours are not equivalent to the SEP contours; the radiative contours represent the radiation field iso-surfaces around the flame. The SEP is the projected radiation on a single point in the field of view of the IR camera that is sensitive only to medium wave lengths of 3-5 micrometer located at a distance from the flame. Nonetheless, both have the same values for qualitative comparison.

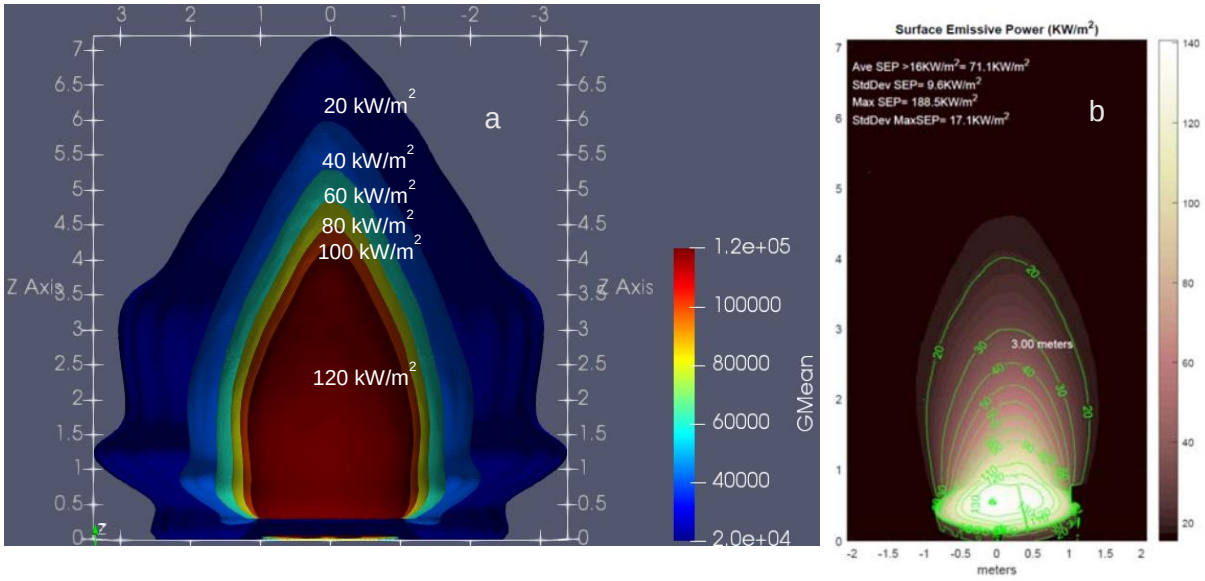

Figure 145. a) Radiative heat flux contours (numerical) b) SEP (experimental)

5.6.8 Wide Angle Heat Flux

5.6.8.1 OpenFOAM

Shown in Figure 146 are the transient wide angle heat fluxes from a) the numerical simulation (time-averaged), b) the experiment [2] and c) the numerical simulation (actual values). Shown in Figure 147 are the steady state values at different heights: a) heat flux versus height and b) height versus heat flux [38]. The two experimental lines are from the same experiment but different time periods where fire parameters were different [38]. The numerical model overestimated the wide angle heat flux at all data points. The same reason was mentioned before but repeated here for completeness. The main reason is the different distances at which the heat flux meters are located in the experiment (9 m) and the simulation (6 m). The intensity of heat flux decreases as the distance from the fire to the target increases (i.e. the decrease is proportional to the square root of the distance).

Also, experimentally, the wide angle heat flux is measured using a total heat flux gauge with a 180^o view angle, which might have different sensitivity to different wave lengths. In the numerical model, all wavelengths are considered using the WSGG radiation model.

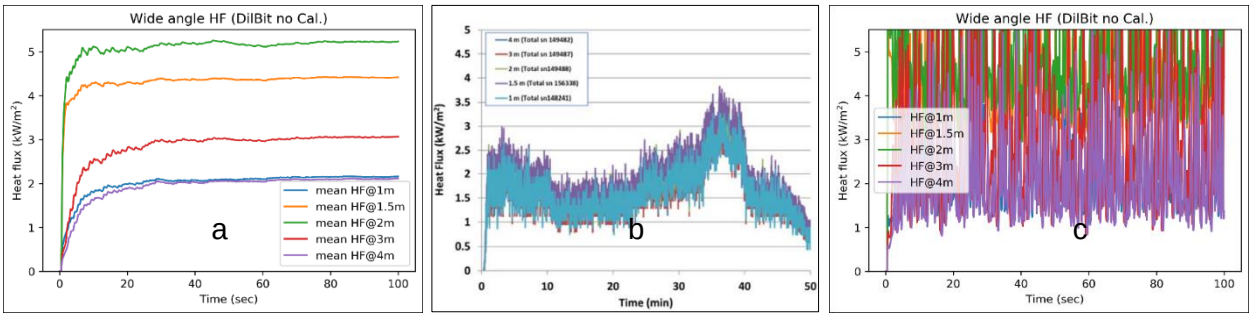

Figure 146. Wide angle heat fluxes of dilbit without calorimeter: a) Numerical, time-averaged. b) Experimental. c) Numerical.

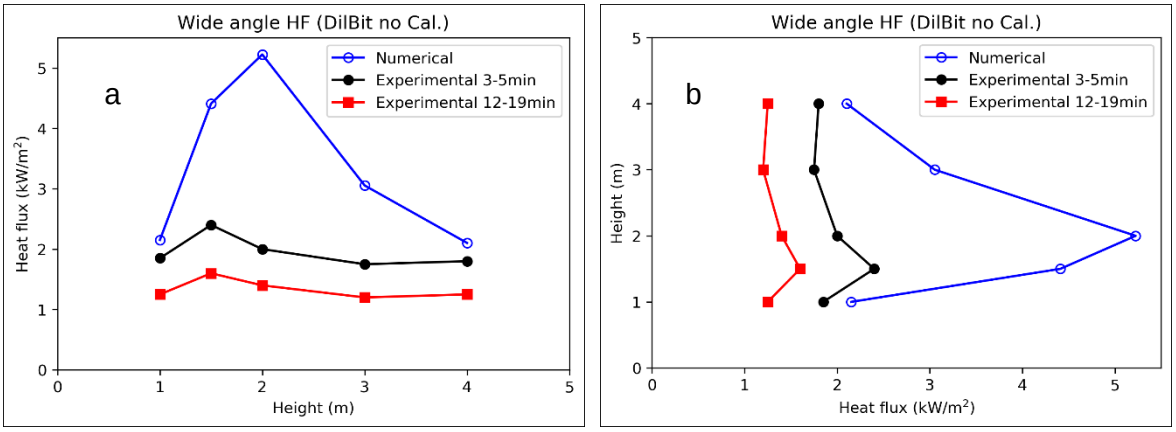

Figure 147. Average wide angle heat fluxes at different heights: a) Flux vs. Height b) Height vs. Flux.

5.6.8.2 FDS

The wide angle radiometer readings are presented in Figure 148. The numerical and experimental ranges are in good agreement (neglecting the unsteady rise in heat flux near the end of the experiment). The numerical and experimental range is 1-3 kW/m^2. It should be noted

that, the numerical heat flux is constant during the whole duration due to the constant burning rate specified in the simulation. However, the burning rate was fluctuating during the dilbit experiment due to its complex chemistry, which resulted in fluctuating experimental heat fluxes. The average wide angle heat fluxes from the simulation and experiment are shown in Figure 149. Two sets of experimental data are presented; average of 3-5 min and 12-19 min.

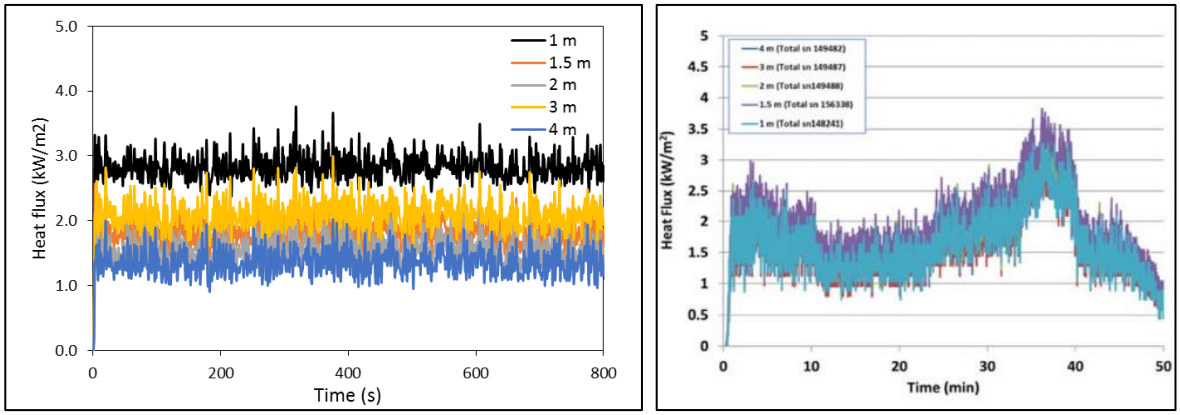

Figure 148. Wide angle radiometer readings for dilbit pool fire without calorimeter from simulations (left panel) and experiments (right panel)

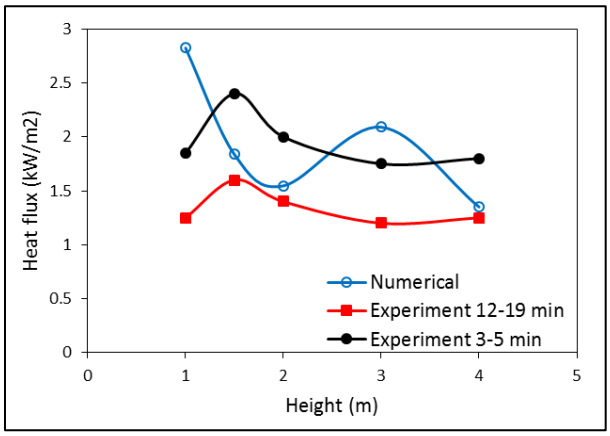

Figure 149. Average wide angle heat fluxes at different heights for dilbit without calorimeter pool fire from FDS simulations

5.6.9 Narrow Angle Heat Flux

5.6.9.1 OpenFOAM

Shown in Figure 150 are the transient narrow angle heat fluxes from a) the numerical simulation (time-averaged), b) the experiment [2] and c) the numerical simulation (actual values). Shown in Figure 151 are the steady state values at different heights: a) heat flux versus height and b) height versus heat flux [38]. The two experimental lines are from the same experiment but different time periods where fire parameters were different [38]. Both numerical and experimental results have the same profile. However, the numerical model seems to be shifted upwards, overestimating the narrow angle heat flux values at all data points. Having the

numerical plot closer to the experimental plot with the higher values might have been coincidental given that numerical narrow angle heat flux has been consistently higher than the experimental value for previous Bakken and dilbit cases. The reason has been discussed in previous sections, however, repeated here for completeness: numerically, the narrow angle heat flux is estimated by sampling the radiation field close to the flame (i.e. at a distance of 1.1 m from the pool center). In the numerical model, all wavelengths are considered using the WSGG radiation model. Experimentally, a 5.5˚ view angle radiometer with a zinc selenide window was used. The zinc selenide window has 70% transmissivity in the wavelength range 2-20 μm and zero transmissivity outside this range. That explains the lower narrow angle heat fluxes from the experimental results. It should be also noted that the surface emissive power measured by the IR camera was about 10% higher than the narrow angle radiometers.

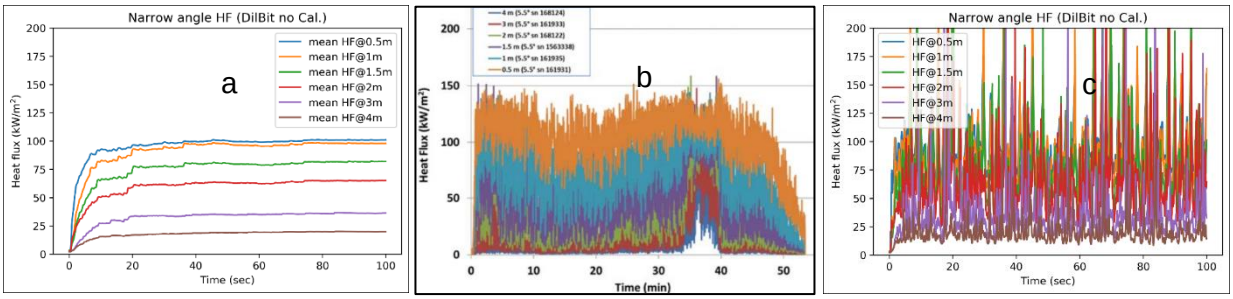

Figure 150. Narrow angle heat fluxes of dilbit without calorimeter: a) Numerical, b) Experimental, c) Numerical, time-averaged.

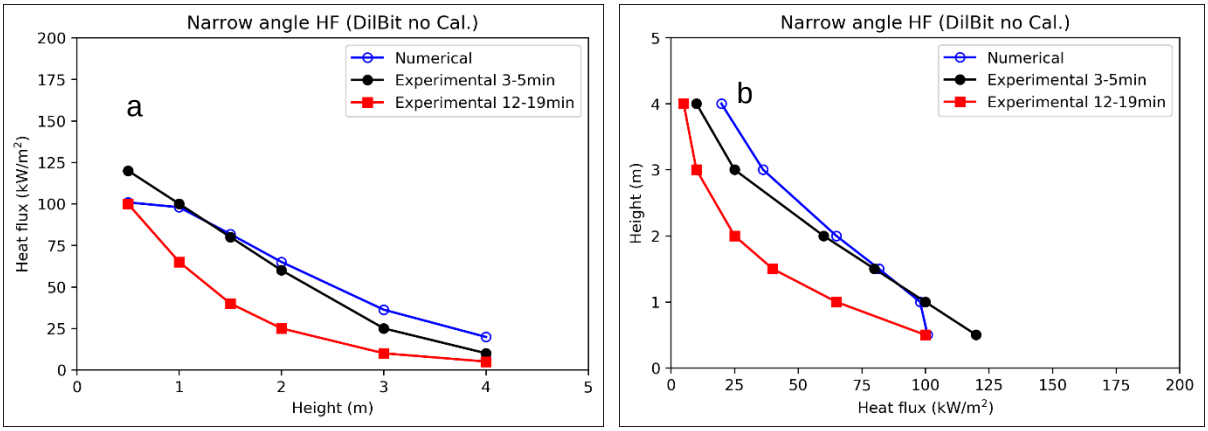

Figure 151. Average narrow angle heat fluxes at different heights: a) Flux vs. Height b) Height vs. Flux.

5.6.10 **Flame Height**

5.6.10.1 OpenFOAM

Shown in Figure 152 is the flame height from a) the numerical simulation and b) the experiment [2]. The numerical model underestimated the flame height. The reason has been discussed in previous section, however, repeated here for completeness; numerically, the flame height is defined by the highest point, in the domain, at which there is a nonzero value of the fuel concentration. Experimentally, the flame height was obtained using used an IR camera which

might have been affected by the radiation from soot particles at an elevated temperature. Given the fact that soot and high temperatures would coincide downstream from the fuel, it's expected that the numerical flame height is always lower than the flame height measured experimentally. In fact, turbulent diffusion flames fluctuate with time by their nature, and the flame height is defined as the height of 50% intermittency of a visible flame.

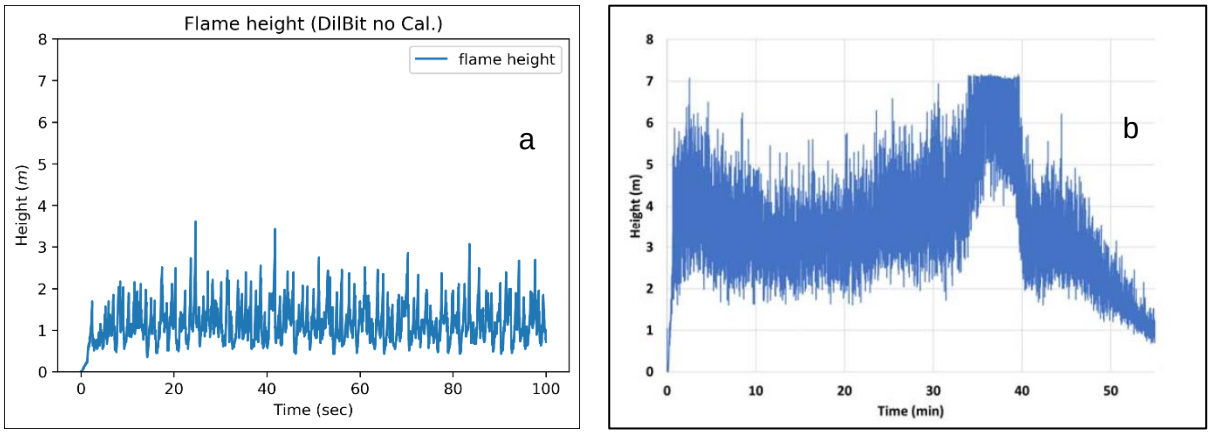

Figure 152. Flame height of dilbit without calorimeter: a) Numerical, b) Experimental.

6 Comparison between OpenFOAM and FDS

Both FDS and OpenFOAM solve the same governing equations and use the same input parameters (boundary conditions). The fundamental difference between FDS and OpenFOAM is the method used to solve these equations. In FDS, the finite difference method is used, while in OpenFOAM, the finite volume method is used. Using the finite difference method requires a rectilinear mesh structure with perfectly orthogonal mesh lines. That restriction dictates that objects in the domain should be rectangular which is perfect for compartment fires. However, any curved shape should be approximated using a "stair-step" like mesh, which results in slower simulation, potential numerical instability and altered flow field around the object. FDS is not fully flexible in using different mesh sizes in the domain. Also, Adaptive Mesh Refinement (AMR) is not possible in FDS. Despite these disadvantages, the finite difference method is faster and forces an excellent mesh quality.

Because the finite volume method is used in OpenFOAM, curved geometries are easily modeled and meshed. There is more flexibility to use different mesh sizes in the domain. That has proven very useful in this study where a cylindrical calorimeter with thin baffles and a pan rim had to be included in the domain. Although the version of OpenFOAM used in this work didn't include the option of AMR, this option is available in newer versions of OpenFOAM and might be considered in future work to shorten simulations time.

The ability to model curved shapes in OpenFOAM resulted in better agreement with experimental results related to the calorimeter: calorimeter heat flux, calorimeter temperatures and calorimeter surrounding temperatures.

FDS developers have taken an extra step to model experimental instruments as “devices” in the numerical domain. Users can specify some properties for thermocouples and heat flux gauges and FDS can calculate what these devices would measure in reality. However, in OpenFOAM, users have to create these devices in the input files by sampling and conduct mathematical operations on specific fields. That is the reason why FDS wide angle heat flux values were closer to the experimental wide angle heat flux.

In conclusion, the limitations on the shapes that could be modeled in FDS is hard to get around. And models of measuring “devices” in OpenFOAM can be easily refined to better match the output from the experimental instrument.

Another advantage of OpenFOAM over FDS is that the source code is more accessible and easier to modify; the code is broken down to a large number of short scripts and distributed over clearly named directories (folders).

Moving forward, OpenFOAM will be the tool used to model pool fires in this project.

7 Conclusions

7.1 OpenFOAM

Presented in this report are the findings from Stage 2 of the “Numerical Fire Modeling of Crude Oil Spills” project. The objective of this stage was to evaluate the ability of numerical models to predict gas phase parameters from crude oil pool fires. The NRC-Sandia experiments were chosen to compare numerical and experimental results.

A review of gas phase models was conducted. The EDC model was used for combustion. The SPH model was used for soot formation. The WSGG model was used for radiation. In line with the experimental setup, six simulations were conducted: 3 types of fuel (heptane, Bakken and dilbit) and 2 domains: one with a calorimeter representing a tank engulfed in fire and another domain that did not include a calorimeter.

Eleven parameters were selected to gauge the capabilities of the numerical model to predict fire behaviour. Important parameters in term of relevance to the goals of this project are centerline temperature, calorimeter temperature, calorimeter surrounding temperature, calorimeter heat flux, radiation fraction and HRR.

For heptane, there were some discrepancies between the numerical and experimental results that are attributed to boiling of heptane which hasn’t been considered in the numerical model. A better agreement from a numerical model where the fuel pan is removed from the domain supports that theory.

For Bakken and dilbit there is good agreement between numerical and experimental results especially when comparing the important parameters mentioned above. Any discrepancy could be explained by considering experimental uncertainties, absence of thermal mass of the calorimeter from the numerical model, absence of small physical details from the numerical model or propagated uncertainties of input parameters (such as the uncertainty in burning rate

in case of dilbit). High resolution details are further obtained from the numerical model for the calorimeter temperature distribution and calorimeter heat flux.

Simulated measurements of the wide angle heat flux, narrow angle heat flux, temperature contours and flame height exhibited a larger deviation from the experimental results. The main reason is attributed to a less accurate model of the measuring devices, in the numerical domain.

The wide range of data points and parameters used to validate the numerical models and the general agreement with experimental results, provide good confidence in the ability of the numerical model to predict important parameters affecting a tank car subjected to a crude oil pool / spill fire.

7.2 FDS

A model for simulating crude oil fires was developed in Fire Dynamics Simulator (FDS). Similar to OpenFOAM, 6 simulations were conducted for 3 fuels; heptane, and Bakken and dilbit crude oils; in 2 different domains; with and without calorimeter. The model was validated against the experiments conducted by NRC at Sandia National Laboratory. Eight parameters were considered for the validation; centerline (plume) temperature, exterior to calorimeter temperature, radiative fraction, heat flux to calorimeter, heat release rate (HRR), temperature contours, wide angle HF and flame height. Generally, the results for centerline temperature, HRR, flame height, wide angle HF from the simulations are in satisfactory agreement with the experimental data. However, the temperatures surrounding the calorimeter and on its surface were greatly underestimated by the model. This might be attributed to the cuboid geometry of the calorimeter and the absence of baffles in the simulations. Also, the radiative fraction was underpredicted for Bakken and dilbit, this might be due to the experimental uncertainty.

In addition to the limited ability of FDS to simulate curved structures due to its rectilinear mesh, FDS couldn’t replicate the narrow angle HF, flame temperature contours and SEP.

8 Summary

Given the validation results in this report, the numerical model developed has proven to be successful in predicting the most relevant fire conditions encompassing the calorimeter and could be extrapolated to simulate large scale fire scenarios as well as various locations/orientations of a rail tank car with respect to the pool fire. Results from such simulations should be used as thermal boundary conditions for modeling the crude oil behaviour inside the tank and its structural integrity.

During the process of developing and validating a numerical model for crude oil pool fires, there are lessons learned, some of which are not explicitly discussed in the report. For example, thermal boundary conditions, such as temperature distribution around the calorimeter and radiative heat flux, are very sensitive to the burning rate of crude oil. This is evident from the different burning rates used to model heptane, Bakken and dilbit and the results of temperature distribution and radiative heat flux from each fuel. Another unexpected finding is that soot yield didn’t always correlate to an increased radiation fraction. For example, despite the increase in

soot yield from the dilbit fire (27%, numerical) compared to Bakken (15%, numerical), the radiation fraction from both Bakken and dilbit fires, from the “with calorimeter” cases, was approximately the same (44%). Also, some geometrical details could make a big difference in the results. For example, adding baffles to the calorimeter resulted in better agreement between the numerical and experimental results. Another important lesson learned is the trade-off between the benefit of adding more details to a model and the time and resources needed in preprocessing, running the simulations and post processing the results. Generally, a numerical model is as accurate as the details included in the domain, mesh, and sub models. However, some details are overwhelmingly complicated and could be unreasonable to be included in the numerical model. For example, including very small and many geometrical details could be counterproductive and might result in a low mesh quality. Also, accounting for the effect of detailed chemistry of the crude oil and its composition is time consuming and requires a lot more computational resources. A better approach is to model the equivalent effect of a crude oil chemical composition using surrogates and equivalent burning characteristics.

It is evident that the gas phase results are very much dependant on the burning rate of the fuel in question. Hence, if further work were to be conducted, the key recommendation would be to develop and validate a pyrolysis model for Bakken and dilbit crude oils to predict their burning rate and soot yield. These models would enable simulating crude oil fire scenarios that are similar to actual fire incidents. Development of the pyrolysis models should be conducted in a chemically controlled environment using a thermogravimetric analyzer or a micro cone calorimeter. Pyrolysis models should be tested by simulating a small scale experiment such as the cone calorimeter where fire parameters can be controlled and accurately measured. Also, gas analysis techniques, such as FTIR, and soot measurements should be collected and compared to numerical predictions.

Acknowledgment

This project was funded by Transport Canada. Their support is gratefully acknowledged. The authors would like to thank Michael Spiess and Rachel Domaratzki for their contribution in reviewing the report.

The authors would like to thank Professor Jennifer Wen, University of Warwick, UK, for sharing the source codes for the EDC combustion model, Soot SPH model and the WSGG radiation model for OpenFOAM.

References

[1] “Sandia National Laboratories: Burn Site.” https://www.sandia.gov/vqsec/facilities/burn-site.html (accessed Mar. 07, 2019).

[2] Y. Ko, C. Lam, E. Gibbs, P. Lafrance, and M. Weinfurter, “Rail Tank Cars Exposed to Fires: Experimental Analyses of Thermal Conditions Imposed to a Railcar Engulfed in Crude Oil Fires (Series 1-3 Tests),” A1-010647, Oct. 2020.

[3] K. McGrattan, S. Hostikka, R. McDermott, J. Floyd, C. Weinschenk, and K. Overholt, “Fire Dynamics Simulator User’s Guide,” NIST, 1019, Jan. 2017.

[4] K. McGrattan, S. Hostikka, R. McDermott, J. Floyd, C. Weinschenk, and K. Overholt, “Fire Dynamics Simulator Technical Reference Guide Volume 1: Mathematical Model,” NIST, 1018-1, Jan. 2017.

[5] C. Greenshields, “OpenFOAM User Guide: CFD Direct, Architects of OpenFOAM,” *CFD Direct*, Mar. 02, 2017. https://cfd.direct/openfoam/user-guide/ (accessed Feb. 26, 2019).

[6] “OpenFOAM | The OpenFOAM Foundation,” *OpenFOAM*. https://openfoam.org/ (accessed Mar. 07, 2019).

[7] C. Greenshields, “OpenFOAM v6 User Guide: 5.4 Meshing with snappyHexMesh,” *CFD Direct*, Jul. 10, 2018. https://cfd.direct/openfoam/user-guide/v6-snappyhexmesh/ (accessed Mar. 07, 2019).

[8] I. Gomaa, N. Elsagan, C. Lam, and Y. Ko, “Evaluation of CFD tools for crude oil fire simulations (modeling steps in openFOAM and FDS) / author(s), Islam Gomaa, Nour Elsagan, Cecilia Lam and Yoon Ko.: NR24-37/2019E-PDF - Government of Canada Publications - Canada.ca,” National Research Council Canada, NR24-37/2019E-PDF, Aug. 2019. Accessed: Sep. 07, 2021. [Online]. Available: https://publications.gc.ca/site/eng/9.870653/publication.html

[9] C. Greenshields, “Programmer’s Guide,” OpenFOAM Foundation Ltd., 3.0.1, Dec. 2015. [Online]. Available: http://foam.sourceforge.net/docs/Guides-a4/ProgrammersGuide.pdf

[10] “ParaView.” https://www.paraview.org/ (accessed Mar. 07, 2019).

[11] G. P. Forney and K. B. McGrattan, *User’s Guide for Smokeview Version4: A Tool for Visualizing Fire Dynamics Simulation Data*. US Department of Commerce, National Institute of Standards and Technology, 2004.

[12] “ANSYS Fluent Theory Guide,” ANSYS Inc., Release 15.0, Nov. 2013.

[13] S. P. Burke and T. E. W. Schumann, “Diffusion Flames,” *INDUSTRIAL AND ENGINEERING CHEMISTRY*, vol. 20, no. 10, p. 7, 1928.

[14] N. Peters, “Laminar diffusion flamelet models in non-premixed turbulent combustion,” *Progress in Energy and Combustion Science*, vol. 10, no. 3, pp. 319–339, Jan. 1984, doi: 10.1016/0360-1285(84)90114-X.

[15] D. Veynante and L. Vervisch, “Turbulent combustion modeling,” *Progress in Energy and Combustion Science*, vol. 28, no. 3, pp. 193–266, Mar. 2002, doi: 10.1016/S0360-1285(01)00017-X.

[16] T. Poinsot and D. Veynante, *Theoretical and Numerical Combustion*. R.T. Edwards, Inc., 2005.

[17] D. B. Spalding, “Mixing and chemical reaction in steady confined turbulent flames,” *Symposium (International) on Combustion*, vol. 13, no. 1, pp. 649–657, Jan. 1971, doi: 10.1016/S0082-0784(71)80067-X.

[18] H. B. Mason and D. B. Spalding, “Prediction of reaction rates in turbulent premixed boundary layer flows,” *Combustion Institute European Symposium*, pp. 601–606, 1973.

[19] M. Bösenhofer, E.-M. Wartha, C. Jordan, and M. Harasek, “The Eddy Dissipation Concept—Analysis of Different Fine Structure Treatments for Classical Combustion,” *Energies*, vol. 11, no. 7, Art. no. 7, Jul. 2018, doi: 10.3390/en11071902.

[20] I. R. GRAN and B. F. MAGNUSSEN, “A Numerical Study of a Bluff-Body Stabilized Diffusion Flame. Part 2. Influence of Combustion Modeling And Finite-Rate Chemistry,” *Combustion Science and Technology*, vol. 119, no. 1–6, pp. 191–217, Oct. 1996, doi: 10.1080/00102209608951999.

[21] B. MAGNUSSEN, “On the structure of turbulence and a generalized eddy dissipation concept for chemical reaction in turbulent flow,” in *19th Aerospace Sciences Meeting*, American Institute of Aeronautics and Astronautics. doi: 10.2514/6.1981-42.

[22] B. F. Magnussen and B. H. Hjertager, “On mathematical modeling of turbulent combustion with special emphasis on soot formation and combustion,” *Symposium (International) on Combustion*, vol. 16, no. 1, pp. 719–729, Jan. 1977, doi: 10.1016/S0082-0784(77)80366-4.

[23] B. F. Magnussen, “THE EDDY DISSIPATION CONCEPT A BRIDGE BETWEEN SCIENCE AND TECHNOLOGY,” presented at the ECCOMAS Thematic Conference on Computational Combustion, Lisbon, Portugal, Jun. 2005.

[24] B. Panjawani, I. S. Ertesvåg, A. Gruber, and K. E. Rian, “Turbulence combustion closure model based on the Eddy dissipation concept for large eddy simulation,” Algarve, Portugal, Aug. 2010, pp. 27–38. doi: 10.2495/AFM100031.

[25] I. S. ERTESVÅG and B. F. MAGNUSSEN, “The Eddy Dissipation Turbulence Energy Cascade Model,” *Combustion Science and Technology*, vol. 159, no. 1, pp. 213–235, Oct. 2000, doi: 10.1080/00102200008935784.

[26] Z. Chen, J. Wen, B. Xu, and S. Dembele, “Large eddy simulation of a medium-scale methanol pool fire using the extended eddy dissipation concept,” *International Journal of Heat and Mass Transfer*, vol. 70, pp. 389–408, Mar. 2014, doi: 10.1016/j.ijheatmasstransfer.2013.11.010.

[27] Z. Chen, J. X. Wen, X. B, and S. Dembele, “Large Eddy Simulation of Fire Dynamics with the Improved Eddy Dissipation Concept,” *Fire Safety Science*, vol. 10, pp. 795–808, 2011.

[28] Z. Chen, J. Wen, B. Xu, and S. Dembele, “Extension of the eddy dissipation concept and smoke point soot model to the LES frame for fire simulations,” *Fire Safety Journal*, vol. 64, pp. 12–26, Feb. 2014, doi: 10.1016/j.firesaf.2014.01.001.

[29] F. Cassol, R. Brittes, F. H. R. França, and O. A. Ezekoye, “Application of the weighted-sum-of-gray-gases model for media composed of arbitrary concentrations of H2O, CO2 and soot,” *International Journal of Heat and Mass Transfer*, vol. 79, pp. 796–806, Dec. 2014, doi: 10.1016/j.ijheatmasstransfer.2014.08.032.

[30] M. Runefors, J. Anderson, and B. Husted, “A comparison of radiative transfer models in FireFoam and FDS,” in *Interflam 2016: 14th International Conference*, Jul. 2016, pp. 59–69.

[31] K. B. McGrattan, R. D. Peacock, and K. J. Overholt, “Fire Model Validation - Eight Lessons Learned,” Mar. 2014. Accessed: Jan. 27, 2021. [Online]. Available: https://www.nist.gov/publications/fire-model-validation-150-eight-lessons-learned

[32] K. McGrattan, R. Peacock, and K. Overholt, “Validation of Fire Models Applied to Nuclear Power Plant Safety,” *Fire Technol*, vol. 52, no. 1, pp. 5–24, Jan. 2016, doi: 10.1007/s10694-014-0436-z.

[33] W. Chung and C. B. Devaud, “Buoyancy-corrected k–ε models and large eddy simulation applied to a large axisymmetric helium plume,” *International Journal for Numerical Methods in Fluids*, vol. 58, no. 1, pp. 57–89, 2008, doi: https://doi.org/10.1002/fld.1720.

[34] J. X. Wen, K. Kang, T. Donchev, and J. M. Karwatzki, “Validation of FDS for the prediction of medium-scale pool fires,” *Fire Safety Journal*, vol. 42, no. 2, pp. 127–138, Mar. 2007, doi: 10.1016/j.firesaf.2006.08.007.

[35] G. Maragkos and B. Merci, “Large Eddy Simulations of CH4 Fire Plumes,” *Flow, Turbulence and Combustion*, vol. 99, no. 1, 2017, doi: 10.1007/s10494-017-9803-4.

[36] A. Tewarson and Center for Fire Research (U.S.), *Prediction of fire properties of materials: Part 1. Aliphatic and aromatic hydrocarbons and related polymers*. Norwood, Calif.: Factory Mutual Research, 1986.

[37] J. L. De Ris, “A Scientific Approach To Flame Radiation And Material Flammability,” *Fire Safety Science*, vol. 2, pp. 29–46, 1989.

[38] C. Lam, “Detailed Analysis of Sandia Experimental Crude Oil Fire Data,” A1-016311.1, Aug. 2019.

[39] B. J. McCaffrey, *Purely buoyant diffusion flames: Some experimental results*. National Bureau of Standards. Accessed: Feb. 12, 2021. [Online]. Available: http://archive.org/details/purelybuoyantdif7919mcca

[40] B. M. Cetegen, E. E. Zukoski, and T. Kubota, “Entrainment in the Near and Far Field of Fire Plumes,” *Combustion Science and Technology*, vol. 39, no. 1–6, pp. 305–331, Aug. 1984, doi: 10.1080/00102208408923794.